ALMA-IMF

N. Cunningham, A. Ginsburg, R. Galván-Madrid, F. Motte, T. Csengeri, A. Stutz, M. Fernández-López, R. Álvarez-Gutiérrez, M. Armante, T. Baug, et al.

N. Cunningham, A. Ginsburg, R. Galván-Madrid, F. Motte, T. Csengeri, et al.. ALMA-IMF. Astronomy and Astrophysics - A&A, 2023, 678, pp.A194. 10.1051/0004-6361/202245429 . hal-04294996

HAL Id: hal-04294996
https://hal.science/hal-04294996
Submitted on 2 Dec 2023

A&A 678, A194 (2023)
https://doi.org/10.1051/0004-6361/202245429

Astronomy & Astrophysics

ALMA-IMF

VII. First release of the full spectral line cubes: Core kinematics traced by DCN $J = (3–2)$

N. Cunningham[1], A. Ginsburg[2], R. Galván-Madrid[3], F. Motte[1], T. Csengeri[4], A. M. Stutz[5], M. Fernández-López[6], R. H. Álvarez-Gutiérrez[5], M. Armante[7,8], T. Baug[9], M. Bonfand[4,21], S. Bontemps[4], J. Braine[4], N. Brouillet[4], G. Busquet[10,11,12], D. J. Díaz-González[3], J. Di Francesco[18], A. Gusdorf[7,8], F. Herpin[4], H. Liu[19], A. López-Sepulcre[1,13], F. Louvet[1,22], X. Lu[20], L. Maud[14], T. Nony[3], F. A. Olguin[15], Y. Pouteau[1], R. Rivera-Soto[3], N. A. Sandoval-Garrido[5], P. Sanhueza[16,17], K. Tatematsu[16,17], A. P. M. Towner[2], and M. Valeille-Manet[4]

(Affiliations can be found after the references)

Received 10 November 2022 / Accepted 26 May 2023

ABSTRACT

ALMA-IMF is an Atacama Large Millimeter/submillimeter Array (ALMA) Large Program designed to measure the core mass function (CMF) of 15 protoclusters chosen to span their early evolutionary stages. It further aims to understand their kinematics, chemistry, and the impact of gas inflow, accretion, and dynamics on the CMF. We present here the first release of the ALMA-IMF line data cubes (DR1), produced from the combination of two ALMA 12 m-array configurations. The data include 12 spectral windows, with eight at 1.3 mm and four at 3 mm. The broad spectral coverage of ALMA-IMF (~6.7 GHz bandwidth coverage per field) hosts a wealth of simple atomic, molecular, ionised, and complex organic molecular lines. We describe the line cube calibration done by ALMA and the subsequent calibration and imaging we performed. We discuss our choice of calibration parameters and optimisation of the cleaning parameters, and we demonstrate the utility and necessity of additional processing compared to the ALMA archive pipeline. As a demonstration of the scientific potential of these data, we present a first analysis of the DCN (3–2) line. We find that DCN (3–2) traces a diversity of morphologies and complex velocity structures, which tend to be more filamentary and widespread in evolved regions and are more compact in the young and intermediate-stage protoclusters. Furthermore, we used the DCN (3–2) emission as a tracer of the gas associated with 595 continuum cores across the 15 protoclusters, providing the first estimates of the core systemic velocities and linewidths within the sample. We find that DCN (3–2) is detected towards a higher percentage of cores in evolved regions than the young and intermediate-stage protoclusters and is likely a more complete tracer of the core population in more evolved protoclusters. The full ALMA 12m-array cubes for the ALMA-IMF Large Program are provided with this DR1 release.

Key words. instrumentation: interferometers – stars: formation – stars: massive – stars: kinematics and dynamics – ISM: structure – ISM: molecules

1. Introduction

The relative number of stars born with different masses between 0.01 $M_\odot$ and >100 $M_\odot$, described by the initial mass function (IMF), is thought to be universal in studies of the cosmic history of star formation, including within our own Galaxy (e.g. Bastian et al. 2010; Kroupa et al. 2013). Early studies of the core mass distribution in local star-forming regions (SFRs) found distributions with shapes similar to the stellar IMF, suggesting a direct mapping of the core mass function (CMF) to the IMF with a constant efficiency factor (e.g. Motte et al. 1998, 2001; Testi & Sargent 1998; Alves et al. 2007; Enoch et al. 2008; Könyves et al. 2015). These studies, however, were based on nearby star-forming clouds, where the core mass was limited to <5 $M_\odot$. More recent studies on a larger selection of clouds (e.g. Zhang et al. 2015; Ohashi et al. 2016; Csengeri et al. 2017a; Lu et al. 2020) and the pilot studies of the ALMA-IMF Large Program (e.g. Ginsburg et al. 2017; Motte et al. 2018, and Sanhueza et al. 2019) identified varying CMF shapes, with evidence for top-heavy CMFs towards regions forming massive stars. Moreover, the dependence of the IMF on the environment remains the subject of debate (see reviews by Offner et al. 2014; Krumholz 2015; Ballesteros-Paredes et al. 2020; Lee et al. 2020). These circumstances highlighted the need for a larger, more statistically robust sample of protoclusters in different environments to test the universality of the CMF and determine if the cloud characteristics impact its shape.

ALMA-IMF is an ALMA Large Program (#2017.1.01355.L, PIs: Motte, Ginsburg, Louvet, Sanhueza) to survey 15 nearby high-mass SFRs in the Galactic plane with the goal of characterising the CMF and its evolution. To understand the CMF fully, it is imperative to also investigate the distribution, dynamics, and kinematics of the gas from clumps to clusters down to core scales and determine if inflows, outflows, or the formation of filaments may be correlated with the CMF shape or impact its shape over time. One of the main objectives of the ALMA-IMF Large Program is to discriminate between the quasi-static and dynamic scenarios of cloud-scale star formation by quantifying the role of cloud and core kinematics in defining core mass and core mass growth over time.

An overview of ALMA-IMF is presented in Paper I by Motte et al. (2022), who describes the sample selection, classification of the evolutionary nature of individual protoclusters in the three subgroups (i.e. young, intermediate, and evolved), and early results, highlighting the complex velocity and filamentary structures in the protoclusters. In Paper II, Ginsburg et al. (2022a)

Table 1. Overview of the ALMA-IMF protocluster clouds and their evolutionary stage.

Protocluster cloud name $^{(1)}$	RA $^{(1)}$ [ICRS (J2000)]	Dec $^{(1)}$ [ICRS (J2000)]	$V_{\rm LSR}$ $^{(1)}$ [km s^{-1}]	d $^{(1)}$ [kpc]	Evolutionary stage $^{(2)}$	Imaged areas$^{(3)}$ [pc × pc]		$f_{\rm BW}$ lines$^{(4)}$	
						$A_{1.3\,\rm mm}$	$A_{3\,\rm mm}$	B3	B6
W43–MM1	18:47:47.00	−01:54:26.0	+97	5.5 ± 0.4	Y	3.1 × 2.3	5.1 × 4.0	0.64	0.55
W43–MM2	18:47:36.61	−02:00:51.1	+97	5.5 ± 0.4	Y	2.6 × 2.4	5.1 × 4.0	0.46	0.52
G338.93	16:40:34.42	−45:41:40.6	−62	3.9 ± 1.0	Y	1.6 × 1.6	2.9 × 2.8	0.49	0.25
G328.25	15:57:59.68	−53:58:00.2	−43	2.5 ± 0.5	Y	1.4 × 1.4	2.2 × 1.9	0.2	0.53
G337.92	16:41:10.62	−47:08:02.9	−40	2.7 ± 0.7	Y	1.2 × 1.1	2.1 × 2.0	0.37	0.53
G327.29	15:53:08.13	−54:37:08.6	−45	2.5 ± 0.5	Y	1.3 × 1.3	1.9 × 1.8	0.65	0.48
G351.77	17:26:42.62	−36:09:20.5	−3	2.0 ± 0.7	I	1.3 × 1.3	1.8 × 1.7	0.64	0.56
G008.67	18:06:21.12	−21:37:16.7	+37.6	3.4 ± 0.3	I	2.2 × 1.4	3.1 × 2.1	0.22	0.29
W43-MM3	18:47:41.46	−02:00:27.6	+97	5.5 ± 0.4	I	2.7 × 2.4	5.1 × 4.0	0.13	0.08
W51-E	19:23:44.18	+14:30:29.5	+55	5.4 ± 0.3	I	2.6 × 2.4	4.2 × 3.9	0.3	0.37
G353.41	17:30:26.28	−34:41:49.7	−17	2.0 ± 0.7	I	1.3 × 1.3	1.8 × 1.7	0.14	0.08
G010.62	18:10:28.84	−19:55:48.3	−2	4.95 ± 0.5	E	2.3 × 2.2	3.8 × 3.6	0.11	0.28
W51-IRS2	19:23:39.81	+14:31:03.5	+55	5.4 ± 0.3	E	2.6 × 2.4	4.2 × 3.9	0.26	0.42
G012.80	18:14:13.37	−17:55:45.2	+37	2.4 ± 0.2	E	1.5 × 1.5	2.2 × 2.1	0.12	0.16
G333.60	16:22:09.36	−50:05:58.9	−47	4.2 ± 0.7	E	2.9 × 2.9	3.9 × 3.7	0.16	0.2

Notes.$^{(1)}$Protocluster name, central position, and velocity relative to the local standard of rest used for the ALMA-IMF observations. $V_{\rm LSR}$ values are taken from the high-density gas studies by Wienen et al. (2015), Ginsburg et al. (2015) for W51, Nguyen-Luong et al. (2013) for W43, and Immer et al. (2014) for G012.80. The phase centre of W43-MM1 in the pilot study is RA = 18:47:46.50, Dec = −01:54:29.5. Distances are taken from Motte et al. (2022) and references therein. $^{(2)}$Classification of the ALMA-IMF protocluster clouds: Young (Y), Intermediate (I), and Evolved (E). See Sect. 4.1 of Motte et al. (2022). $^{(3)}$Physical areas encompassing the combined primary beams of the 1.3 mm and 3 mm mosaics. The released maps cover an area down to the full width at 10% of the maximum of the primary beam response. $^{(4)}$This is the fraction of the bandwidth found to contain bright line emission, which was excluded to make the `cleanest` continuum cubes, i.e. $1 - f_{\rm BW,cleanest}$ from Table 3 of Ginsburg et al. (2022a). To first order, this fraction highlights the percentage of bandwidth containing bright line emission and illustrates the variation of molecular emission between the regions.

describes the first data release of the continuum images and presents an analysis of the spectral indices on the continuum data. Paper III, Pouteau et al. (2022), and Louvet et al. (2023) utilise the ALMA-IMF continuum data to characterise the continuum cores, providing the first core catalogues and building the first individual region and global CMFs for the 15 protoclusters. The next step in understanding the origin of the CMF is to measure the internal kinematics with evolution and determine their importance on the shape and evolution of the CMF over time. The ALMA-IMF spectral setup hosts a wealth of molecular emission well suited for this purpose, such as the ^{12}CO (2–1), SiO (5–4), and SO (6–5), which can be used to explore the outflow population and provide a means to characterise further the nature of the cores as being pre- or proto-stellar (see Nony et al. 2023). The core population, gas inflow, and filamentary structure towards the 15 protoclusters will be probed using dense gas tracers in the ALMA-IMF spectral coverage, such as ^{13}CS (5–4), DCN (3–2), N_2H^+ (1–0), and N_2D^+ (3–2) to understand further inflow onto the cores and characterise core mass growth with time and its implications on the CMF. In addition, the multitude of emission lines, from species tracing ionised gas to the interstellar complex organic molecules (iCOMs) present in the ALMA-IMF spectral coverage, will provide the community with an unprecedented database with high legacy value for cores, hot cores, shocks, and outflows. We present the data reduction steps and imaging strategies implemented to obtain the ALMA-IMF spectral line cubes. This DR1 data release provides the position-position-velocity image cubes of the 12 spectral windows (spws), ~6.7 GHz of bandwidth coverage per protocluster, resulting in 180 image cubes for the whole ALMA-IMF sample. As a demonstration of the scientific potential of these data, we also present a first analysis of the DCN (3–2) emission towards the 15 protoclusters. As DCN (3–2) is expected to be an optically thin, dense gas tracer, we further utilised the DCN emission to explore the core kinematics of the ~600 thermal dust cores identified and described in Louvet et al. (2023).

This paper is organised as follows: in Sect. 2, we report a summary of the observations taken by ALMA and an overview of the target regions. Section 3 describes the data processing and imaging strategy performed to produce the final deconvolved line cubes, the data products, and the post-processing steps. In Sects. 4, and 5 we provide an analysis and discussion of DCN line emission towards the 15 protoclusters. In Sect. 6, we give a summary of the DR1 release and the results obtained.

2. Observations

ALMA-IMF[1] (the ALMA Large Program #2017.1.01355.L, PIs: Motte, Ginsburg, Louvet, Sanhueza), targets 15 protocluster clouds in our Galaxy using ALMA with its 12 m, 7 m arrays and total power (TP) observations and in two frequency bands; Band-3 (B3; ~91–106 GHz) and Band-6 (B6; ~216–234 GHz). We combine Tables 1 and 2 from Motte et al. (2022) to provide here a global overview of the 15 observed protoclusters in Table 1, listing their central positions, $V_{\rm LSR}$ estimates, distances from the Sun, evolutionary nature, and imaged areas of the mosaics in ALMA's B3 (3 mm) and B6 (1 mm). In addition, Table 1 lists the fraction of the bandwidth containing bright line emission ($f_{\rm BW}$ line). This is the fraction of bandwidth that was excluded from making the `cleanest` continuum images (taken from Table 3 of Ginsburg et al. 2022a) and which highlights, to first order, the relative amount of molecular line emission present

---

[1] https://www.almaimf.com

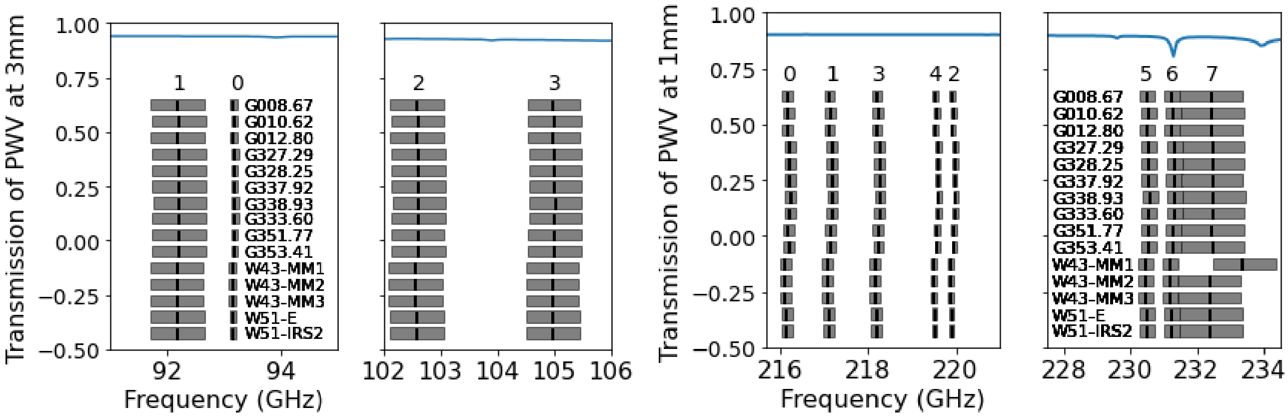

Fig. 1. Overview of the bandwidth covered by the spectral windows (spws, grey boxes), four in B3 (left panels) and eight in B6 (right panels) towards the 15 ALMA-IMF fields. The black line represents the central frequency for each spectral window. The numbers at the top denote the spectral windows as described in Table 2. The exact frequency coverage is provided in Table A.3. The blue line is the atmospheric transmission at a precipitable water vapour (PWV; The values over the observed frequency range are taken from `https://www.apex-telescope.org/sites/chajnantor/atmosphere/transpwv/index_ns.php`) of 1.796 mm in B6 and 5.18 mm in B3 (the typical values used in the ALMA sensitivity calculator), for a source at an elevation of 45 degrees. The coverage of the ALMA-IMF pilot program (B6 spectral window 7 for the W43-MM1 field) is offset by 1 GHz.

Table 2. Spectral setups of the ALMA-IMF Large Program.

ALMA band	Spectral window (SPW)	Central frequency [GHz]	Bandwidth [MHz]	Resolution [1] [kHz]	[$km s^{-1}$]	Main spectral lines
Band 6	SPW0	216.200	234	122	0.17	DCO^+ (3–2), CH_3OCHO, $OC^{33}S$ (18–17), HCOOH
	SPW1	217.150	234	244	0.34	SiO (5–4), DCN (3–2), $^{13}CH_3OH$, CH_3OCH_3
	SPW2	219.945	117	244	0.33	SO (6–5), $H_2^{13}CO$ ($3_{1,2}$–$2_{1,1}$), CH_3OH
	SPW3	218.230	234	122	0.17	H_2CO (3–2), $O^{13}CS$ (18–17), HC_3N (24–23), CH_3OCHO
	SPW4	219.560	117	122	0.17	$C^{18}O$ (2–1), C_2H_5CN
	SPW5	230.530	468	974	1.27	CO (2–1), CH_3CHO, CH_3OH, C_2H_3CN, C_2H_5OH
	SPW6	231.280	468	244	0.32	^{13}CS (5–4), N_2D^+ (3–2), OCS (19–18), CH_3CHO, CH_3OH, $CH_3^{18}OH$, C_2H_5CN
	SPW7	232.450	1875	976	1.26	H30α, CH_3CHO, CH_3OH, CH_3OCHO, C_2H_5OH, C_2H_5CN, CH_3OCH_3, CH_3COCH_3, $^{13}CH_3CN$ (13–12), $H_2C^{34}S$ ($7_{1,7}$–$6_{1,6}$)
Band 3	SPW0	93.1734	117	61	0.2	N_2H^+ (1–0), CH_3OH
	SPW1	92.2000	938	488	1.6	CH_3CN (5–4), H41α, $CH_3^{13}CN$, ^{13}CS (2–1), $^{13}CH_3OH$, CH_3OCHO
	SPW2	102.600	938	488	1.4	CH_3CCH (6–5), CH_3OH, H_2CS,C_2H_5CN, C_2H_5OH, CH_3NCO
	SPW3	105.000	938	488	1.4	H_2CS, CH_3OH, C_2H_3CN, C_2H_5OH, CH_3OCH_3

Notes. (1)This is the same as Table 3 of Motte et al. (2022), but with slightly updated values for the achieved spectral resolutions.

in the brightest regions of the protoclusters. A detailed description of the observing details and target selection for ALMA-IMF is provided in Ginsburg et al. (2022a) and Motte et al. (2022), respectively. ALMA-IMF was designed to observe homogeneously 15 of the most extreme and massive Galactic clouds within a distance range of 2–5.5 kpc. This distance range allows coverage of $\gtrsim 1 \times 1$ pc^2 of the highest column density regions towards each protocluster determined from ATLASGAL imaging (Csengeri et al. 2017b), while also allowing for a reasonable observing time towards the more distant protoclusters in the sample. The observing setup and array configurations were chosen to achieve a spatial resolution of ~2000 au for all protoclusters, regardless of distance. In B3, all targets were observed with two 12m array configurations. In B6, the more distant regions were observed in two configurations (see Ginsburg et al. 2022a for the full description of the 12m array configurations per protocluster). The released cubes are produced from the combination of the two ALMA 12m-array configurations. The resulting angular resolutions of the continuum data are between 0.3″ and 1.5″ using a robust weighting of 0 for the Briggs weighting. The major and minor axis of the synthesised beam for each spectral window towards each protocluster is provided in Table A.2.

An overview of the spectral setup of the 12 ALMA spectral windows is displayed in Fig. 1. The corresponding bandwidth, spectral resolution, along with main spectral lines in their respective spectral windows are also provided in Table 2[2]. For W43-MM1, the B6 data were taken as part of the pilot program, 2013.1.01365.S (Motte et al. 2018). The exact frequency coverage for each spectral window and field are given in Table A.3.

---

[2] This is the same as Table 3 of Motte et al. (2022) but with slightly updated values for the achieved spectral resolutions.

3. Data products

Together with this paper, we provide access to the DR1 line cube release[3], which includes the calibrated and imaged full spectral windows (both in B3 and B6) of the 12m array configurations towards the 15 protoclusters. ALMA-IMF also includes 7m array and TP observations using the same spectral setup. The combination of these data, which is particularly important for lines with significant extended emission, is ongoing, and those cubes will be added to the repository as they are created for future planned studies. For spectral window 0 in B3, which includes the N_2H^+ line, the 12 m only data still contain artefacts due to the extended emission and missing short spacings, we thus exclude this window from this DR1 release. The combined N_2H^+ data for this spectral window will be added to the repository as part of future works (e.g. Stutz et al., in prep.; Álvarez-Gutiérrez et al., in prep.; Sandoval et al., in prep.). We include the properties of spectral window 0 in B3 (e.g. beam size, and noise estimates) in this paper for completeness.

The data were restored to measurement sets using the `scriptForPI.py` files provided by the ALMA archive, and further batch processed with the custom scripts and imaging parameters of the ALMA-IMF data pipeline (Ginsburg et al. 2022a). All measurement sets underwent QA3 reprocessing: the FAUST Large Program (Project code: 2018.1.01205.L, Codella et al. 2021) reported that the calibration of the system temperature adopted by ALMA could result in the artificial suppression of bright lines[4]. The ALMA-IMF data were also affected by these issues, particularly spectral window 5 in B6 and spectral window 0 in B3, containing the brightest emission lines of CO (2–1) and N_2H^+ (1–0), respectively. The measurement sets were returned to the Joint ALMA Observatory for further QA3 processing in November 2020, and the reprocessing was completed in March 2021. The W43-MM1 B6 data from the pilot program 2013.1.01365.S (Motte et al. 2018) were also reprocessed following the same QA3 procedure as for the 2017.1.01355.L data.

3.1. ALMA-IMF data pipeline

The custom ALMA-IMF data pipeline developed to produce the calibrated and imaged continuum data (as described in Ginsburg et al. 2022a) was subsequently adapted to process the full spectral line windows. It runs in the CASA (McMullin et al. 2007) environment and is described in the following eight steps. The full data pipeline and custom python scripts can be found on the ALMA-IMF GitHub repository[5].

1. Retrieve and extract the data from the ALMA archive using astroquery (Ginsburg et al. 2019).
2. Run `scriptForPI.py` to restore the measurement sets.
3. Separate the continuum and line measurement sets with `split_windows.py`[5] and combine the different 12m array configurations.
4. Run the `continuum_imaging_selfcal.py` script[5] to perform the continuum imaging and self calibration[6].
5. Produce the continuum start model from the continuum data.

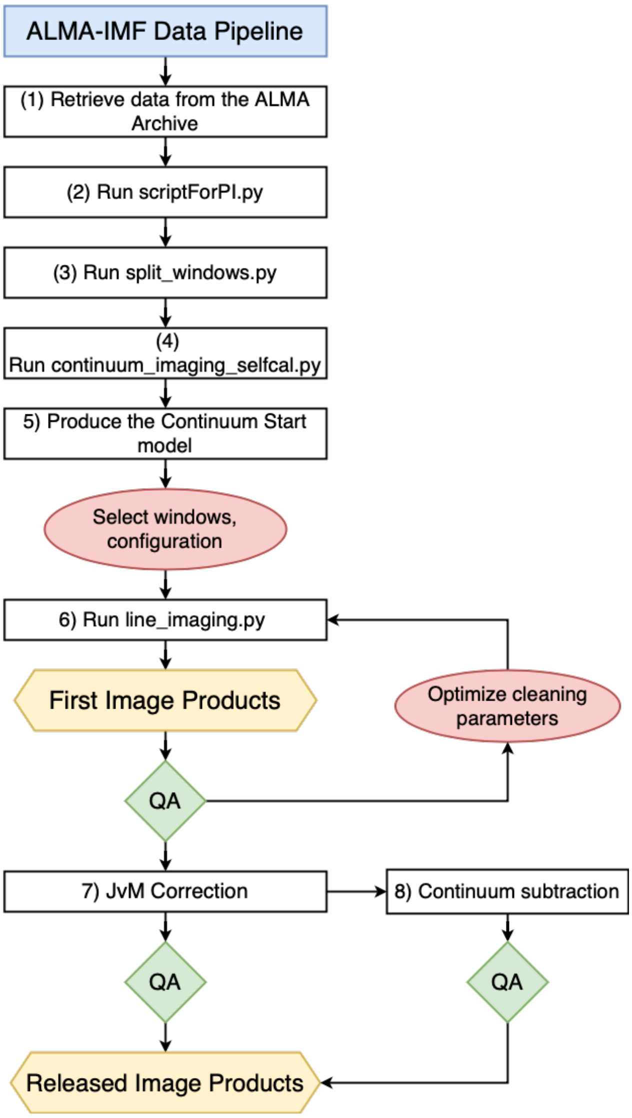

Fig. 2. Flow chart providing an overview of the framework of the ALMA-IMF data pipeline employed to produce the line cubes provided in this release. The white boxes labelled from 1–8 describe the steps in the pipeline that are defined by running scripts or procedures (as described in more detail in Sect. 3.1). Red ellipses highlight points where manual input was required to either select which line, spectral window, or configuration on which to perform `tclean`, or to optimise the `tclean` parameters after internal quality assessments (green diamonds).

6. Run the `line_imaging.py` script[5] to perform the line imaging.
7. Apply the 'JvM' correction (Jorsater & van Moorsel 1995) to the cleaned cubes (see Sect. 3.3 for more details).
8. Run `statcont` (Sánchez-Monge et al. 2017) on the imaged line cubes to produce the continuum subtracted cubes (this step is optional).

For illustration, Fig. 2 displays a flow diagram of the ALMA-IMF imaging pipeline and image processing steps taken to obtain the final line cubes provided in this release. The initial four steps are identical to the continuum data processing as detailed in Sect. 3.1.1 of Ginsburg et al. (2022a). Step 5) onward details the processing of the line cubes. In Step 5) the input start model for the line cleaning is derived from the output model of the continuum cleaning (see Sect. 3.2.1). To produce the optimal

---

[3] The ALMA-IMF project page is at `https://www.almaimf.com/data.html`. This Data Release is hosted at Harvard Dataverse `https://dataverse.harvard.edu/dataverse/alma-imf`

[4] `https://help.almascience.org/kb/articles/607`

[5] `https://github.com/ALMA-IMF/reduction`

[6] We note that the self-calibration solutions were not applied to the line data.

`tclean` parameters in CASA used for these data, we performed several internal quality assessments (QAs) of the `tclean` products and several iterations to test a range of `tclean` parameters (see Sect. 3.2 for more details). As with the continuum cleaning, the most important input file is `imaging_parameters.py`[5], which includes the user-specified `tclean` parameters for both the continuum and now the line cubes for all fields and spectral windows. Finally, the last two steps, 7 and 8, refer to post-processing actions after the final CASA cubes are produced. The optional continuum subtraction on the line cubes described in Step 8 is performed in the image plane using the `statcont` procedure, as described in Sánchez-Monge et al. (2017). The `statcont` continuum-subtracted cubes are included in the data release. We also provide the continuum estimates and the primary beam responses for each field and spectral window so that the unsubtracted and non-primary beam-corrected cubes can be reproduced if required.

3.2. *Optimisation of cleaning and imaging parameters*

The ALMA-IMF dataset covers a multitude of molecular lines with varying dynamic ranges and morphologies across the 15 protoclusters. Therefore, the `tclean` parameters are optimised to be as homogeneous as possible, allowing the pipeline to run in an automated way. In the following, we discuss the selection of `tclean` parameters implemented to reach the imaged line cubes of the released ALMA-IMF dataset.

3.2.1. Continuum start-model

Given the large extent of the mosaic coverage, the complexity of the data, and the varying dynamic range across an individual field, we chose not to perform a simple continuum subtraction in the uv-plane before running `tclean`. This choice led to difficulties, however, with `tclean` diverging for some fields. Thus, we use a continuum model cube as the input `startmodel` parameter in `tclean`. This model cube is constructed from the .tt0 and .tt1 products of the mostly line-free `cleanest` continuum imaging (see Ginsburg et al. 2022a), `tclean` then stores this as an initial model and subtracts it from the visibilities at the beginning of the deconvolution process.

3.2.2. Cleaning optimisation and masking

We performed several iterations of `tclean` using the Hogbom and multi-scale deconvolvers and tested methods to mask the line emission: (1) an internally developed auto-masking, (2) the CASA auto multi-threshold masking, and (3) a primary beam mask. Multi-scale deconvolution with a primary beam mask produced the most stable and optimal results over the full set of spectral windows. In spectral windows with bright and extended emission, the routines that mask in an automated way could not adequately cover the full extent of the emission. Furthermore, auto multi-threshold had additional convergence problems when working with multi-scale deconvolution. For these reasons, we opted to use the primary beam mask (pbmask) as our `tclean` mask, setting its limit to 10% of the primary beam response. For the deconvolver, we found that multi-scale clean performed better at recovering larger-scale emission than Hogbom deconvolution. This difference was expected since the latter uses only point sources as a model. We defined the scales used in multi-scale `tclean` using a geometric series starting at 0 and increasing by ~ × 2 the ratio of the minor beam axis to the cell size until a scale of ~5.5″ is reached. This largest scale is selected to be a factor of 2–3 smaller than the typical largest recoverable scale in the data. The scales used for each field and spectral window are provided in the `imaging_parameters.py` file[5].

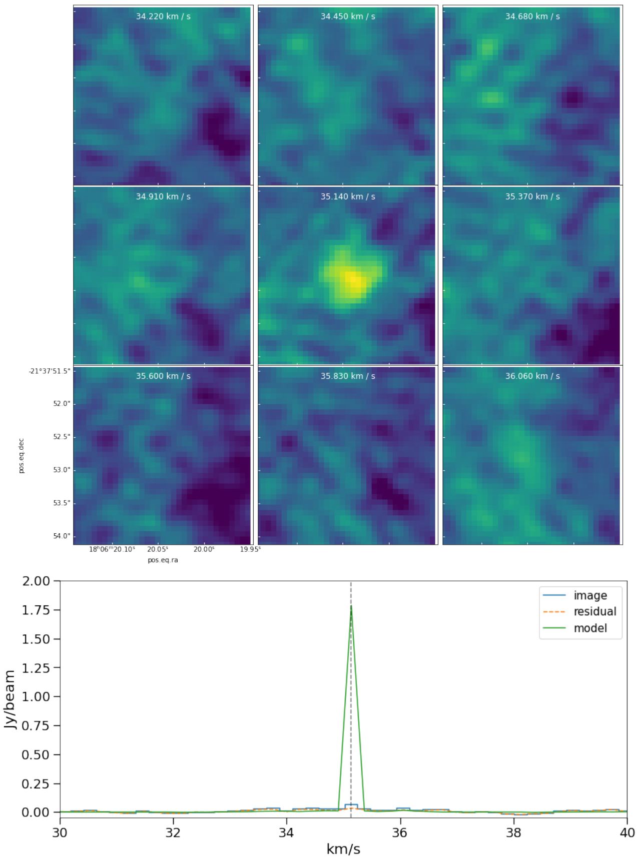

Fig. 3. Example of the ‘stippling’ effect as previously described in Czekala et al. (2021). The top panel shows nine channels of a zoomed-in region in a restored image cube, cleaned using a 3σ threshold. The central channel shows the resulting spurious emission peak. This bright emission, of order the beam size, is only present in a single channel, while the neighbouring pixels show no equivalent emission. The bottom panel shows the model extracted at the central pixel, where the bright model component (green line) is only found in a single pixel and channel. This model component is then convolved with the Gaussian clean beam during the `tclean` run to produce the restored image, resulting in spurious compact emission in a single channel.

3.2.3. Cleaning threshold

During the QA of the line cubes, we iterated over several cleaning thresholds. We found that using a relatively shallow threshold of 5σ resulted in the most stable outcomes, that is, mitigating the effects of divergence and ‘stippling’ over the full dataset. As described in Czekala et al. (2021) for the ALMA MAPS Large Program, a stippling pattern can be present in deeply cleaned cubes ($\leq 3\sigma$), which then results in artificial clean components appearing as spurious sources – of order the beam size – in the deconvolved image cubes. In Fig. 3, we show an example of this stippling effect in one of the ALMA-IMF line cubes. When cleaning down to 3σ, a bright model component was found in only one channel and pixel, resulting in a spurious emission peak in the cleaned cube, present in only a single channel. A Jupyter notebook describing this effect can

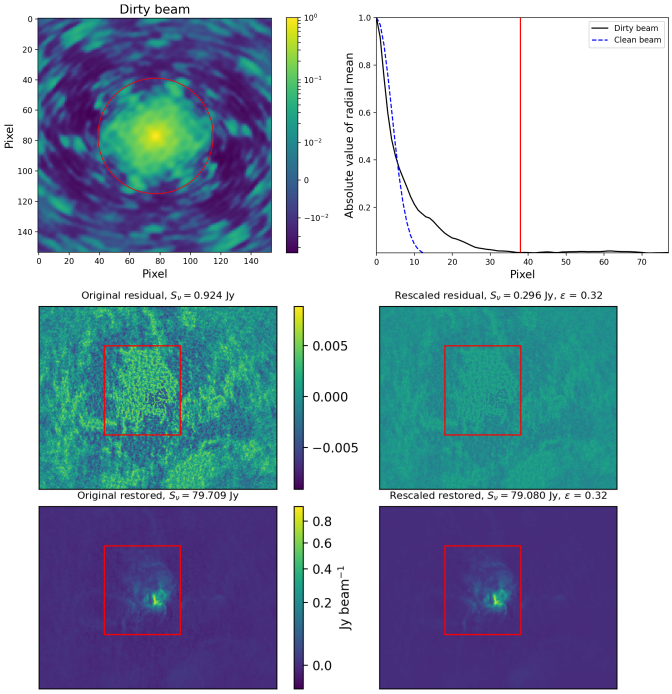

Fig. 4. Example of the JvM correction for the peak channel of the H41α line in spectral window 1 of Band 3 for protocluster G333.60. The top left panel shows the original PSF (i.e. the dirty beam), where the red circle marks the first null. The top right panel shows the absolute value of the radial profile of the beam (black solid line) and the corresponding approximation to a Gaussian clean beam (blue dashed line). The ϵ factor, defined as the ratio of the clean-to-dirty beam volumes, is 0.32 in this example. The residuals are shown for the original image (middle left panel) and after (middle right), the JvM correction is applied. The red rectangle shows the aperture where the quoted fluxes are measured. The restored images without (bottom left) and with JvM (bottom right) correction are shown in the bottom panels.

be found in the ALMA-IMF pipeline repository[7]. We estimate that this issue only affects <0.1% of the pixels in the cubes of this data release. In addition to the stippling, we found that cleaning to levels of 4σ or deeper also resulted in divergence across multiple spectral windows, compared with setting the noise threshold to $\geq 5\sigma$. For the latter thresholds, however, we still find divergence in a few channels towards spectral windows containing bright and extended emission. These are mainly identified around the $V_{\rm LSR}$ of the ^{12}CO (2–1) and C^{18}O (2–1) transitions. In these cases, we chose to mask the channels that showed divergence and re-run the `tclean`, leaving those channels uncleaned in the final cubes (the masked channel ranges can be obtained in the `imaging_parameters.py` file[5]). Towards the protocluster G351.77, we still identify divergences in several spectral windows. In the end, we ran `tclean` only down to 10σ level for this region for all spectral windows. The full set of cleaning parameters and masked channels can be found in the `imaging_parameters.py` file[5].

3.3. JvM correction

The JvM correction (Jorsater & van Moorsel 1995) is applied to the CASA-generated cubes to correct the flux scale of the residuals, and thus of the restored image, since the volumes of the clean and dirty beams are not the same (see also Walter et al. 2008; Czekala et al. 2021). Figure 4 illustrates this correction for the G333.60 region's peak channel of the H41α line (situated in spectral window 1 of Band 3). The top panels show that a Gaussian clean beam is a reasonable approximation for the central part of the original PSF (dirty beam) but not beyond ~50% of its FWHM. A factor ϵ is defined as the ratio of the clean-to-dirty beam volumes. The dirty beam is only considered up to its first null since this is the part approximated to a Gaussian during deconvolution and because the volume of a dirty beam without zero spacing integrated over its full domain is formally zero. The output CASA cubes are the channel-by-channel addition of a `.model` image convolved with the Gaussian clean beam (resulting in units of Jy per clean beam), the residuals contained in the `.residual` file, which are still in units of Jy per dirty beam, are then added. The JvM correction rescales the residuals to the same units (Jy per clean beam) by multiplying them by the ϵ factor before the final image restoration[8].

Figure 4 shows a case where ϵ is as low as 0.32 (typically $\epsilon > 0.5$). The mean, median and standard deviation for ϵ over all spectral windows and fields are 0.62, 0.60, and 0.17, respectively. The effect of the JvM correction on the flux in a restored-image is minimal when the line is relatively bright and deeply cleaned. The JvM correction becomes important as the flux in the residuals becomes larger than the flux in the model and as ϵ decreases. The first condition can occur in cubes with very bright and extended line emission that cannot be cleaned too deeply or for faint lines that reside in the same cube of a much brighter line. A small ϵ appears when the dirty beam has a substantial plateau beyond its core, which might occur due to the combination of different array configurations. The ϵ factor for each protocluster and spectral window can be found in its FITS header and in Table A.5. The `CASA`-generated cubes generally have a different beam for every channel. The common beam found by `radio-beam` is the minimum beam that contains all of the per-channel beams, excluding outliers (which sometimes occur at the edge of spectral windows). Although the channel-to-channel beam should vary smoothly with frequency, sometimes significant jumps in beam size can occur due to software instabilities. To make the cubes more readily usable, we convolve the model in every channel to a common Gaussian beam per spectral window using the `radio-beam` tool[9]. Using a common beam has the advantage of eliminating channel-to-channel variations, resulting in a cube with the same spatial resolution across all channels and allowing direct comparisons of full-bandwidth spectra in units of brightness temperature.

The JvM cubes are in a common unit (Jy per clean beam), meaning flux measurements from these cubes can be interpreted. As discussed previously, these cubes are not deeply cleaned due to divergence and stippling issues over the full bandwidth, which can result in significant real emission remaining in the residuals. Thus, the JvM correction provides a more accurate estimation of the flux in our data. An important consequence, however, of performing the JvM correction is that the noise in the residual is also scaled by the ϵ factor. The most conservative approach to obtaining the noise, which we adopt here, is to estimate the noise from emission and line-free regions in the JvM cubes (in units of Jy per clean beam) and scale by $1/\epsilon$ factor (see Sect. 3.5), thus, taking the higher noise estimates in units of Jy per dirty

---

[7] `https://github.com/ALMA-IMF/notebooks/blob/master/ConfettiQA.ipynb`

[8] A public tool to apply the JvM correction to interferometric images will be released in `https://github.com/radio-astro-tools/beam-volume-tools`

[9] `https://github.com/radio-astro-tools/radio-beam`

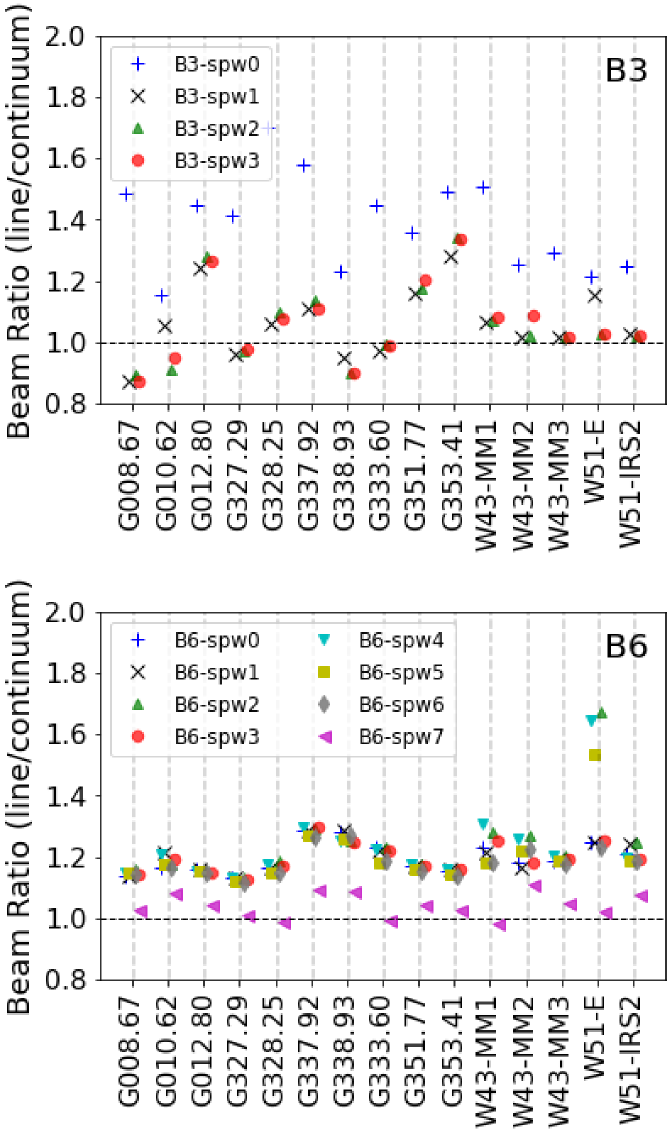

Fig. 5. Ratio of the average line to continuum beam for each protocluster and spectral window (B3 top; B6 bottom panels). Where the average beam is defined as $\theta_{\mathrm{ave}} = \sqrt{\theta_{\mathrm{maj}} \times \theta_{\mathrm{min}}}$. We scale the ratio linearly to account for the frequency difference between the central frequency of the spectral window and the frequency of the continuum beam. The native beam major and minor axis for each spectral window is listed in Table A.2. The proposed beam and the average recovered continuum beam for all fields are given in Table A.1. The central frequency of the continuum images for B3 and B6 for each protocluster is given in Ginsburg et al. (2022a), and the spectral coverage for each of the line cubes are shown in Table A.3. The dashed horizontal line shows a one-to-one ratio between the line and continuum beams.

beam. In other words, we assume the noise estimated from a smaller clean beam should be larger by the ratio of the dirty and clean beam areas. This conservative approach means we adopt a higher noise level (in units of Jy per dirty beam), reducing the number of sources we consider significant. Still, we suggest further investigation of noise behaviour with non-Gaussian beams would be helpful. We note that Walter et al. (2008) and Czekala et al. (2021) adopt the noise in Jy per dirty beam and Jy per clean beam as their noise levels, respectively. The latter is more representative of the telescope sensitivity for point-source detection prior to deconvolution.

3.4. Beam sizes

In Table A.1, we present the proposed beam and the average recovered continuum beam for all fields. In Table A.2, we provide the major and minor axes along with the beam position angle for all spectral windows towards all protoclusters. Plots of the continuum PSFs and central average frequencies are presented in Ginsburg et al. (2022a). In Fig. 5, we show the ratio of the average recovered beam for each spectral window and protocluster compared to the average continuum beam. We further scale the beam ratio by the frequency difference between the central frequency in the given spectral window to the frequency used to determine the continuum beam to account for any beam size differences due to frequency. The average ratio of the line beams and continuum beam is ~1.2, except for B3, spectral window 0 (which includes the N_2H^+ transition), where the ratio is on average ~1.4. The larger beams recovered in this spectral window are due to a plateau in the PSF, which may have occurred due to the combination of two considerably different array configurations, which resulted in a broader Gaussian fit during the determination of the synthesised beam in `tclean`. An example of the PSF profiles and synthesised beams for all spectral windows towards G012.80 is shown in Fig. 6. Additional broadening can be seen in B3, particularly in spectral window 0.

3.5. Noise estimation

Estimating the noise homogeneously over the full sample of protoclusters and spectral windows is non-trivial, given that several lines are present in the same spectral window, with varying morphology and intensity across a given protocluster. To estimate noise levels, we use the median-absolute-deviation (MAD) estimator[10] and take a threshold cut in intensity so that the noise is estimated using only the 25% of the channels with the lowest intensity across the full spectral window, and using the manually defined regions[11] which were created for the continuum estimates of the noise in Ginsburg et al. (2022a). The noise estimates for each field and spectral window are taken on the non-continuum subtracted line cubes with the JvM correction applied but uncorrected by the primary beam response. As described in Sect. 3.3, we adopt the noise in units of Jy per dirty beam and provide the noise estimates for all fields and spectral windows (in units of mJy per dirty beam) in Table A.4. We also provide the requested (theoretical) noise in Table A.4 from the original ALMA-IMF proposal scaled to the obtained channel width and central frequency. In Fig. 7, we compare the requested to the achieved noise in brightness temperature units. To provide a direct comparison between the achieved noise (taken from Table A.4) and the requested noise, we scaled the requested noise to the same spectral resolution, beam size, and central frequency as those obtained in the observed data cubes for all spectral windows. We show in Fig. 7 that the achieved noise is better than expected (in all but one case) and, on average, ~2.3 times lower than anticipated, accounting for the larger beam sizes achieved. We note that the data were observed in better conditions for most fields and with lower system temperatures (typically 20–30% better, but in some cases up to ~50%) than those used for the sensitivity calculator's noise estimates. The continuum noise is typically within a factor of two (Ginsburg et al. 2022a) of the theoretical value.

---

[10] Implemented in `astropy.stats.median_abs_deviation` and we scale this by 1.4826 such that the reported value is equivalent to the standard deviation if the underlying data are normally distributed.

[11] https://github.com/ALMA-IMF/reduction/tree/master/reduction/noise_estimation_regions

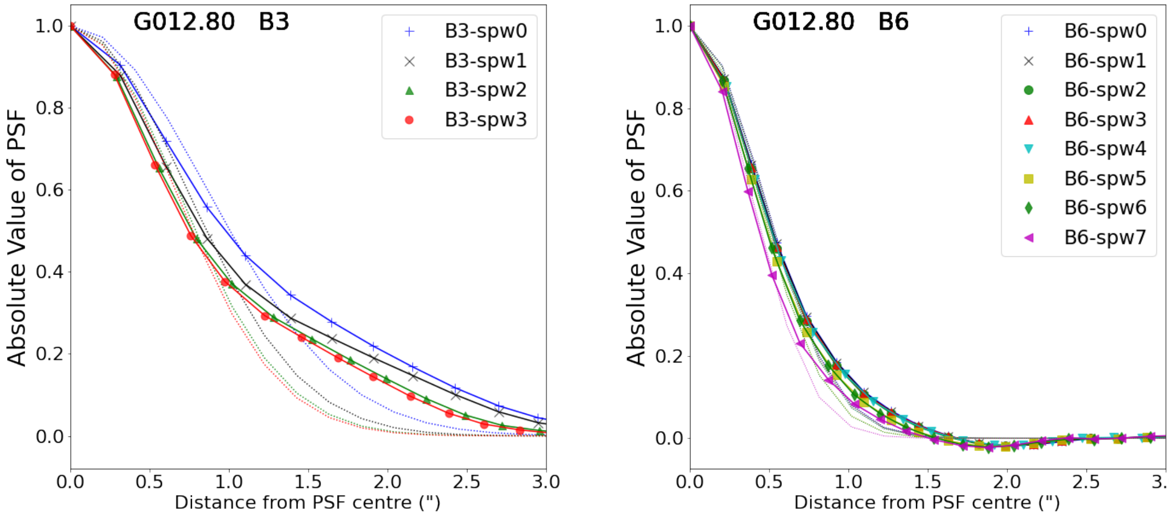

Fig. 6. Absolute value of the radial mean of the PSF (dirty beam) for the protocluster G012.80 as a function of the distance from the PSF centre (in arcseconds). B3 spectral windows are shown on the left and B6 spectral windows are on the right. The solid lines use the `.psf` outputs from `tclean` and the dashed lines are the expected Gaussian clean beams (the FWHM is taken from the geometric mean of the beam major and minor axes). For the B3 spectral windows, the Gaussian clean beam is a good approximation to the PSF only within ~50% of its FWHM. B3 spectral window 0 shows the largest deviation, resulting in a larger estimation of the respective Gaussian clean beam in `tclean`. The B6 spectral windows typically show a better correspondence between the PSFs and the Gaussian clean beam.

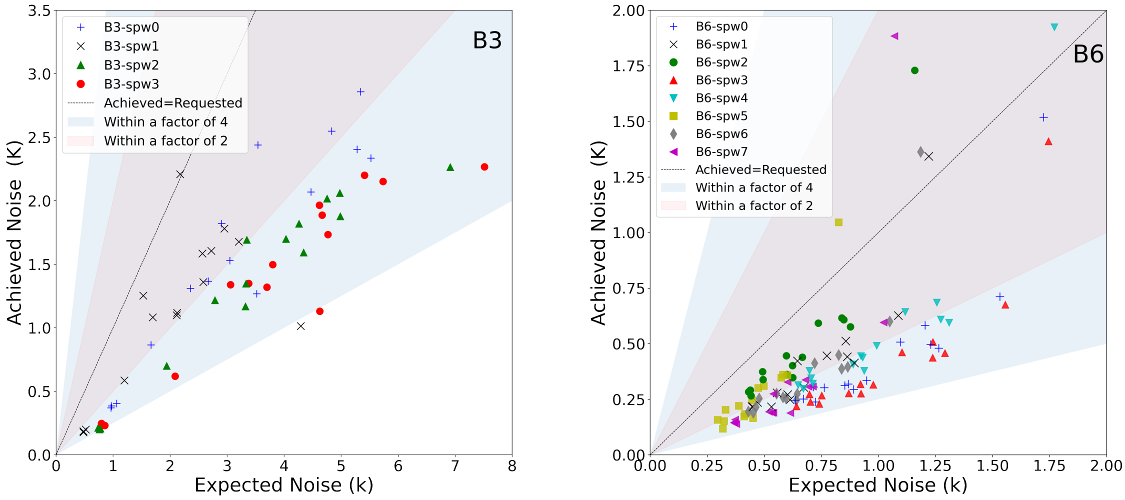

Fig. 7. Expected thermal noise from the observations vs the achieved noise in the cubes for each spectral window in Kelvin (B3 left panel and B6 right panel). The Y-axis shows the measured noise in the released cubes in Jy per dirty beam converted to brightness temperature as described in Sect. 3.4. The X-axis shows the expected brightness temperature sensitivity for the proposed beam sizes (see Table A.1). Furthermore, to directly compare the achieved noise in the data to the expected noise from the proposed observations, we scale the expected noise by the frequency difference between the requested representative frequency and the central frequency of each spectral window. We also scale the expected noise by the difference in the representative channel width and the achieved channel width for each spectral window. As shown in Fig. 5, the achieved beam area is typically larger than the continuum beam by ~1–1.5×. Thus, the expected noise is also scaled to account for the difference in the beam areas between the achieved and proposed beams (see Table A.2 for the exact proposed beams and achieved beams per field). The shaded regions show a noise within a factor of two (pink) and four (blue) from the expected noise, and the dashed line represents a 1 to 1 ratio. We typically achieve a noise on average ~2–2.5 times lower than expected.

3.6. Released line cubes and post-processed image products

The DR1 line cube release discussed here is made available with this work[12]. We provide the continuum-subtracted cubes corrected for their respective primary beam response and the JvM correction. The `STATCONT` procedure employed simultaneously over the full spectral window can satisfactorily remove the continuum for most of the bandwidth and fields, however, towards, the positions of hot core candidates or bright outflows, the continuum subtraction could be improved. For completeness, we also include the continuum estimates from the cubes, the models, residuals and primary beam files in this release. The naming structure of the cubes is given as the protocluster name, the ALMA band (i.e. B3 or B6), array configuration (we release here only the 12m array data), and spectral window (see Table 2 for reference). Meanwhile `.JvM` refers to the JvM correction (we

---

[12] See the ALMA-IMF website; https://www.almaimf.com/data.html and is hosted by Harvard Dataverse; https://dataverse.harvard.edu/dataverse/alma-imf

have applied the correction to all released cubes; the ϵ factors used can be found in Table A.4), `.image.pbcor` refers to the primary beam correction, and `.statcont.contsub` refers to the continuum subtraction applied using the `STATCONT` procedure. The cubes range from the smallest at several MBs to the largest, which are ~50 GB. The full DR1 dataset is ~5 TB.

4. Analysis

The full set of ALMA-IMF line cubes contains a wealth of emission from a variety of molecular line species (see Table 2) and will provide the community with an unprecedented database with high legacy value for cores, hot cores (e.g. Bonfand et al. 2023; Brouillet et al. 2022), outflows, and inflows. To illustrate the richness of the ALMA-IMF survey data, we present a first look at the DCN (3–2) emission towards the 15 protoclusters, along with an analysis of the DCN (3–2) emission extracted from the compact continuum core population. We utilise the molecular transition DCN (3–2) as a proxy for the gas associated with the core as it is typically an optically thin tracer with a critical density of $\sim 10^7$ cm^{-3}. Furthermore, towards several low, intermediate, and massive star-forming regions DCN (3–2) emission has been previously observed to coincide well with the thermal dust emission associated with star-forming cores (see, e.g. Cunningham et al. 2016; Tatematsu et al. 2020; Sakai et al. 2022) and is not typically observed as an outflow tracer (however, it has been associated with shocks in, e.g. L1157-B1: Busquet et al. 2017).

4.1. Global scale DCN (3–2) morphology

DCN (3–2) has a rest frequency of 217.23854 GHz (Müller et al. 2001, 2005) and is located in B6, spectral window 1, with a spectral resolution of 0.34 km s^{-1}. We use the continuum subtracted (`STATCONT`) line cubes provided in this release and do not perform any additional baseline subtraction. We then extract a 50 km s^{-1} wide subset of channels around the $V_{\rm LSR}$ reported in Motte et al. (2022) and create the first three moment maps towards the 15 protoclusters, using the non-primary beam corrected cubes. The DCN (3–2) emission is integrated over a manually determined velocity range for each protocluster, using a 4σ threshold to identify channels where DCN (3–2) emission is present over an area larger than the beam size (the velocity ranges used for each protocluster are provided in the figure captions). The σ level is the noise estimated for spectral window 1 as described in Sect. 3.5 (i.e. in units of mJy per dirty beam) and listed for each protocluster in Table A.4. Furthermore, for the first and second-moment maps, we take an additional threshold cut per channel and include only pixels that contain emission $>4\sigma$, preventing noisy pixels from being added into them. To highlight the contrast in the DCN (3–2) emission across the sample, we selected two protoclusters with different evolutionary classifications: young G338.93 and evolved G333.60, and display their first three moments in Fig. 8. Towards G338.93, there are two prominent ~0.2 pc clumps of emission with a spread of ~10 km s^{-1} in velocity. On the other hand, towards G333.60, the emission is tracing a more filamentary structure spread over a larger extent, that is, over ~2 pc. This morphological difference appears to be part of a general trend (see Fig. D.1), where dense gas is less widespread in the young regions. Still, the trend needs to be confirmed using various gas tracers (Cunningham et al., in prep.). The full set of moment maps towards all protoclusters is presented in Fig. D.1. We note that in a few regions (e.g. G327.29 and G351.77), the moment 0 maps display negative bowls, resulting from the missing short spacings in this 12m-array only data.

4.2. DCN (3–2) line extraction and fitting

The DCN (3–2) line emission is extracted from each core using `spectral-cube`[13] (Ginsburg et al. 2019). We use an elliptical aperture with a major (minor) axis length twice that of the continuum source major (minor) FWHM to extract the spectrum, where the continuum core sizes are taken from Louvet et al. (2023)[14]. As with the continuum cores, where the background is filtered to estimate the core properties more accurately, we chose to perform background subtraction on the DCN (3–2) emission to limit contamination from background and foreground DCN (3–2) within the dense regions of the protocluster. We extract the background emission from an elliptical annulus with an inner major (minor) axis size equal to the size of the spectral aperture (i.e. twice the continuum source major (minor) FWHM) and outer radius size 1.5x larger (i.e. three times the continuum source major (minor) FWHM). In these complex regions, particularly towards the densest parts of the protoclusters, nearby cores can overlap with the background annulus. We excluded pixels from neighbouring cores that spatially overlap with the background annulus in these instances. An example of the core spectral aperture and resulting background annulus is given in Appendix E. A core-averaged spectrum is then extracted for each of the 595 cores across the 15 ALMA-IMF clouds, and the average spectrum from its background annulus is subtracted from it. The resulting core-averaged, background-subtracted spectrum for each core is then fitted using a single component hyperfine structure model (HFS) adapted for the DCN (3–2) transition in `PySpecKit` (Ginsburg & Mirocha 2011; Ginsburg et al. 2022b). The methodology of the line extraction, background subtraction, and HSF fitting are discussed further in Appendix E.

4.3. DCN (3–2) detection of cores

A core is determined to have a DCN (3–2) detection if a velocity dispersion of >0.2 km s^{-1} and a signal-to-noise ratio $(S/N) > 4\sigma$ are found in the core averaged, background-subtracted spectrum. The noise in the spectrum is estimated from the MAD[10] in 30 continuous channels (~10 km s^{-1}) from either the lower or upper part of the spectrum that were identified by eye to be in a line free part of the spectrum. Furthermore, as described in Sect. 3.3, we use the higher noise estimates in units of mJy per dirty beam.

Of the 595 continuum cores, 357 (60%) have a DCN (3–2) detection. Within each protocluster, however, several detected cores display complex spectra (91 over the full sample), thus not well fit by the single component HFS. We classify spectra as complex-type if multiple components or clear signs of structure affecting the single component fits are present in the spectrum. This is done manually by visually inspecting all fitted DCN (3–2) spectra. While the $V_{\rm LSR}$ from complex-type spectral fits are provided for reference, the linewidths are not given, and these cores are excluded from the following analysis. Only cores determined to be well fit by a single component (e.g. listed as single in Table 3) are considered further. The complex-type spectra may harbour multiple velocity components or arise from line self-absorption due to optical depth

---

[13] https://spectral-cube.readthedocs.io/en/latest/

[14] We use here the smoothed core catalogue, where the continuum maps are smoothed to the same angular resolution of 2700 au. The extraction is done with v210414 of *getsf* (Men'shchikov 2021).

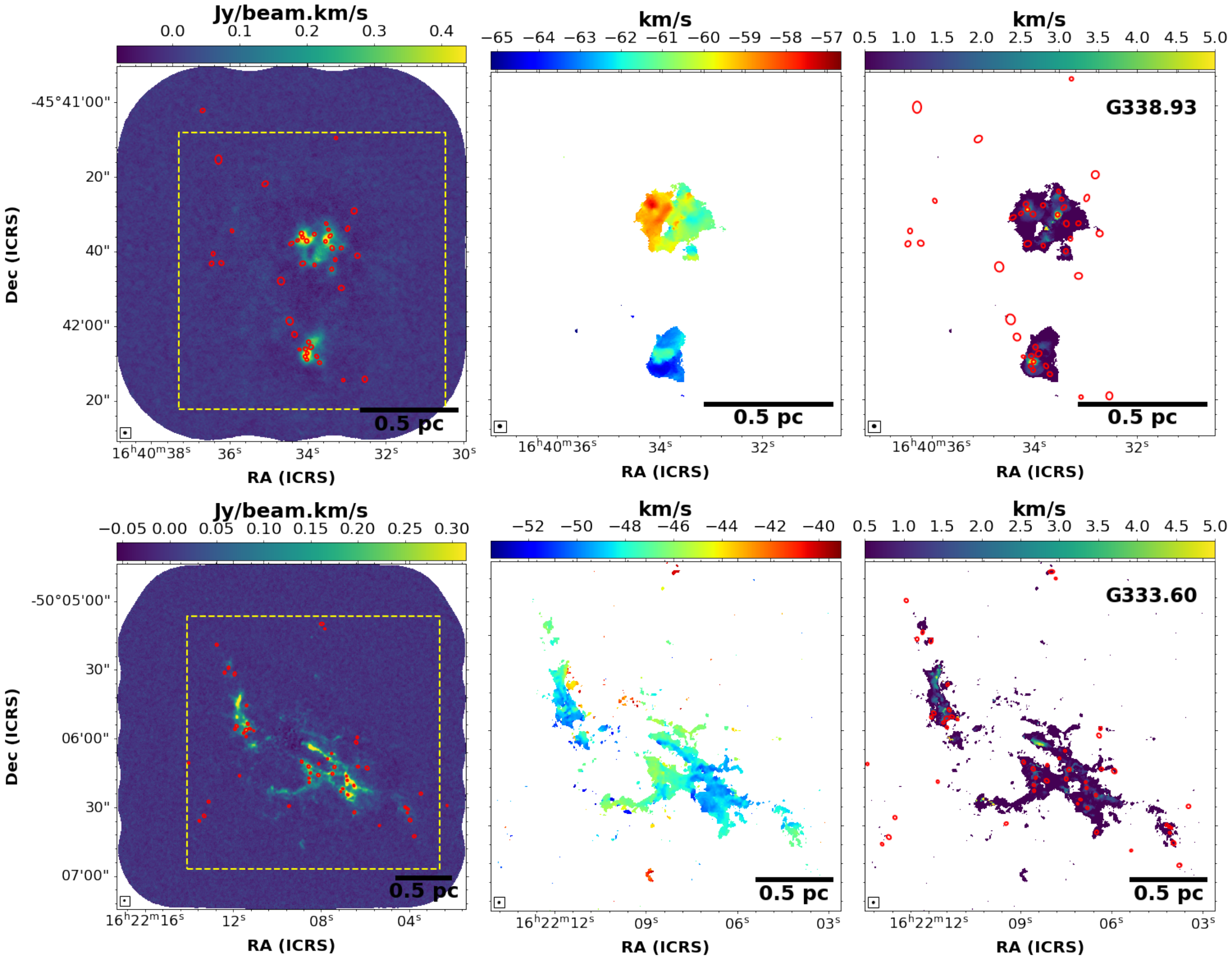

Fig. 8. Moment maps (moment 0, 1, and 2 in the left, centre, and right panels, respectively) of DCN (3–2) emission towards two example protoclusters with different evolutionary classifications, the young protocluster G338.93 (top), and the evolved G333.60 (bottom). All three moments have been determined over a velocity range of −53.4 to −68.6 km s^{-1} and −40 to −52.7 km s^{-1} for G338.93 and G333.60, respectively. For the moment 0 and moment 2 maps, we overlay the core positions and sizes (red ellipses) from the continuum core catalogue described in Louvet et al. (2023). For the moment 1 and moment 2 maps, we show a zoom-in of the area highlighted by the yellow dashed box overlaid on the moment 0 map. The moment 1 and moment 2 maps have an additional threshold cut per channel of 4σ. The synthesised beam is shown in the bottom left corner of each image. These maps highlight differences in the morphology traced by the DCN (3–2) emission, where the emission is more widespread and filamentary towards the evolved region G333.60 than in the young region G338.93. This trend in the DCN (3–2) emission morphology with the evolutionary stage is consistent across the full ALMA-IMF sample.

effects. We note that a few of the DCN (3–2) spectra (i.e. core 3, G338.93) show broad wings, which may indicate that it is tracing shocked gas (e.g. Busquet et al. 2017). Additional work is required, however, to understand the nature of the complex-type spectra fully and extract accurate fits, which is beyond this paper's scope. After filtering out the cores with a complex DCN (3–2) spectrum, the sample is reduced to 266 continuum cores, that is, ~45% of the continuum cores have a single component HFS fit.

We show examples of the single- and complex-type DCN (3–2) spectra in Figs. 9 and 10, respectively, extracted towards a sample of cores in the protocluster G338.93. In Table 3, we give an example of the resulting linewidth and V_{LSR} from the hyperfine fitting for G338.93. The linewidths are taken as σ obs $\times \sqrt{8 ln2}$, where σ obs is the observed velocity dispersion from single component HFS fits to the core-averaged, background-subtracted spectra. The full set of single- and complex-type spectra and tables for G338.93 and all protoclusters can be found in Appendix F. Towards G338.93, 26 of its 42 cores have DCN (3–2) detections (~62%), with 8 of these cores displaying complex spectra, thus after filtering, ~43% of the cores in G338.93 have a single-type DCN (3–2) detection. In the evolved region G333.60, 38 of its 52 cores have DCN (3–2) detections (~73%), with 10 of these cores displaying complex spectra, filtering out the complex-type spectra, ~54% of the cores have single-type detection. In Table 4, we show the detection rate of the DCN (3–2) fits for both the single- and complex-type spectra extracted from all cores in all protoclusters. We find that DCN (3–2) is detected more often in cores situated in evolved regions with an average detection rate of 62% for cores with single-type spectra, compared to a lower average detection rate (<35%) in the young and intermediate regions. This difference is seen whether

Table 3. Example of the DCN fits towards the first 15 cores of the young protocluster G338.93.

n [1]	Core [1] name	RA [1] [ICRS]	Dec [1] [ICRS]	F_A [1] [″]	F_B [1] [″]	PA [1] [deg]	T [K]	$V_{\rm LSR}$ [2] [km s^{-1}]	Linewidth [2] [km s^{-1}]	Spectral [3] type
1	250.1422011-45.6934028	16:40:34.13	−45:41:36.25	0.89	0.79	84	100 ± 50	−57.34 ± 0.08	–	Complex
2	250.1427268-45.6936217	16:40:34.25	−45:41:37.04	0.97	0.73	124	100 ± 50	−58.71 ± 0.08	–	Complex
3	250.1417044-45.7020244	16:40:34.01	−45:42:7.290	0.86	0.79	92	100 ± 50	−62.49 ± 0.03	–	Complex
4	250.1397543-45.6936984	16:40:33.54	−45:41:37.31	0.86	0.82	7	100 ± 50	−60.37 ± 0.04	–	Complex
5	250.1417392-45.7025004	16:40:34.02	−45:42:9.000	0.86	0.79	89	36 ± 7	−64.94 ± 0.02	2.19 ± 0.07	Single
6	250.1419183-45.7022799	16:40:34.06	−45:42:8.210	1.0	0.86	65	35 ± 10	−64.36 ± 0.01	2.98 ± 0.12	Single
7	250.1378537-45.7040233	16:40:33.08	−45:42:14.48	0.81	0.76	56	30 ± 6	–	–	–
8	250.1433977-45.6938542	16:40:34.42	−45:41:37.88	1.42	0.88	119	27 ± 6	−58.93 ± 0.03	1.81 ± 0.12	Single
9	250.1497218-45.6929092	16:40:35.93	−45:41:34.47	0.98	0.74	29	24 ± 5	–	–	–
10	250.1403862-45.7027264	16:40:33.69	−45:42:9.820	1.02	0.88	63	100 ± 50	−63.32 ± 0.07	–	Complex
11	250.1409277-45.6954519	16:40:33.82	−45:41:43.63	0.87	0.74	15	27 ± 6	−59.8 ± 0.05	0.95 ± 0.2	Single
12	250.1444989-45.69665	16:40:34.68	−45:41:47.94	1.99	1.75	16	24 ± 5	–	–	–
13	250.1423231-45.6931039	16:40:34.16	−45:41:35.17	1.06	1.04	129	29 ± 6	−57.29 ± 0.02	2.12 ± 0.09	Single
14	250.1394346-45.6928199	16:40:33.46	−45:41:34.15	0.87	0.7	72	28 ± 6	−59.26 ± 0.06	1.69 ± 0.17	Single
15	250.1461922-45.6894135	16:40:35.09	−45:41:21.89	1.68	1.26	124	24 ± 5	–	–	–

Notes. [1]The core numbering (n), core name, RA, Dec, position angle (PA), core major (F_A) and core minor (F_B) FWHM and dust temperatures (T) are taken from the smoothed core catalogues in Louvet et al. (2023), where the dust temperatures are those assumed for the core mass estimates presented in this work. [2]The $V_{\rm LSR}$ and linewidth are taken from the HFS fits. For reference, we include the $V_{\rm LSR}$ for the complex-type spectra, however, as the spectra are complex, often containing multiple components, we do not use them in the analysis or provide the linewidths. [3]Dashes are given for those cores with no DCN (3–2) detection.

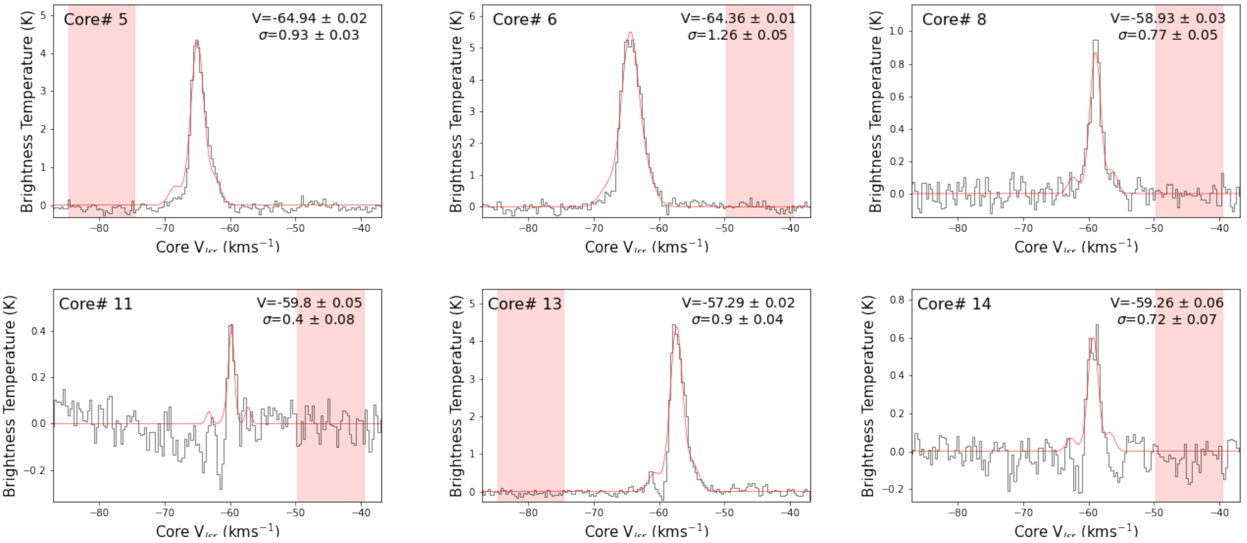

Fig. 9. Example of the core-averaged, background-subtracted DCN (3–2) single-type spectra for six cores in the young protocluster G338.93. The associated continuum core number is given in the top left of each panel (the core numbering is taken from Louvet et al. 2023). The core $V_{\rm LSR}$ (V) and velocity dispersion (σ) in units of km s^{-1} from the HSF fit are given in the top right. The line fit parameters for each core are also presented in Table 3. The pink-shaded region represents the part of the spectrum used to estimate the MAD noise.

the complex-type spectra are included or not, suggesting DCN detects a higher fraction of the continuum cores in the evolved protoclusters. This trend is in line with the more widespread detection of the DCN (3–2) emission in evolved protoclusters, as described in Sect. 4.1.

To assess if the background subtraction could bias the results, we also perform an extraction on the non-background subtracted DCN (3–2) spectra towards each core in Appendix E. While more cores are detected overall with single-type spectra (∼56%), DCN still detects a higher fraction of the continuum cores in evolved protoclusters (∼72%) compared with young and intermediate regions (<50%). We also note that the absorption features in several spectra may come from the background subtraction (e.g. core 2, G338.93). Absorption features are, however, still present in the non-background subtracted spectra and are likely a consequence of the missing short spacings in these 12m array only data.

4.4. Protocluster $V_{\rm LSR}$ estimates from the DCN (3-2) fits

In Table 4, we also provide the average $V_{\rm LSR}$ and velocity ranges for the detected cores in each protocluster using only the fits from single-type DCN (3–2) spectra. For most protoclusters, we find that the $V_{\rm LSR}$ estimates given in Table 1 (Motte et al. 2022) are consistent with the average centroid core $V_{\rm LSR}$ for each protocluster. For W51-IRS2, W43-MM2, and W43-MM3, however, there is a shift of 5–7 km s^{-1} between the average core $V_{\rm LSR}$ and that of the $V_{\rm LSR}$ estimates from Motte et al. (2022). The shift

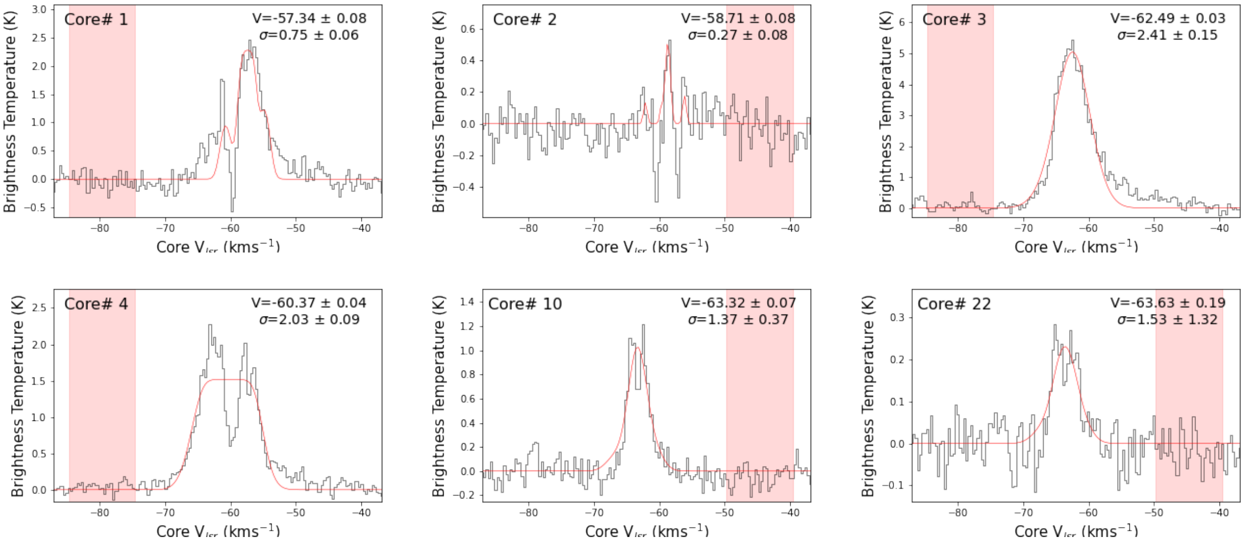

Fig. 10. Example of the core-averaged, background-subtracted DCN (3–2) complex-type spectra for six cores in the young protocluster G338.93. The associated continuum core number is given in the top left of each panel (the core numbering is taken from Louvet et al. 2023). The core $V_{\rm LSR}$ (V) and velocity dispersion (σ) in units of km s^{-1} from the HSF fit are given in the top right. Given the complex structure in their spectra, the resulting fits are excluded from the analysis and labelled as complex-type spectra. The pink-shaded region represents the part of the spectrum used to estimate the MAD noise.

Table 4. Characteristic parameters of the DCN (3–2) hyperfine fits.

Protocluster cloud name	Number [(1)] of cores	Number [(2)] detected (complex)	Detection [(2)] rate [%] (complex)	Velocity [(3)] range [km s^{-1}]	$V_{\rm LSR}$ [(3)] mean [km s^{-1}]	$V_{\rm LSR}$ [(3)] std [km s^{-1}]	Linewidth [(3)] mean [km s^{-1}]	Linewidth [(3)] median [km s^{-1}]	Linewidth [(3)] std [km s^{-1}]
Young									
G327.29	32	13 (17)	41 (53)%	5.7	−45.1	1.9	1.3	1.3	0.3
G328.25	11	3 (4)	27 (36)%	2.5	−42.7	1.0	2.0	1.2	1.2
G338.93	42	18 (26)	43 (62)%	7.7	−61.0	2.0	1.6	1.6	0.7
G337.92	22	8 (15)	36 (68)%	3.9	−39.2	1.3	2.3	2.0	1.2
W43-MM1	70	15 (29)	21 (41)%	7.0	98.5	2.1	1.1	0.9	0.5
W43-MM2	40	18 (25)	45 (62)%	4.7	91.1	1.4	1.4	1.3	0.5
Average	36	12 (19)	35 (53)%	5.2		1.9	1.5	1.3	0.8
Total	217	75 (116)							
Intermediate									
G351.77	18	4 (13)	22 (72)%	6.0	−3.9	2.4	1.4	1.5	0.3
G353.41	45	14 (15)	31 (33)%	7.6	−17.4	1.9	1.4	1.1	0.7
G008.67	19	9 (13)	47 (68)%	7.3	35.9	2.5	1.5	1.4	0.5
W43-MM3	36	9 (13)	25 (36)%	4.6	92.8	1.4	1.4	1.2	0.7
W51-E	23	7 (10)	30 (43)%	11.7	56.2	4.5	1.8	2.0	0.7
Average	28	9 (13)	30 (45)%	7.4		2.9	1.5	1.3	0.6
Total	141	43 (64)							
Evolved									
G333.60	52	28 (38)	54 (73)%	10.4	−47.8	2.2	1.3	1.2	0.4
G010.62	42	28 (34)	67 (81)%	10.1	−2.7	2.4	1.1	1.1	0.3
G012.80	46	37 (38)	80 (83)%	7.4	36.0	1.5	1.3	1.2	0.6
W51-IRS2	97	55 (67)	57 (69)%	13.7	61.8	2.4	1.2	1.1	0.5
Average	59	37 (44)	62 (75)%	10.4		2.3	1.2	1.1	0.5
Total	237	148 (177)							

Notes. [(1)]The number of continuum cores is taken from the smoothed core catalogue from Louvet et al. (2023). We note that four cores in the sample overlap: two cores from W51-E (cores 20 and 30) overlap with two cores in W51-IRS2 (cores 22 and 38), and two cores in W43-MM2 (cores 10 and 46) overlap with two cores in W43-MM3 (cores 2 and 37). However, as they are either non-detections or complex-type spectra, we do not explicitly assign them to a given field as done in Louvet et al. (2023). [(2)]The number of cores detected and the detection rates (given in percentages) are for single-type DCN detections. The numbers within the brackets are for the sum of the single- and complex-type DCN detections. Spectra described as complex-type spectra are not well fit by a single component. We provide the percentages and number of detections, but cores with a complex-type spectrum are not included in the estimates of the velocity range, $V_{\rm LSR}$, or linewidth. [(3)]Only single-type DCN spectra (fit with a single component) and listed as single in the Tables of the DCN fits (e.g. Table 3) are included in the estimates of the velocity ranges, $V_{\rm LSR}$ and linewidth for each protocluster.

in W51-IRS2 is likely due to the two distinct velocity distributions of its cores (which can be seen in the moment maps for W51-IRS2 in Fig. D.1) and has been observed previously (Ginsburg et al. 2015). Furthermore, both W43-MM2 and W43-MM3 reside in the same complex (W43), along with W43-MM1, and the few km s^{-1} velocity offset in these regions is likely due to differences between the average bulk motions on larger scales compared to the internal motions of the embedded protoclusters. The $V_{\rm LSR}$ distribution for the cores situated within a given region span a range of values from $2.5 < \Delta v_{\rm LSR} < 13.7$ km s^{-1}; however, the higher values are produced by outliers (see Fig. 11). In Fig. 11, we display the distribution of the core velocities per evolutionary stage. We estimate the velocity offset for each core by taking the central velocity of the fit and subtracting from it the average protocluster velocity (estimated from the average of the DCN (3–2) moment 1 maps). While the evolved protoclusters have cores with a larger velocity spread, that sample is dominated by the protocluster W51-IRS2, which likely has two distinct velocity distributions for its cores. Thus, we find no apparent difference in the spread of the core $V_{\rm LSR}$ with the evolutionary stage of the host region.

4.5. Comparison with other molecular lines

We compare here the DCN (3–2) emission extracted towards the protocluster G338.93 to other molecular lines (situated within the ALMA-IMF spectral coverage) that have previously been used to study core properties and kinematics, such as DCO$^+$ (3–2), ^{13}CS (5–4), OCS (19–18), C^{18}O (2–1), and N$_2$D$^+$ (3–2) (e.g. Li et al. 2022; Sakai et al. 2022; Nony et al. 2020; Cunningham et al. 2016; Maud et al. 2015). They are fitted and classified as single- or complex-type spectra in the same way as for DCN (3–2) (described in Sect. 4.3), but using only a single component Gaussian fit in pyspeckit. To be consistent, for lines (e.g. DCO$^+$) situated in spectral windows with higher spectral resolution than B6 spectral window 1, we smooth these cubes to have the same spectral resolution as DCN. In Table 5, we show the detection rate of several molecular transitions towards the core population of G338.93 along with their critical densities and the energies of their respective lower level above ground (in K). DCN (3–2) exhibits single-type spectra towards the highest percentile (~43%) of continuum cores in G338.93, versus 5–31% for the other species. While C^{18}O (2–1) is detected towards 1.3 times more cores overall (~81%), a large fraction of those spectra (62%) contains complex-type spectra, which exhibit multiple peaks or non-Gaussian profiles (see Sect. 4.3). In Fig. 12, we show the extracted linewidths for each molecular species as a function of the associated continuum core masses (taken from Louvet et al. 2023) for the protocluster G338.93. DCN (3–2) is extracted with a single-type spectrum across the majority of the mass distribution of the cores. In comparison, ^{13}CS (5–4) and OCS (19–18) are found predominantly towards the higher-mass continuum cores. Meanwhile, N$_2$D$^+$ (3–2) and DCO$^+$ (3–2) trace cores in the low/intermediate mass range with a single-type spectrum. We note that several of the lowest mass cores in this region are not traced by DCN (3–2), but are traced by either C^{18}O (2–1), N$_2$D$^+$ (3–2) and DCO$^+$ (3–2), thus, DCN (3–2) may not be sensitive to the lowest mass cores (see Sect. 5.4 for further discussion). Furthermore, N$_2$D$^+$ (3–2) predominantly traces different cores than DCN (3-2) in G338.93 and could provide a complementary tracer of the low/intermediate mass core population. For the ALMA-IMF protoclusters, N$_2$D$^+$ may not be the optimal tracer of high-mass prestellar cores, contrary to the picture in infrared dark clouds (e.g. Tan et al. 2013, Barnes et al. 2023) where N$_2$D$^+$ is observed towards massive prestellar cores. While Fig. 12 highlights the need for a multi-line analysis to recover the full core population in these protoclusters, such a task is beyond the scope of this paper. It will be performed on individual regions in the future (e.g. Cunningham et al., in prep.). DCN (3–2) recovers the highest percentage of continuum cores with single-type spectra compared to other dense gas tracers. Thus, using only a single tracer, DCN (3–2) likely still provides the best proxy of the dense gas associated with the continuum cores in the ALMA-IMF bandwidth coverage.

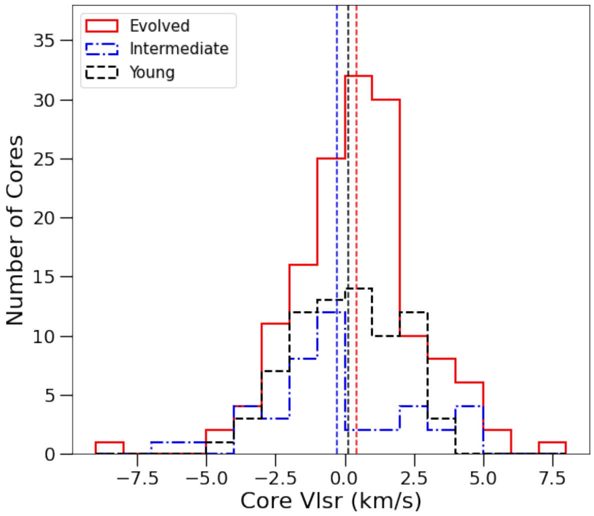

Fig. 11. Distribution of the core velocities from the DCN line fits split by evolutionary stage. The velocity offset is determined as the central velocity of the fit and subtracting from it the average protocluster velocity (estimated from the average of the DCN (3–2) moment 1 maps). The vertical dashed lines are the average values for each subgroup (0.13 km s^{-1}, −0.29 km s^{-1}, and 0.44 km s^{-1} for the young, intermediate and evolved regions, respectively). We find no obvious dependence on the distribution of the core velocities over the sample.

5. Discussion

5.1. Global DCN (3–2) morphology and kinematics

The DCN (3–2) emission displays a diversity of morphology and velocity structure across the ALMA-IMF fields. For the evolved regions, the emission traces more elongated, filamentary structures (e.g. W51-IRS2, G333.60, and G012.80) compared with more compact and less elongated emission for the young protoclusters (e.g. G328.25, and G338.93). The difference may be caused by a time evolution of density and temperature, where the evolved regions have had more time to concentrate gas, reaching temperatures and densities sufficient to produce DCN (3–2) emission, perhaps due to the development of expanding H II regions in the evolved protoclusters, which adds heating and compression and can shape their surrounding cloud (such as in G5.89-0.39, Fernández-López et al. 2021). The DCN (3–2) moment 1 maps display a broad range of velocity dispersion across the protoclusters, typically around 12 km s^{-1} and up to 16 km s^{-1} in W51-IRS2. We use here the spread of core velocities and the global DCN (3–2) emission to identify two protoclusters in the sample, W51-IRS2 and W51-E, which likely consist of multiple clouds along the line of sight that may not be spatially coherent structures in position-velocity space (e.g. Ginsburg et al. 2015).

Table 5. Comparison of molecular line detection towards the continuum core population of G338.93.

Molecule	Transition	Frequency [1]	E_u/k_b [1]	Critical density [1]	Cores detected [2]		Percentage (%)	
		[GHz]	[K]	$n_{\rm crit}$ [cm^{-3}]	Single	Complex	Single	Complex
DCO^+	3–2	216.113	20.7	$2.4{\times}10^6$	5	8	12	20
$OC^{33}S$	18–17	216.147	98.6	$1.3{\times}10^6$	2	1	5	2
DCN	3–2	217.238	20.9	$1.8{\times}10^7$	18	8	43	19
$C^{18}O$	2–1	219.560	15.8	$9.9{\times}10^3$	13	21	31	50
OCS	19–18	231.061	110.9	$4.9{\times}10^5$	6	10	14	24
^{13}CS	5–4	231.220	33.3	$4.3{\times}10^6$	3	7	7	17
N_2D^+	3–2	231.322	22.2	$3.6{\times}10^6$	8	2	19	5

Notes. (1)The rest frequencies were taken from the Cologne Database for Molecular Spectroscopy (CDMS). The temperatures and critical densities for OCS, $OC^{33}S$, $C^{18}O$ and ^{13}CS are taken from Molet et al. (2019). For DCN (3-2), we take the values from Bosco et al. (2019) and for N_2D^+, DCO^+ we follow Bosco et al. (2019) and approximate the critical density assuming $n_{\rm crit} \approx A/\Gamma$ (Shirley 2015), for collisional rates at T = 100 K where the Einstein A and Γ coefficients are taken from the Leiden Atomic Molecular Database (LAMBDA; Schöier et al. 2005). N_2D^+ is approximated by the values for N_2H^+. (2)Number of continuum cores that have a background-subtracted spectrum which is well represented by either a single Gaussian component fit (single) or has a spectrum that consists of multiple components or is too complex to fit with a single component Gaussian (complex). The total number of continuum cores in G338.93 is 42. In the case of DCN (3–2), we use the adapted single-component HFS to fit the spectra.

5.2. Core distribution and kinematics in individual protoclusters

In Fig. 13, we show the positions of the detected cores and their respective core $V_{\rm LSR}$ and linewidths overlaid on their DCN (3–2) moment 0 contour maps for the two example protoclusters, G338.93 and G333.60. The entire sample is shown in Appendix G. We estimate their core-to-core velocity dispersions (i.e. the standard deviation of the core $V_{\rm LSR}$) and find values of ~2 km s^{-1} for both the young (G338.93) and evolved (G333.60) regions. In G338.93, however, the cores with DCN (3–2) detections are distributed in two separated ≲0.5 pc size hubs with different average bulk velocities, −60.2 km s^{-1} and −62.6 km s^{-1} for the north and south hub, respectively, compared to the global average of −61 km s^{-1}. If we consider these core populations separately, the estimated core-to-core velocity dispersion is smaller ~1.5 km s^{-1}. In G333.60, the distribution of the detected cores is more widespread, over ~3 pc. While it is less obvious to split the cores based on the DCN (3–2) emission, if we split the cores into three subgroups, the central ~0.5 pc and the two filaments in the north-east and south-west, we obtain core-to-core velocities of ~1.2 km s^{-1}, ~1.9 km s^{-1}, ~1.0 km s^{-1}, respectively. We find no striking difference between the two regions, however, depending on how the cores are grouped, the core-to-core velocities can change by up to a factor of 2. The core-to-core velocity dispersions for the sub-groups in G338.93 and G333.60 are still larger than nearby star-forming regions (e.g. <0.6 km s^{-1} Kirk et al. 2010), but they are in line with those found by Cheng et al. (2020) in the massive star-forming region, G286, on similar ~1 pc scales.

Furthermore, if we consider the DCN (3–2) linewidths of cores situated within the two <0.5 pc size hubs in G338.93, we find an average linewidth with a standard deviation of ~1.6 km s^{-1} and ~0.7 km s^{-1}, respectively, whereas the cores outside of these main hubs (which are low and intermediate-mass) are not detected. Towards the evolved protocluster G333.60, around the central ~0.5 pc close to the positions of the known H II region (e.g. Fujiyoshi et al. 2006), the linewidths are similar to G338.93 (average and standard deviation of ~1.5 km s^{-1} and ~0.5 km s^{-1}, respectively) or associated with complex-type spectra (green points). In contrast, cores with a DCN (3-2) detection outside of the central region are typically lower-mass and situated along the filamentary structures and have smaller linewidths (with an average and standard deviation of ~1.2 km s^{-1} and ~0.3 km s^{-1}, respectively).

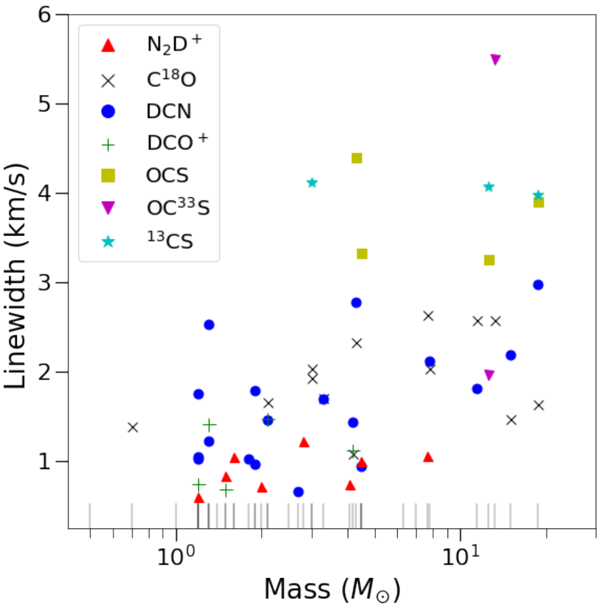

Fig. 12. Linewidths extracted towards the core population of G338.93 for the molecules listed in Table 5 as a function of the continuum core masses taken from Louvet et al. (2023), assuming the core dust temperature estimates as given in Table 3. The linewidths shown are from fits classified as single-type which can be well approximated by a single Gaussian (or single HFS fit for DCN) component fit to the extracted spectrum. The grey vertical lines represent the masses of all 42 cores in the G338.93 protocluster. DCN (3–2) well represents the full mass range of the cores in the protocluster.

5.3. Core kinematics and distribution with evolutionary classification

5.3.1. Core-to-core velocity distribution

In Fig. 14, we plot the core-to-core velocity dispersion vs the spatial spread (following, e.g. Stutz & Gould 2016) for each core grouped by their host region's evolutionary stage. The radial

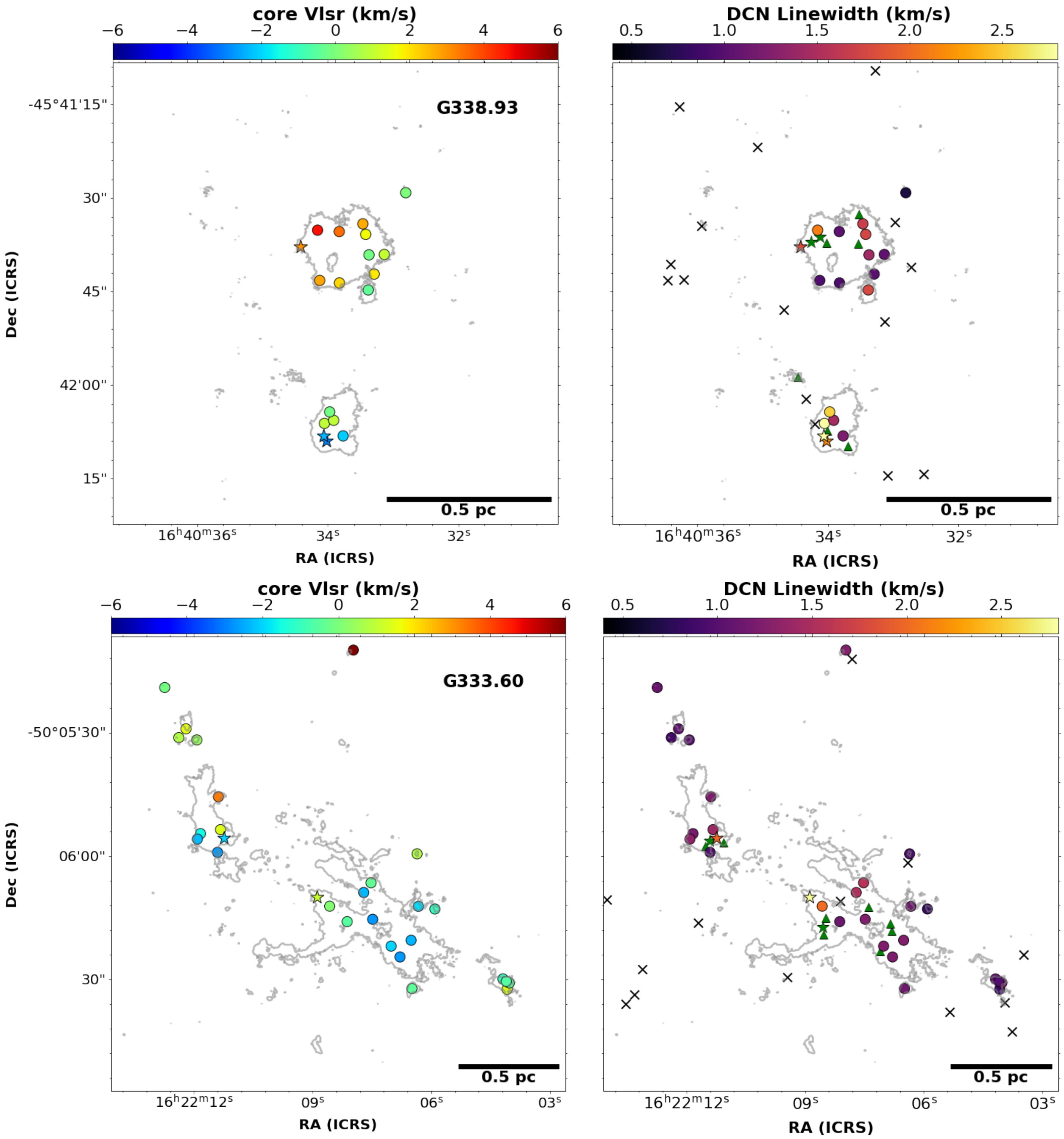

Fig. 13. Core $V_{\rm LSR}$ (left) and DCN (3–2) linewidths (right) estimated from the DCN (3–2) fits to the continuum cores towards examples of a young and an evolved protocluster G338.93 (top) and G333.60 (bottom), respectively. The circles and stars represent the detected cores with mass estimates below and above 8 $M_\odot$, respectively, with the colour scale displaying the fitted parameters from the DCN (3–2) fits (left: core $V_{\rm LSR}$, right: linewidth). The core $V_{\rm LSR}$ is the centroid velocity of the DCN (3–2) fit minus the cloud $V_{\rm LSR}$ (taken as −62 km s^{-1}, and −47 km s^{-1} for G338.93, and G333.60, respectively). The grey contours are the 4σ level of the DCN (3–2) moment 0 map. In the right panels, the positions of cores without a DCN (3–2) detection are marked with a black cross and with a black star for cores with a mass estimate below and above 8 $M_\odot$, respectively, and green triangles and stars represent cores with a complex-type DCN (3–2) spectra, with a mass estimate below and above 8 $M_\odot$, respectively.

spatial offset for each core is determined by taking the position of the core and subtracting from it the mean position of all cores in its protocluster and assuming the distances given in Table 1 for each region. The velocity offset for each core is determined by subtracting the centroid $V_{\rm LSR}$ found from all cores with single-type spectra in a given region from it. We find core-to-core velocity dispersions of 1.8 ± 0.2 km s^{-1}, 2.6 ± 0.4 km s^{-1}, and 2.2 ± 0.2 km s^{-1} for the young, intermediate, and evolved protoclusters, respectively. This suggests that the young protoclusters have a slightly smaller core-to-core velocity dispersion compared with the intermediate and evolved protoclusters; however, a Kolmogorov-Smirnov (KS) test between the core-to-core velocities of the evolutionary stages does not give $P_{\rm values} < 0.05$. Furthermore, as discussed in Sect. 5.2 for G338.93, and G333.60, the core-to-core velocities can change by a factor of 2 depending on how cores are separated. Thus, we would need to separate the cores spatially and by velocity in each region to assess the core-to-core velocity and spatial distribution fully. In

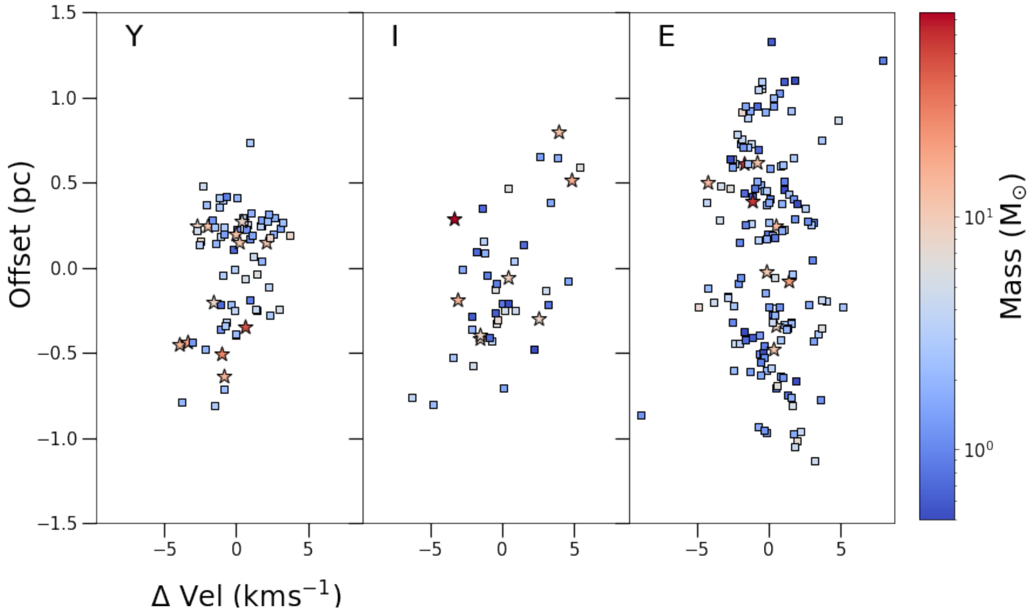

Fig. 14. Core $V_{\rm LSR}$ vs the core radial offset grouped by evolutionary classification of the host protocluster; young, intermediate and evolved (Y: left, I: centre, and E: right, respectively). The radial spatial offset for each core is determined by taking the position of the core and subtracting from it the mean position of all cores in its protocluster and assuming the distances given in Table 1 for each region. The velocity offset for each core is determined by subtracting the centroid $V_{\rm LSR}$ found from all cores with single-type spectra in a given region from it. The cores are colour-coded by their mass estimates taken from Louvet et al. (2023), and star symbols represent those cores with mass estimates $>8\,M_\odot$. Cores with a declination smaller than the average position have a negative offset. For the young and intermediate regions, the spatial distribution of the cores is more compact compared to cores in evolved protoclusters, where the cores can be spatially distributed over larger areas (>2.0 pc).

Fig. 14, we also find that the most massive cores (red stars) are not necessarily at the central velocity or average central position of the protocluster, although we have a small number of statistics for the most massive cores. However, this also depends on how the cores are sub-clustered in a given protocluster. A complete analysis of the core-to-envelope dispersion will be done in future works, along with the separation of cores in individual protoclusters to estimate the core-to-core velocities more accurately.

Figure 14 highlights again that the cores in evolved protoclusters have a more widespread spatial distribution than those in the young and intermediate regions. The standard deviation of the spatial spread for the young, intermediate, and evolved regions are 0.33 pc, 0.39 pc, and 0.60 pc, respectively, with standard errors <0.06 pc. A KS test on the core offsets in the young and intermediate regions suggests they are drawn from a different population than cores in evolved regions. Thus, the cores detected in DCN (3–2) are typically more concentrated in the young and intermediate regions. This is also the case if we consider the full core populations, not just those with DCN (3–2) detections. This suggests that the spatial distribution is inherent to the evolutionary stage and not biased by the cores with DCN (3–2) detections. Furthermore, we find that cores with large spatial offsets in evolved regions (i.e. >0.5 pc) are predominantly lower mass. As discussed above, this depends on where the spatial centre of the protocluster is defined and if the cores are further sub-clustered. However, if we take ten random cores in each protocluster as the central position, the evolved protoclusters always have larger standard deviations in their spatial spread, which is significant with a KS-test. Thus, the larger values are likely not due to a bias in the definition of the cluster centre. A full assessment of the sub-clustering or separation of core populations as done in (e.g. Pouteau et al. 2023) should be performed to confirm this.

5.3.2. DCN (3–2) linewidths

Considering the DCN (3–2) linewidths grouped by evolutionary classification, we find slightly smaller average linewidths in the evolved regions of ~1.2 km s^{-1} compared to the young and intermediate protoclusters of ~1.5 km s^{-1}, and standard deviations of ~0.5, and ~0.7 km s^{-1} respectively. In Fig. 15, we show the histogram of the DCN (3–2) linewidths extracted from the continuum cores as a function of the evolutionary stage. Furthermore, a KS test on the DCN (3–2) linewidths of those cores situated in the evolved regions, when compared with the DCN (3–2) linewidths of cores from intermediate + young regions, gives a $P_{\rm values} < 0.001$, suggesting that they are not drawn from the same population. We note, however, that we do not have linewidth estimates with DCN (3–2) for all cores, thus, this trend would need to be confirmed with additional lines.

While evolved protoclusters are typically at a slightly larger distance (~4.2 kpc) compared with the young and intermediate regions (~3.7 kpc), as our data are taken at a constant linear resolution, there is no reason to expect differences in the linewidths with protocluster distance, as shown in Fig. 15. Furthermore, if we consider the size-linewidth relation, we may expect an increase in the DCN linewidths with the core size. In Fig. 16, we show the non-thermal velocity dispersion-size relation for the 266 cores in our sample from all 15 protoclusters, where the non-thermal velocity dispersion ($\sigma_{\rm NT}$) is estimated assuming:

$$\sigma_{\rm NT} = \sqrt{\sigma^2 - \frac{kT_k}{\mu m_{\rm H}}},$$

where k is the Boltzmann constant, T_k is the gas kinetic temperature used for DCN (3–2), which is taken to be equal to the dust temperature assumed by Louvet et al. (2023) and has a range from 18 K to be 300 K for all cores (the assumed temperatures

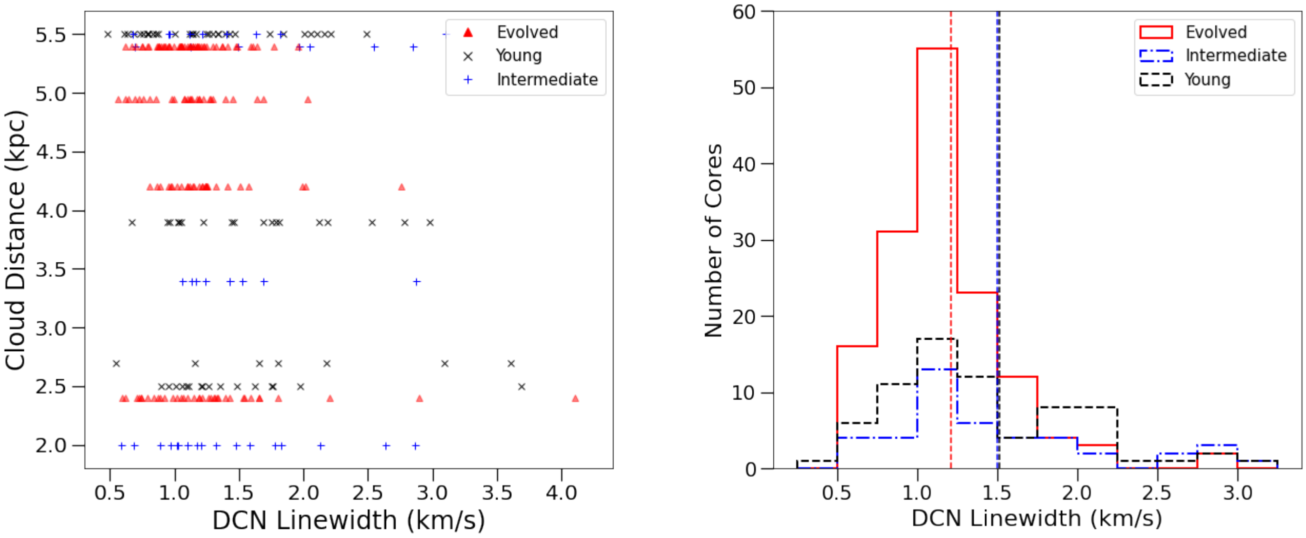

Fig. 15. Distribution of the core linewidths from DCN single-type line fits as a function of protocluster distance (left). The red triangles, blue plusses, and black crosses represent the linewidths of core emission associated with evolved, intermediate, and young protoclusters, respectively. There is no obvious dependence on the protocluster distance and the linewidths. Right: Histogram of the linewidths from the DCN line fits grouped by evolutionary stage, where the solid red, blue dot-dashed, and black dashed lines represent the evolved, intermediate, and young protoclusters, respectively. The vertical lines display the mean linewidth for each evolutionary stage with the same colours described above. The evolved regions have a slightly smaller average linewidth (1.2 km s^{-1}) than young and intermediate regions (~1.5 km s^{-1}), significant within the standard errors.

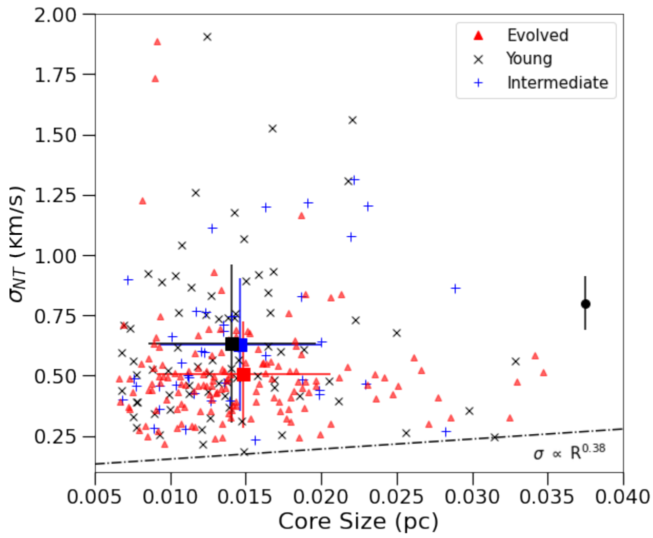

Fig. 16. Distribution of the core-size as a function of the respective non-thermal velocity dispersion from the DCN (3-2) spectra. The red triangles, blue plusses, and black crosses represent evolved, intermediate, and young protoclusters, respectively. The red, blue, and black squares are the average values (0.50 km s^{-1}, 0.63 km s^{-1}, and 0.63 km s^{-1}) for the collective evolved, intermediate and young values, respectively, where the error bars represent the standard deviations (0.22 km s^{-1}, 0.27 km s^{-1}, and 0.33 km s^{-1}, respectively). The black dashed line is the Larson relation (Larson 1981), and nearly all cores are above it. The black circle and error bar provide an estimate of the typical errors on the linewidth estimates. We find no correlation between the non-thermal velocity dispersion with core-size in the ranges of values sampled here.

for individual cores are shown in, e.g. Table 3), $m_{\rm H}$ is the hydrogen mass, and μ is the molecular weight of the DCN molecule. The core sizes are the geometric mean of the major and minor continuum core FWHMs from Louvet et al. (2023) deconvolved by the smoothed beam[15]. We fit Pearson's correlation coefficient (ρ), which measures the linear correlation between two variables, and find a value of 0.18, indicating no correlation exists between the dispersion and core sizes in these data. A similar lack of correlation between the non-thermal velocity dispersion and radius was found by Traficante et al. (2018) towards a sample of Hi-Gal clumps, albeit on the larger size scales of 0.1-1 pc. If we consider the different evolutionary stages independently, there is similarly no correlation for any individual subgroup. However, we note that we are sampling a very small range of core sizes (i.e. a factor of ~3).

5.4. Nature of the core population traced by DCN (3-2)

In Fig. 17, we show the distribution of core masses taken from Louvet et al. (2023; assuming the core dust temperature estimates as given in e.g. Table 3) separated by their DCN classification (i.e. single-, complex-type and non-detected). We find that the complex-type spectra are typically extracted in cores with higher masses and densities on average (~17 $M_{\odot}$, and ~2.5×10^7 $\rm cm^{-3}$, respectively) than those with single-type DCN (3-2) spectra (~5 $M_{\odot}$, and ~1×10^7 $\rm cm^{-3}$, respectively). Since complexity is associated with higher mass cores, we suggest the complex-type spectra may be caused by high optical depths, either through self-absorption of the line or absorption of the background continuum. However, the presence of multiple velocity components cannot be ruled out. If we consider the non-detected cores, the average masses and densities are slightly lower, ~3 $M_{\odot}$, and ~$0.8 \times 10^7 \rm cm^{-3}$, respectively. Moreover, there is a higher proportion of non-detected cores with masses less than a few $M_{\odot}$ in the young and intermediate regions than the evolved protoclusters. As shown previously, towards the young protocluster, G338.93 (see Fig. 12), DCN (3–2) is not detected towards cores with masses below ~1 $M_{\odot}$, which could indicate a sensitivity

---

[15] Unless the deconvolved size is less than half of the smoothed beam size, then the non-deconvolved source size is used.

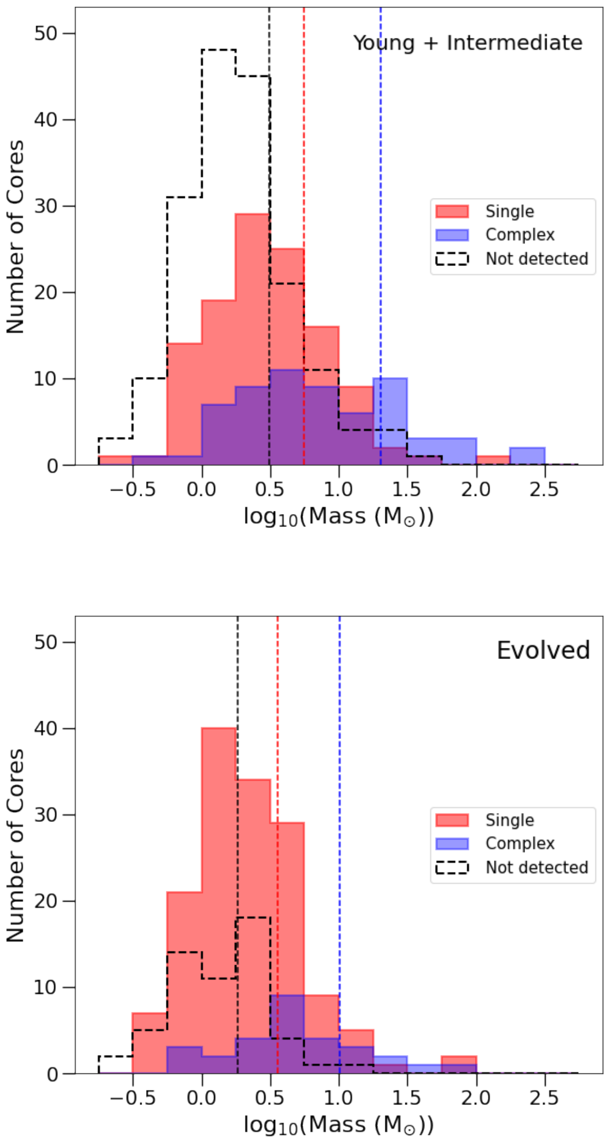

Fig. 17. Histograms of the mass distribution (in log scale) of the cores in the combined young + intermediate regions (top panel) and evolved regions (bottom panel). The shaded red and blue areas show the cores with single-type DCN (3–2) and complex-type spectra, respectively. The dashed black line represents cores with a DCN (3–2) non-detection. The red, blue, and black dashed vertical lines represent the average mass values (top: 5.6 $M_\odot$, 20.1 $M_\odot$, and 3.1 $M_\odot$; bottom: 3.6 $M_\odot$, 10.2 $M_\odot$, and 1.8 $M_\odot$) for the single-, complex-type, and non-detections, respectively. We find that the complex-type cores have an average mass nearly an order of magnitude higher than those without a DCN (3–2) detection and around three times higher than cores with a single-type DCN detection, regardless of evolutionary class.

bias for the lowest mass cores. We note that in G338.93, several of the lowest mass cores that are not detected by DCN (3–2) are, however, detected in other species (i.e. N_2D^+ (3–2) at ~1 $M_\odot$). If we consider recent DCN (3–2) observations by Hsieh et al. (2023) towards SVS13A, a low mass protobinary system harbouring two subsolar protostars at 293 pc, where they find peak brightness temperatures of around 15 K, we would not be sensitive to those cores at the distance of G338.93. We would expect, however, to detect them towards the ALMA-IMF protoclusters at distances <3kpc (e.g. G337.92), suggesting that a sensitivity bias does not account for all of the non-detected low mass cores. Furthermore, if we include all non-detected cores with a mass below 1 $M_\odot$ into the detected core statistics, the evolved protoclusters would still have ~27% more DCN (3–2) detections. While the sensitivity limit has an impact on the DCN (3–2) detections and should be explored further, it does not fully explain the higher fraction of cores with a DCN detection in the evolved regions.

The detection of a deuterated species is typically associated with cold temperatures and high densities (e.g. Roberts & Millar 2000); however, DCN can form through both cold and high-temperature reaction channels, with reactions at higher temperatures being the dominant pathway (e.g. Turner 2001; Roueff et al. 2013). The abundance of DCN is enhanced in warmer gas up to and even above 70K (e.g. Millar et al. 1989; Turner 2001, Roueff et al. 2007, 2013). Thus, unlike other deuterated species such as N_2D^+, where the abundance is enhanced in the cold (<25 K) dense environments, (where CO is frozen out) and destroyed in higher temperatures, DCN (3–2) emission also traces warmer gas. The higher number of DCN (3–2) detected cores in evolved protoclusters may be due to temperature, with the evolved regions having higher temperatures over a larger fraction of the cloud than young and intermediate regions. Perhaps due to the presence of H II regions in the evolved protoclusters, which can add heating and compression in the surrounding cloud. We should also note the possibility that DCN enhancement may result from sputtering. In particular, for high-mass protostellar cores with powerful outflows and shocks, DCN emission frozen in the dust grains could be released back to the gas phase by the passage of strong shocks (e.g. Busquet et al. 2017).

Cores with an N_2D^+ (3–2) detection but without a DCN detection are typically located outside the central hubs in G338.93 and may be in colder, more quiescent parts of the clouds. This has been observed in other works (e.g. Tatematsu et al. 2020; Cheng et al. 2020, Li et al. 2022; Sakai et al. 2022) where the spatial distribution between DCN (3–2) and N_2D^+ (3–2) is observed to be different. Sakai et al. (2022) found DCN (3–2) traced regions associated with more active signs of ongoing star formation, compared to N_2D^+ (3–2), which they observed to be tracing the more quiescent, colder regions in their sample of infrared dark clouds. This spatial dichotomy between DCN (3–2) emission and N_2D^+/DCO^+ was similarly found in the young massive star-forming region G286 (Cheng et al. 2020) where they identified the DCN emission to be again concentrated around the more active, likely warmer parts of the cloud compared with other deuterated species. To assess the dichotomy and nature of the cores fully across the ALMA-IMF regions requires a multi-line analysis, which will be performed in future works (e.g. Cunningham et al., in prep.).

6. Summary

We have presented an overview of the calibration and imaging steps performed to produce the full set of ALMA-IMF 12m-only line cubes provided as part of the DR1 release with this paper. We have described the internal ALMA-IMF data pipeline available on the ALMA-IMF GitHub. We used the custom ALMA-IMF pipeline to produce a homogeneous and reproducible set of imaged line cubes for the 12 spectral windows and 6.7 GHz of total spectral coverage, containing a multitude of key molecular tracers that will provide a lasting legacy value to the community.

In addition, we provide an overview of the DCN (3–2) emission across the ALMA-IMF protoclusters, where the global DCN (3–2) emission displays a diversity of morphologies and kinematics across the sample, tracing more widespread, filamentary structures in the evolved regions, compared to young protoclusters where the DCN emission is found in more compact hub-type structures. We also extracted the DCN spectra from the 595 continuum cores, where DCN (3–2) emission is detected in ~60% of the continuum cores, of which ~45% have a single-type DCN spectrum. The evolved protoclusters have a higher percentage of DCN-detected cores, suggesting that the DCN (3–2) transition is likely a more complete tracer of the core population in evolved protoclusters. Furthermore, the cores with DCN (3–2) detections in evolved regions tend to be more spatially extended over the region than in the younger protoclusters. This may be due to the time evolution of the gas temperature and density, where the evolved regions are warmer over a larger portion of the cloud. We provide first estimates of the core linewidths and core $V_{\rm LSR}$ from the DCN (3–2) fits and find an average core-to-core velocity and linewidth for cores with single-type DCN spectra of ~2.2 km s^{-1} and ~1.3 km s^{-1}, respectively, across the 15 protoclusters. We find no obvious difference between the average core-to-core velocities and only a tentative difference in linewidths with the protocluster evolutionary stage. This may, however, be biased by the fact that we do not have estimates for all of the cores.

Acknowledgements. We are grateful to the anonymous referee for their comments which improved this manuscript. This paper makes use of the following ALMA data: ADS/JAO.ALMA 2017.1.01355.L, 2013.1.01365.S, and 2015.1.01273.S. ALMA is a partnership of ESO (representing its member states), NSF (USA) and NINS (Japan), together with NRC (Canada), MOST and ASIAA (Taiwan), and KASI (Republic of Korea), in cooperation with the Republic of Chile. The Joint ALMA Observatory is operated by ESO, AUI/NRAO and NAOJ. This work and N.C. have received funding from the European Research Council (ERC) via the ERC Synergy Grant ECOGAL (grant 855130), from the French Agence Nationale de la Recherche (ANR) through the project COSMHIC (ANR-20- CE31-0009). The project leading to this publication has received support from ORP, which is funded by the European Union's Horizon 2020 research and innovation programme under grant agreement No 101004719 [ORP]. A.G. acknowledges support from the National Science Foundation under grants AST-2008101 and CAREER 2142300. T.Cs. has received financial support from the French State in the framework of the IdEx Université de Bordeaux Investments for the future Program. R.G.-M. acknowledges support from UNAM-PAPIIT project IN108822 and from CONACyT Ciencia de Frontera project ID: 86372. A.S. gratefully acknowledges support by the Fondecyt Regular (projectcode 1220610), and ANID BASAL projects ACE210002 and FB210003. R.A. gratefully acknowledges support from ANID Beca Doctorado Nacional 21200897. T. B. acknowledges the support from S. N. Bose National Centre for Basic Sciences under the Department of Science and Technology, Govt. of India. M.B. has received financial support from the French State in the framework of the IdEx Université de Bordeaux Investments for the future Program. S.B. acknowledges support by the French Agence Nationale de la Recherche (ANR) through the project *GENESIS* (ANR-16-CE92-0035-01). A.L.S. and Y.P. acknowledge funding from the European Research Council (ERC) under the European Union's Horizon 2020 research and innovation programme, for the project 'the Dawn of Organic Chemistry' (DOC), grant agreement No 741002. G.B. acknowledges support by the grant PID2020-117710GB-I00 (MCI-AEI-FEDER,UE).

References

Alves, J., Lombardi, M., & Lada, C. J. 2007, A&A, 462, L17
Ballesteros-Paredes, J., André, P., Hennebelle, P., et al. 2020, Space Sci. Rev., 216, 76
Barnes, A. T., Liu, J., Zhang, Q., et al. 2023, A&A, 675, A53
Bastian, N., Covey, K. R., & Meyer, M. R. 2010, ARA&A, 48, 339
Bonfand, M., Csengeri, T., Bontemps, S., et al. 2023, A&A, submitted
Bosco, F., Beuther, H., Ahmadi, A., et al. 2019, A&A, 629, A10
Brouillet, N., Despois, D., Molet, J., et al. 2022, A&A, 665, A140
Busquet, G., Fontani, F., Viti, S., et al. 2017, A&A, 604, A20
Cheng, Y., Tan, J. C., Liu, M., Lim, W., & Andersen, M. 2020, ApJ, 894, 87
Codella, C., Ceccarelli, C., Chandler, C., et al. 2021, Front. Astron. Space Sci., 8, 227
Csengeri, T., Bontemps, S., Wyrowski, F., et al. 2017a, A&A, 600, L10
Csengeri, T., Bontemps, S., Wyrowski, F., et al. 2017b, A&A, 601, A60
Cunningham, N., Lumsden, S. L., Cyganowski, C. J., Maud, L. T., & Purcell, C. 2016, MNRAS, 458, 1742
Czekala, I., Loomis, R. A., Teague, R., et al. 2021, ApJS, 257, 2
Endres, C. P., Schlemmer, S., Schilke, P., et al. 2016, J. Mol. Spectrosc., 327, 95
Enoch, M. L., Evans, N. J. I., Sargent, A. I., et al. 2008, ApJ, 684, 1240
Fernández-López, M., Sanhueza, P., Zapata, L. A., et al. 2021, ApJ, 913, 29
Fujiyoshi, T., Smith, C. H., Caswell, J. L., et al. 2006, MNRAS, 368, 1843
Ginsburg, A., & Mirocha, J. 2011, Astrophysics Source Code Library [record ascl:`1109.001`]
Ginsburg, A., Bally, J., Battersby, C., et al. 2015, A&A, 573, A106
Ginsburg, A., Goddi, C., Kruijssen, J. M. D., et al. 2017, ApJ, 842, 92
Ginsburg, A., Koch, E., Robitaille, T., et al. 2019, `https://doi.org/10.5281/zenodo.3558614`
Ginsburg, A., Csengeri, T., Galván-Madrid, R., et al. 2022a, A&A, 662, A9
Ginsburg, A., Sokolov, V., de Val-Borro, M., et al. 2022b, AJ, 163, 291
Hsieh, T. H., Segura-Cox, D. M., Pineda, J. E., et al. 2023, A&A, 669, A137
Immer, K., Galván-Madrid, R., König, C., Liu, H. B., & Menten, K. M. 2014, A&A, 572, A63
Jorsater, S., & van Moorsel, G. A. 1995, AJ, 110, 2037
Kirk, H., Pineda, J. E., Johnstone, D., & Goodman, A. 2010, ApJ, 723, 457
Könyves, V., André, P., Men'shchikov, A., et al. 2015, A&A, 584, A91
Kroupa, P., Weidner, C., Pflamm-Altenburg, J., et al. 2013, in Planets, Stars and Stellar Systems. Volume 5: Galactic Structure and Stellar Populations, eds. T. D. Oswalt, & G. Gilmore, 115
Krumholz, M. R. 2015, in Very Massive Stars in the Local Universe, ed. J. S. Vink, Astrophys. Space Sci. Libr., 412, 43
Larson, R. B. 1981, MNRAS, 194, 809
Lee, Y.-N., Offner, S. S. R., Hennebelle, P., et al. 2020, Space Sci. Rev., 216, 70
Li, S., Sanhueza, P., Lu, X., et al. 2022, ApJ, 939, 102
Louvet, F., Sanhueza, P., Stutz, A., et al. 2023, A&A, submitted
Lu, X., Cheng, Y., Ginsburg, A., et al. 2020, ApJ, 894, L14
Maud, L. T., Lumsden, S. L., Moore, T. J. T., et al. 2015, MNRAS, 452, 637
McMullin, J. P., Waters, B., Schiebel, D., Young, W., & Golap, K. 2007, ASP Conf. Ser., 376, 127
Men'shchikov, A. 2021, A&A, 649, A89
Millar, T. J., Bennett, A., & Herbst, E. 1989, ApJ, 340, 906
Molet, J., Brouillet, N., Nony, T., et al. 2019, A&A, 626, A132
Motte, F., Andre, P., & Neri, R. 1998, A&A, 336, 150
Motte, F., André, P., Ward-Thompson, D., & Bontemps, S. 2001, A&A, 372, L41
Motte, F., Nony, T., Louvet, F., et al. 2018, Nat. Astron., 2, 478
Motte, F., Bontemps, S., Csengeri, T., et al. 2022, A&A, 662, A8
Müller, H. S. P., Thorwirth, S., Roth, D. A., & Winnewisser, G. 2001, A&A, 370, L49
Müller, H. S. P., Schlöder, F., Stutzki, J., & Winnewisser, G. 2005, J. Mol. Struct., 742, 215
Nguyen-Luong, Q., Motte, F., Carlhoff, P., et al. 2013, ApJ, 775, 88
Nony, T., Motte, F., Louvet, F., et al. 2020, A&A, 636, A38
Nony, T., Galván-Madrid, R., Motte, F., et al. 2023, A&A, 674, A75
Offner, S. S. R., Clark, P. C., Hennebelle, P., et al. 2014, Protostars and Planets VI, 53
Ohashi, S., Sanhueza, P., Chen, H.-R. V., et al. 2016, ApJ, 833, 209
Pouteau, Y., Motte, F., Nony, T., et al. 2022, A&A, 664, A26
Pouteau, Y., Motte, F., Nony, T., et al. 2023, A&A, 674, A76
Roberts, H., & Millar, T. J. 2000, A&A, 364, 780
Roueff, E., Parise, B., & Herbst, E. 2007, A&A, 464, 245
Roueff, E., Gerin, M., Lis, D. C., et al. 2013, J. Phys. Chem. A, 117, 9959
Sakai, T., Sanhueza, P., Furuya, K., et al. 2022, ApJ, 925, 144
Sánchez-Monge, Á., Schilke, P., Schmiedeke, A., et al. 2017, A&A, 604, A6
Sanhueza, P., Contreras, Y., Wu, B., et al. 2019, ApJ, 886, 102
Schöier, F. L., van der Tak, F. F. S., van Dishoeck, E. F., & Black, J. H. 2005, A&A, 432, 369
Shirley, Y. L. 2015, PASP, 127, 299
Stutz, A. M., & Gould, A. 2016, A&A, 590, A2
Tan, J. C., Kong, S., Butler, M. J., Caselli, P., & Fontani, F. 2013, ApJ, 779, 96
Tatematsu, K., Liu, T., Kim, G., et al. 2020, ApJ, 895, 119
Testi, L., & Sargent, A. I. 1998, ApJ, 508, L91
Traficante, A., Duarte-Cabral, A., Elia, D., et al. 2018, MNRAS, 477, 2220
Turner, B. E. 2001, ApJS, 136, 579
Walter, F., Brinks, E., de Blok, W. J. G., et al. 2008, AJ, 136, 2563
Wienen, M., Wyrowski, F., Menten, K. M., et al. 2015, A&A, 579, A91
Zhang, Q., Wang, K., Lu, X., & Jiménez-Serra, I. 2015, ApJ, 804, 141

---

[1] Université Grenoble Alpes, CNRS, Institut de Planétologie et d'Astrophysique de Grenoble, 38000 Grenoble, France
e-mail: `nichol.cunningham@univ-grenoble-alpes.fr`
[2] Department of Astronomy, University of Florida, PO Box 112055, Gainesville, USA
[3] Instituto de Radioastronomía y Astrofísica, Universidad Nacional Autónoma de México, Morelia, Michoacán 58089, Mexico

[4] Laboratoire d'astrophysique de Bordeaux, Univ. Bordeaux, CNRS, B18N allée Geoffroy Saint-Hilaire, 33615 Pessac, France
[5] Departamento de Astronomía, Universidad de Concepción, Casilla 160-C, 4030000 Concepción, Chile
[6] Instituto Argentino de Radioastronomí a (CCT-La Plata, CONICET; CICPBA), C.C. No. 5, 1894 Villa Elisa, Buenos Aires, Argentina
[7] Laboratoire de Physique de l'École Normale Supérieure, ENS, Université PSL, CNRS, Sorbonne Université, Université Paris Cité, 75005 Paris, France
[8] Observatoire de Paris, PSL University, Sorbonne Université, LERMA, 75014 Paris, France
[9] S. N. Bose National Centre for Basic Sciences, Block JD, Sector III, Salt Lake, Kolkata 700106, India
[10] Department de Frisca Quantica i Astrofrisca, Universitat de Barcelona (UB), c. Martí i Franquès, 1, 08028 Barcelona, Catalonia, Spain
[11] Instituto de Ciències del Cosmos (ICCUB), Universitat de Barcelona (UB), c. Martí i Franquès, 1, 08028 Barcelona, Catalonia, Spain
[12] Institut d'Estudis Espacials de Catalunya (IEEC), Gran Capita, 2-4, 08340 Barcelona, Catalonia, Spain
[13] Institut de Radioastronomie Millimétrique (IRAM), 300 rue de la Piscine, 38406 Saint-Martin-d'Hères, France
[14] ESO Headquarters, Karl-Schwarzchild-Str 2, 85748 Garching, Germany
[15] Institute of Astronomy, National Tsing Hua University, Hsinchu 30013, Taiwan
[16] National Astronomical Observatory of Japan, National Institutes of Natural Sciences, 2-21-1 Osawa, Mitaka, Tokyo 181-8588, Japan
[17] Astronomical Science Program, Graduate Institute for Advanced Studies, SOKENDAI, 2-21-1 Osawa, Mitaka, Tokyo 181-8588, Japan
[18] Herzberg Astronomy and Astrophysics Research Centre, National Research Council of Canada, 5071 West Saanich Road, Victoria, BC V9E 2E7, Canada
[19] Department of Astronomy, Yunnan University, Kunming 650091, PR China
[20] Shanghai Astronomical Observatory, Chinese Academy of Sciences, 80 Nandan Road, Shanghai 200030, PR China
[21] Department of Astronomy, University of Virginia, Charlottesville, VA 22904, USA
[22] DAS, Universidad de Chile, 1515 camino el observatorio, Las Condes, Santiago, Chile

Appendix A: Properties of the line cubes and overview of spectral setups

In Table A.1 the geometric average of the expected continuum beam from the proposal (θ_{prop}) and the obtained beams (θ_{cont}) are given. In Table A.2, we provide the beam major and minor axes, along with the position angle for all observed protoclusters and spectral windows. In Table A.3, we provide the exact range of the frequency setups for each spectral window towards all 15 protoclusters. In Table A.4, we provide the rms noise extracted for each spectral window (in units of mJy per dirty beam) as well as the noise expected from the proposed observations, scaled to the same spectral resolution and central frequency. In Table A.5, we provide the ϵ factors used in the JvM correction for each spectral window.

Table A.1. Proposed and actual continuum beams for all spectral windows.

Protocluster cloud name	θ_{prop} [$''$]	B3 θ_{cont} [$''$]	B6 θ_{cont} [$''$]
G008.67	0.67	0.52	0.66
G010.62	0.37	0.36	0.47
G012.80	0.95	1.3	0.88
G327.29	0.67	0.4	0.66
G328.25	0.67	0.51	0.54
G337.92	0.51	0.37	0.54
G338.93	0.51	0.42	0.53
G333.60	0.51	0.46	0.55
G351.77	0.95	1.4	0.77
G353.41	0.95	1.2	0.79
W43-MM1	0.37	0.41	0.43
W43-MM2	0.37	0.27	0.46
W43-MM3	0.37	0.35	0.49
W51-E	0.37	0.27	0.3
W51-IRS2	0.37	0.28	0.47

Table A.2. Obtained beams for B3 spectral windows (0-3).

Protocluster cloud name	spw0			spw1			spw2			spw3		
	θ_{maj} ($''$)	θ_{min} ($''$)	PA	θ_{maj} ($''$)	θ_{min} ($''$)	PA	θ_{maj} ($''$)	θ_{min} ($''$)	PA	θ_{maj} ($''$)	θ_{min} ($''$)	PA
G008.67	0.95	0.72	72	0.55	0.43	69	0.50	0.40	65	0.49	0.38	61
G010.62	0.53	0.39	102	0.46	0.38	107	0.37	0.28	94	0.37	0.29	107
G012.80	2.23	1.83	88	1.85	1.65	80	1.73	1.52	84	1.70	1.43	87
G327.29	0.66	0.57	53	0.45	0.39	69	0.41	0.35	69	0.41	0.35	68
G328.25	0.97	0.90	71	0.69	0.51	106	0.63	0.48	113	0.61	0.45	112
G337.92	0.67	0.60	-72	0.49	0.42	73	0.44	0.39	73	0.43	0.36	75
G338.93	0.59	0.54	-62	0.45	0.42	40	0.39	0.35	88	0.38	0.35	84
G333.60	0.73	0.70	13	0.50	0.47	45	0.45	0.44	25	0.45	0.42	37
G351.77	2.20	1.88	91	1.85	1.65	88	1.69	1.51	89	1.72	1.49	100
G353.41	2.12	1.76	77	1.83	1.54	69	1.67	1.50	76	1.62	1.47	78
W43-MM1	0.88	0.48	99	0.59	0.37	107	0.54	0.33	107	0.53	0.33	108
W43-MM2	0.41	0.32	106	0.34	0.26	106	0.30	0.24	110	0.32	0.24	124
W43-MM3	0.58	0.42	97	0.47	0.33	99	0.42	0.29	98	0.41	0.29	99
W51-E	0.38	0.35	106	0.36	0.33	108	0.29	0.27	83	0.28	0.26	85
W51-IRS2	0.39	0.36	111	0.33	0.30	131	0.29	0.27	130	0.28	0.27	128

Table A.2. continued: Obtained beams for B6 spectral windows (0-3).

Protocluster cloud name	spw0			spw1			spw2			spw3		
	θ_{maj} ($''$)	θ_{min} ($''$)	PA	θ_{maj} ($''$)	θ_{min} ($''$)	PA	θ_{maj} ($''$)	θ_{min} ($''$)	PA	θ_{maj} ($''$)	θ_{min} ($''$)	PA
G008.67	0.88	0.72	98	0.88	0.72	98	0.88	0.72	96	0.88	0.71	99
G010.62	0.65	0.51	106	0.68	0.53	-72	0.64	0.50	106	0.66	0.52	-76
G012.80	1.30	0.89	76	1.29	0.88	76	1.29	0.86	76	1.29	0.87	77
G327.29	0.82	0.76	121	0.82	0.75	124	0.82	0.74	123	0.82	0.74	125
G328.25	0.74	0.59	-13	0.74	0.58	-14	0.75	0.59	-14	0.74	0.58	-14
G337.92	0.81	0.66	129	0.80	0.66	129	0.79	0.66	128	0.80	0.66	129
G338.93	0.77	0.69	80	0.77	0.68	81	0.74	0.65	81	0.75	0.65	83
G333.60	0.75	0.69	-35	0.75	0.68	-36	0.74	0.68	-37	0.74	0.68	-38
G351.77	1.08	0.84	88	1.08	0.83	87	1.07	0.82	88	1.08	0.82	88
G353.41	1.13	0.83	86	1.13	0.83	85	1.11	0.83	86	1.12	0.83	86
W43-MM1	0.66	0.48	-81	0.65	0.47	100	0.67	0.49	103	0.65	0.49	105
W43-MM2	0.63	0.52	100	0.62	0.51	-84	0.68	0.54	100	0.64	0.50	96
W43-MM3	0.66	0.57	86	0.66	0.57	86	0.66	0.57	86	0.66	0.57	86
W51-E	0.46	0.35	29	0.46	0.35	30	0.57	0.49	38	0.46	0.35	30
W51-IRS2	0.64	0.57	-18	0.65	0.59	-23	0.65	0.58	-21	0.63	0.56	-24

Table A.2. continued: Obtained beams for B6 spectral windows (4-7).

Protocluster cloud name	spw4			spw5			spw6			spw7		
	θ_{maj} ($''$)	θ_{min} ($''$)	PA	θ_{maj} ($''$)	θ_{min} ($''$)	PA	θ_{maj} ($''$)	θ_{min} ($''$)	PA	θ_{maj} ($''$)	θ_{min} ($''$)	PA
G008.67	0.88	0.71	99	0.84	0.68	96	0.83	0.67	96	0.73	0.61	97
G010.62	0.67	0.52	112	0.61	0.48	-73	0.61	0.47	106	0.58	0.43	110
G012.80	1.29	0.87	77	1.21	0.83	76	1.21	0.82	76	1.13	0.72	76
G327.29	0.82	0.74	125	0.77	0.70	128	0.77	0.69	127	0.69	0.62	-35
G328.25	0.74	0.58	-14	0.69	0.54	-13	0.69	0.54	-13	0.61	0.45	-13
G337.92	0.80	0.66	129	0.75	0.61	127	0.74	0.61	127	0.65	0.51	127
G338.93	0.75	0.66	82	0.71	0.63	84	0.71	0.63	83	0.60	0.55	91
G333.60	0.74	0.68	-36	0.69	0.62	-34	0.68	0.62	-34	0.57	0.52	-23
G351.77	1.07	0.82	88	1.01	0.77	88	1.00	0.77	87	0.91	0.68	87
G353.41	1.12	0.82	84	1.06	0.77	84	1.05	0.76	86	0.96	0.67	85
W43-MM1	0.69	0.50	99	0.59	0.43	100	0.59	0.43	100	0.50	0.34	103
W43-MM2	0.68	0.53	96	0.61	0.51	110	0.61	0.51	110	0.56	0.45	112
W43-MM3	0.66	0.57	85	0.62	0.54	86	0.62	0.53	85	0.55	0.46	88
W51-E	0.57	0.47	39	0.52	0.41	34	0.42	0.32	30	0.34	0.27	25
W51-IRS2	0.63	0.56	-23	0.59	0.52	-23	0.59	0.52	-25	0.54	0.47	-26

Table A.3. Minimum and maximum frequency ranges [GHz] for the spectral window setups for B3 spws (0-3).

Protocluster cloud name[1]	spw0		spw1		spw2		spw3	
	min	max	min	max	min	max	min	max
G008.67	93.103	93.220	91.720	92.656	102.119	103.056	104.519	105.455
G010.62	93.116	93.233	91.733	92.669	102.133	103.069	104.533	105.469
G012.80	93.103	93.220	91.720	92.657	102.119	103.056	104.519	105.455
G327.29	93.129	93.246	91.746	92.682	102.147	103.084	104.547	105.484
G328.25	93.128	93.245	91.745	92.682	102.147	103.083	104.547	105.483
G337.92	93.127	93.244	91.744	92.681	102.146	103.082	104.546	105.482
G338.93	93.134	93.251	91.751	92.688	102.153	103.089	104.554	105.490
G333.60	93.130	93.247	91.746	92.683	102.148	103.085	104.548	105.485
G351.77	93.116	93.233	91.733	92.669	102.133	103.069	104.533	105.469
G353.41	93.120	93.237	91.737	92.674	102.138	103.074	104.538	105.474
W43-MM1	93.085	93.202	91.702	92.639	102.099	103.035	104.498	105.434
W43-MM2	93.085	93.202	91.702	92.638	102.099	103.035	104.498	105.435
W43-MM3	93.085	93.202	91.702	92.639	102.099	103.035	104.498	105.434
W51-E	93.098	93.215	91.715	92.651	102.113	103.049	104.513	105.449
W51-IRS2	93.098	93.215	91.715	92.651	102.113	103.050	104.513	105.449

Table A.3. continued: Minimum and maximum frequency ranges [GHz] for the spectral window setups for B6 spws (0-3).

Protocluster	spw0		spw1		spw2		spw3	
cloud name[1]	min	max	min	max	min	max	min	max
G008.67	216.056	216.290	217.006	217.240	219.859	219.976	218.086	218.320
G010.62	216.084	216.318	217.034	217.268	219.888	220.005	218.114	218.348
G012.80	216.056	216.290	217.006	217.240	219.860	219.976	218.086	218.320
G327.29	216.115	216.350	217.066	217.299	219.920	220.036	218.146	218.380
G328.25	216.114	216.348	217.064	217.298	219.918	220.035	218.144	218.378
G337.92	216.112	216.346	217.062	217.296	219.916	220.033	218.142	218.376
G338.93	216.128	216.362	217.078	217.312	219.932	220.049	218.158	218.392
G333.60	216.117	216.351	217.067	217.301	219.921	220.038	218.147	218.381
G351.77	216.085	216.319	217.035	217.269	219.889	220.006	218.115	218.349
G353.41	216.095	216.329	217.045	217.279	219.899	220.016	218.125	218.360
W43-MM1	216.014	216.249	216.964	217.198	219.817	219.934	218.044	218.278
W43-MM2	216.013	216.247	216.963	217.197	219.816	219.932	218.042	218.276
W43-MM3	216.013	216.247	216.963	217.197	219.816	219.932	218.042	218.277
W51-E	216.043	216.277	216.993	217.227	219.846	219.963	218.073	218.307
W51-IRS2	216.043	216.277	216.993	217.227	219.846	219.963	218.073	218.307

Table A.3. continued: Minimum and maximum frequency ranges [GHz] for the spectral window setups for B6 spws (4-7).

Protocluster	spw4		spw5		spw6		spw7	
cloud name[1]	min	max	min	max	min	max	min	max
G008.67	219.474	219.591	230.268	230.735	231.017	231.485	231.480	233.353
G010.62	219.503	219.620	230.298	230.765	231.047	231.516	231.508	233.381
G012.80	219.474	219.591	230.269	230.735	231.017	231.486	231.480	233.353
G327.29	219.534	219.651	230.331	230.798	231.081	231.549	231.541	233.414
G328.25	219.533	219.650	230.330	230.797	231.079	231.547	231.540	233.413
G337.92	219.531	219.648	230.328	230.794	231.077	231.545	231.538	233.361
G338.93	219.547	219.664	230.345	230.811	231.094	231.562	231.554	233.426
G333.60	219.536	219.653	230.333	230.800	231.082	231.550	231.543	233.415
G351.77	219.504	219.621	230.299	230.766	231.048	231.517	231.510	233.383
G353.41	219.514	219.631	230.310	230.777	231.059	231.527	231.521	233.393
W43-MM1	219.432	219.549	230.224	230.690	230.973	231.441	232.490	234.362
W43-MM2	219.431	219.548	230.222	230.689	230.971	231.439	231.436	233.308
W43-MM3	219.431	219.547	230.222	230.688	230.971	231.439	231.435	233.308
W51-E	219.461	219.578	230.255	230.721	231.004	231.472	231.467	233.339
W51-IRS2	219.461	219.578	230.255	230.721	231.003	231.472	231.467	233.339

Table A.4. Spectral window noise estimates for B3 spws (0-3).

Protocluster cloud name[1]	spw0			spw1			spw2			spw3		
	σ_{MAD}	σ_{req}	$\frac{\sigma_{MAD}}{\sigma_{req}}$	σ_{MAD}	σ_{req}	$\frac{\sigma_{MAD}}{\sigma_{req}}$	σ_{MAD}	σ_{req}	$\frac{\sigma_{MAD}}{\sigma_{req}}$	σ_{MAD}	σ_{req}	$\frac{\sigma_{MAD}}{\sigma_{req}}$
	[mJybeam^{-1}]			[mJybeam^{-1}]			[mJybeam^{-1}]			[mJybeam^{-1}]		
G008.67	7.39	14.84	0.50	2.78	5.47	0.50	3.28	7.25	0.55	3.59	7.59	0.60
G010.62	3.52	5.04	0.70	1.51	1.86	0.79	1.53	2.46	0.75	1.32	2.58	0.65
G012.80	11.18	28.36	0.39	3.95	10.46	0.37	4.82	13.85	0.42	5.10	14.50	0.45
G327.29	6.23	14.92	0.42	1.26	5.50	0.22	2.86	7.29	0.48	2.88	7.63	0.48
G328.25	8.16	14.83	0.55	5.38	5.47	0.96	3.52	7.24	0.59	3.76	7.58	0.63
G337.92	3.63	9.93	0.37	2.25	3.66	0.60	2.52	4.85	0.63	1.60	5.08	0.40
G338.93	4.67	9.89	0.47	2.15	3.64	0.58	2.47	4.83	0.62	2.66	5.05	0.67
G333.60	4.97	9.84	0.50	1.84	3.63	0.50	2.02	4.80	0.51	2.25	5.03	0.57
G351.77	10.84	28.50	0.38	3.78	10.52	0.35	4.39	13.92	0.38	5.69	14.58	0.50
G353.41	10.75	28.46	0.38	3.91	10.50	0.36	4.45	13.90	0.39	4.95	14.55	0.43
W43-MM1	2.60	4.99	0.52	0.88	1.84	0.47	1.07	2.44	0.53	0.96	2.55	0.48
W43-MM2	2.68	4.99	0.54	1.09	1.84	0.58	1.26	2.44	0.63	1.38	2.55	0.69
W43-MM3	3.14	4.99	0.63	1.15	1.84	0.61	1.29	2.44	0.64	1.42	2.55	0.71
W51-E	2.23	4.95	0.45	0.92	1.83	0.49	1.06	2.41	0.53	1.16	2.53	0.58
W51-IRS2	2.58	4.95	0.52	0.93	1.83	0.50	1.24	2.41	0.62	1.29	2.53	0.65

σ_{MAD} is given in units of mJy per dirty beam as discussed in Section 3.3, while σ_{req} is the noise expected from the proposed ALMA observations.

Table A.4. Spectral window noise estimates for B6 spws (0-3).

Protocluster cloud name[1]	spw0			spw1			spw2			spw3		
	σ_{MAD}	σ_{req}	$\frac{\sigma_{MAD}}{\sigma_{req}}$	σ_{MAD}	σ_{req}	$\frac{\sigma_{MAD}}{\sigma_{req}}$	σ_{MAD}	σ_{req}	$\frac{\sigma_{MAD}}{\sigma_{req}}$	σ_{MAD}	σ_{req}	$\frac{\sigma_{MAD}}{\sigma_{req}}$
	[mJybeam^{-1}]			[mJybeam^{-1}]			[mJybeam^{-1}]			[mJybeam^{-1}]		
G008.67	12.23	29.65	0.36	10.80	19.75	0.48	14.87	20.39	0.66	11.25	30.21	0.33
G010.62	3.88	10.22	0.33	3.25	6.81	0.42	4.35	7.03	0.56	3.62	10.41	0.31
G012.80	14.75	46.99	0.27	13.37	31.29	0.38	19.28	32.31	0.54	13.78	47.87	0.26
G327.29	13.95	32.34	0.38	12.20	21.54	0.50	14.75	22.24	0.60	12.04	32.95	0.33
G328.25	25.35	32.32	0.69	22.47	21.54	0.92	30.00	22.23	1.22	23.69	32.93	0.64
G337.92	6.52	19.90	0.29	5.08	13.26	0.34	7.47	13.68	0.49	5.75	20.27	0.25
G338.93	6.30	19.30	0.29	5.49	12.86	0.38	7.74	13.28	0.53	6.05	19.67	0.27
G333.60	5.87	19.96	0.26	8.27	13.29	0.55	6.91	13.73	0.46	5.42	20.34	0.24
G351.77	16.63	49.16	0.30	14.38	32.75	0.39	20.08	33.81	0.54	15.80	50.04	0.28
G353.41	17.82	49.59	0.31	16.01	33.03	0.43	22.12	34.10	0.59	15.90	50.53	0.28
W43-MM1	3.64	10.29	0.31	3.26	6.85	0.42	4.86	7.07	0.62	3.32	10.48	0.28
W43-MM2	3.01	10.29	0.26	2.65	6.85	0.34	3.85	7.07	0.49	2.89	10.48	0.25
W43-MM3	3.54	10.29	0.30	3.16	6.85	0.41	4.20	7.07	0.54	3.19	10.48	0.27
W51-E	4.36	10.49	0.36	3.83	7.02	0.48	4.90	7.24	0.61	4.15	10.73	0.34
W51-IRS2	3.52	10.53	0.29	3.19	7.02	0.40	4.35	7.24	0.54	3.25	10.73	0.27

σ_{MAD} is given in units of mJy per dirty beam as discussed in Section 3.3, while σ_{req} is the noise expected from the proposed ALMA observations.

Table A.4. Spectral window noise estimates for B6 spws (4-7).

Protocluster cloud name[1]	spw4			spw5			spw6			spw7		
	σ_{MAD}	σ_{req}	$\frac{\sigma_{MAD}}{\sigma_{req}}$	σ_{MAD}	σ_{req}	$\frac{\sigma_{MAD}}{\sigma_{req}}$	σ_{MAD}	σ_{req}	$\frac{\sigma_{MAD}}{\sigma_{req}}$	σ_{MAD}	σ_{req}	$\frac{\sigma_{MAD}}{\sigma_{req}}$
	[mJybeam^{-1}]			[mJybeam^{-1}]			[mJybeam^{-1}]			[mJybeam^{-1}]		
G008.67	15.89	30.58	0.47	7.67	12.38	0.62	10.09	24.73	0.41	6.43	11.71	0.56
G010.62	5.15	10.54	0.44	2.61	4.26	0.61	3.21	8.52	0.38	1.75	4.03	0.44
G012.80	21.63	48.46	0.40	10.76	19.61	0.55	11.90	39.19	0.30	7.01	18.56	0.38
G327.29	16.42	33.35	0.44	8.14	13.50	0.60	10.45	26.98	0.39	6.41	12.78	0.51
G328.25	32.64	33.34	0.88	16.99	13.49	1.25	22.07	26.97	0.82	22.71	12.77	1.80
G337.92	8.48	20.52	0.37	3.67	8.31	0.44	5.05	16.60	0.30	2.80	7.86	0.36
G338.93	8.45	19.91	0.38	3.38	8.06	0.42	5.11	16.10	0.32	2.74	7.63	0.36
G333.60	7.50	20.58	0.33	3.04	8.34	0.36	4.57	16.65	0.27	2.45	7.89	0.31
G351.77	20.76	50.70	0.37	12.15	20.53	0.59	13.36	41.01	0.33	8.49	19.43	0.44
G353.41	22.05	51.10	0.39	12.74	20.71	0.61	13.58	41.37	0.33	8.77	19.59	0.45
W43-MM1	4.69	10.61	0.40	2.43	4.29	0.56	3.05	8.58	0.35	2.09	4.06	0.52
W43-MM2	4.25	10.61	0.36	1.58	4.29	0.37	2.56	8.58	0.30	1.63	4.06	0.40
W43-MM3	4.64	10.61	0.39	2.27	4.29	0.53	2.77	8.58	0.32	1.62	4.06	0.40
W51-E	4.71	10.86	0.39	2.78	4.40	0.63	3.57	8.79	0.41	2.45	4.16	0.59
W51-IRS2	4.41	10.86	0.37	2.05	4.40	0.46	2.90	8.79	0.33	1.55	4.16	0.38

σ_{MAD} is given in units of mJy per dirty beam as discussed in Section 3.3, while σ_{req} is the noise expected from the proposed ALMA observations.

Table A.5. ϵ values used for the JvM correction for B3 spws (0-3) and B6 spws (0-7).

Protocluster	B3				B6							
cloud name	spw0	spw1	spw2	spw3	spw0	spw1	spw2	spw3	spw4	spw5	spw6	spw7
G008.67	0.37	0.49	0.47	0.47	0.67	0.67	0.67	0.67	0.66	0.67	0.67	0.64
G010.62	0.32	0.47	0.94	0.46	0.61	0.61	0.61	0.61	0.61	0.6	0.6	0.87
G012.80	0.66	0.56	0.58	0.59	0.84	0.84	0.85	0.84	0.84	0.84	0.84	0.81
G327.29	0.23	0.88	0.38	0.93	0.7	0.7	0.69	0.7	0.7	0.68	0.69	0.67
G328.25	0.32	0.33	0.52	0.52	0.6	0.6	0.59	0.6	0.6	0.6	0.6	0.61
G337.92	0.4	0.31	0.32	0.48	0.59	0.59	0.58	0.59	0.59	0.58	0.58	0.52
G338.93	0.31	0.38	0.25	0.25	0.58	0.58	0.58	0.57	0.58	0.58	0.57	0.5
G333.60	0.31	0.48	0.5	0.46	0.54	0.54	0.54	0.54	0.54	0.52	0.52	0.49
G351.77	0.67	0.58	0.58	0.6	0.79	0.81	0.79	0.74	0.79	0.74	0.76	0.7
G353.41	0.67	0.56	0.6	0.58	0.78	0.79	0.74	0.79	0.75	0.76	0.79	0.71
W43-MM1	0.47	0.95	0.37	0.4	0.6	0.6	0.62	0.62	0.62	0.61	0.61	0.61
W43-MM2	0.26	0.94	0.97	0.95	0.65	0.62	0.66	0.65	0.65	0.64	0.64	0.65
W43-MM3	0.32	0.85	1.0	1.0	0.59	0.59	0.59	0.58	0.58	0.58	0.57	0.58
W51-E	0.42	0.26	0.99	0.98	0.48	0.48	0.43	0.48	0.47	0.4	0.47	0.48
W51-IRS2	0.41	0.96	0.99	0.98	0.65	0.65	0.65	0.65	0.65	0.65	0.65	0.98

Appendix B: Known data issues

Towards several regions that contain bright hot cores, there can be a slight overestimation of the continuum startmodel at the positions of the hot cores, resulting in localised negative features in some of the residuals. This overestimate is likely due to rich line emission (line forests) across the spectrum at those positions. Often the negative residuals are $< 10\%$ of the flux in the restored image, but in some cases with faint (real) continuum and bright line emission, they are larger. We also note that in some instances the sidelobes can remain particularly bright in the final imaged cubes (e.g. G327 in B6).

Appendix C: Special cases

Several regions required additional special attention in early 2022 because `tclean` failed for a variety of reasons related to software configurations. We were never able to fully determine what the underlying causes of the failures were, but they manifested as `CASA` like the following:

```
MPICommandServer:: command_request_handler
_service:: SynthesisImagerVi2::
CubeMajorCycle::MPIServer-23 (file
src/code/synthesis/ImagerObjects/
CubeMajorCycleAlgorithm.cc, line 336)
Exception for chan range [1921, 1921] -
Error in running Major Cycle: A nasty
Visbuffer2 error occurred...wait for CNGI
W51-E_B3_fullcube_12M_0_34232805.log: Exception:
Error in running Major Cycle: A nasty Visbuffer2
error occurred...wait for CNGI
```

or

```
SEVERE tclean::::casa Task tclean raised an
exception of class RuntimeError with the
following message: Error in making PSF : One or
more of the cube section failed in de/gridding.
Return values for the sections: [1, 1, 1, 1, 1,
1, 1, 0, 0, 1, 1, 1, 1, 1, 1, 1, 1, 1, 1, 1, 1,
1, 1, 1, 1, 1, 1, 1, 1, 1, 1, 1, 1, 1, 1, 1, 1,
1, 1, 1, 1, 1, 1, 1, 1, 1, 1, 1, 1, 1, 1, 1, 1,
1, 1, 1, 1, 1, 1, 1, 1, 1, 1, 1, 1, 1, 1, 1, 1,
1, 1, 1, 1, 1, 1, 1, 1, 1, 1, 1, 1, 1, 1, 1, 1,
1, 1, 1, 1, 1, 1, 1, 1, 0, 1, 1, 1, 1, 1, 1, 1,
1, 1, 1, 1, 1, 1, 1, 1, 1, 1, 1, 1, 1, 1, 1, 1,
1, 1, 1, 1, 1, 1, 1]
```

Two combinations of field and band, W51-E B3 spw0 and G333.60 B6 spw 1, proved particularly difficult to run `tclean` to completion. We, therefore, modified the W51-E B3 spw0 imaging parameters to specify the number of channels by hand. For G333.60, we found that the final model exhibited 'zigzag' spectral patterns, in which, at the end of cleaning, adjacent spectral channels oscillated from $-1t$ to $+1t$, where t is the final clean threshold. These oscillations manifest strongly in the image and spectra and render the data unusable for science, even though technically the clean threshold has been met. To correct this issue, we re-processed the final `.model` file by applying a 3-pixel maximum spectral filter, that is, replacing the value at each pixel in the cube with the maximum of the ±1 pixel range surrounding it in the spectral dimension. This approach has the effect of retaining the spectral peaks, but slightly over-predicting the values to either edge of the peaks.

Appendix D: DCN moment maps

In Figure D.1 we present the first three moment maps for the remaining 13 protoclusters. G338.93 and G333.60 are presented in the main body of the text in Figure 8.

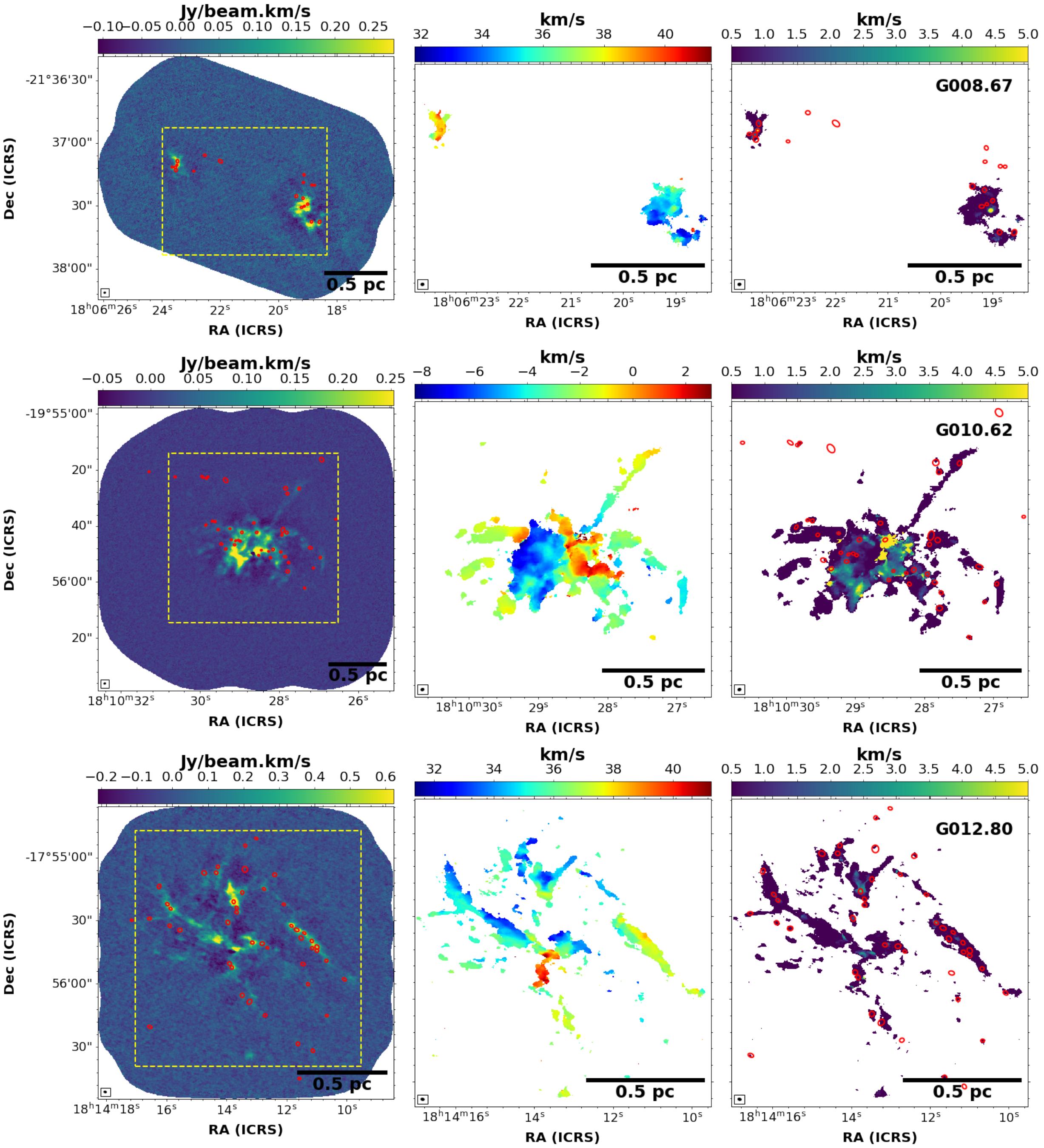

Fig. D.1. Moment maps (moment 0, 1, and 2 in the left, centre, and right panels, respectively) of DCN (3-2) emission towards the protoclusters G008.67 (top), G010.62 (middle), and G012.80 (bottom). All three moments have been determined over a velocity range of 31.7 to 43 km s^{-1}, −9.3 to 5.8 km s^{-1}, and 30.7 to 43 km s^{-1} for G008.67, G010.62, and G012.80, respectively. For the moment 0 and moment 2 maps, we overlay the core positions and sizes (red ellipses) from the continuum core catalogue described in Louvet et al. (2023). For the moment 1 and moment 2 maps, we show a zoom-in of the area highlighted by the yellow dashed box overlaid on the moment 0 map. The moment 1 and moment 2 maps have an additional threshold cut per channel of 4 σ. The synthesised beam is shown in the bottom left corner of each image.

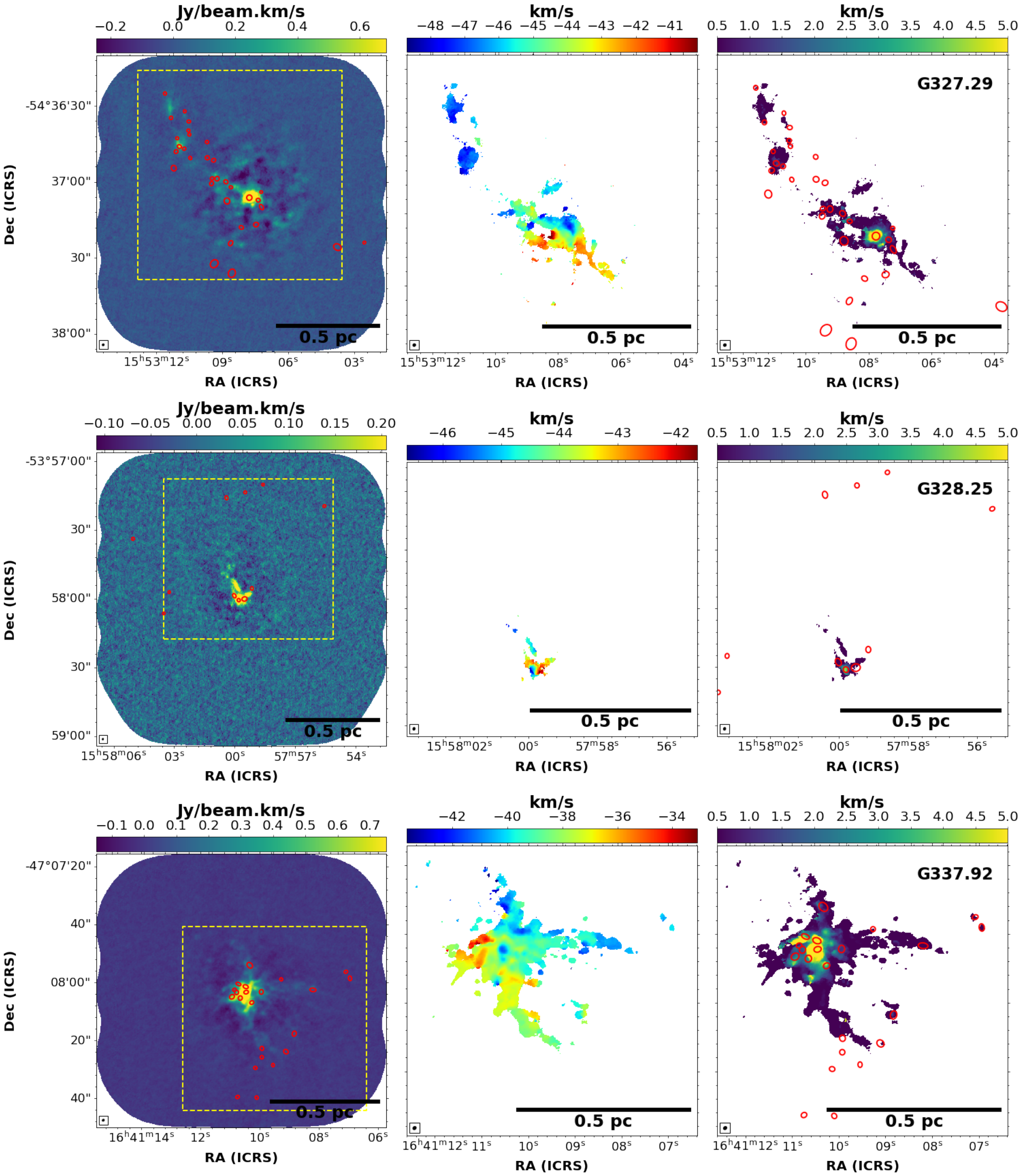

Fig. D.1. continued. Moment maps (Moment 0, 1, and 2 in the left, centre, and right panels, respectively) of DCN (3-2) for G327.29 (top), G328.25 (middle), and G337.92 (bottom). Maps were calculated over a velocity range of −50.2 to −39.7 km s^{-1}, −47.5 to −41 km s^{-1}, and −30.8 to −45 km s^{-1}, respectively.

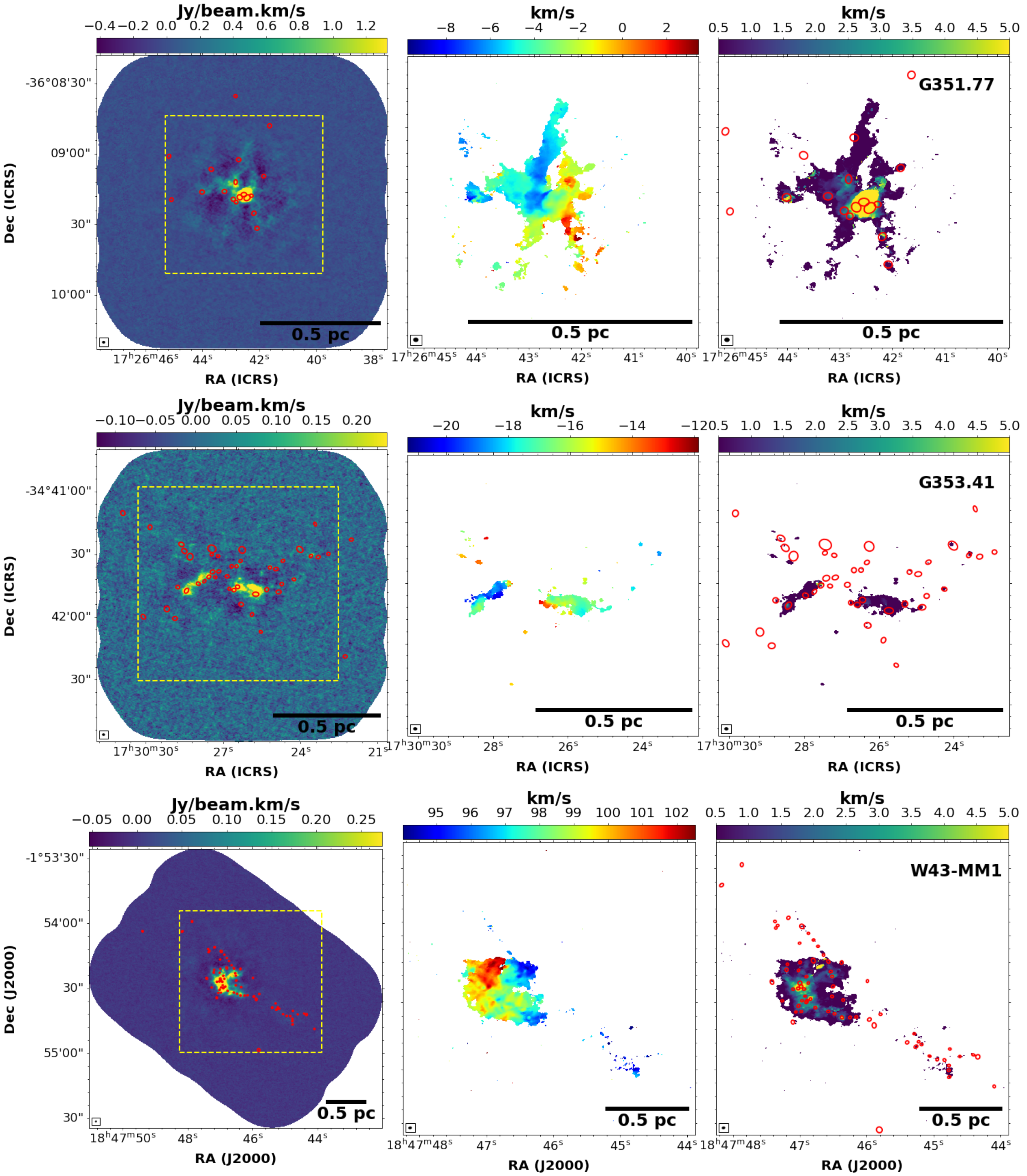

Fig. D.1. continued. Moment maps (Moment 0, 1, and 2 in the left, centre, and right panels, respectively) of DCN (3-2) for G351.77 (top), G353.41 (middle), and W43-MM1 (bottom). Maps were calculated over a velocity range of −9.8 to 3.2 km s^{-1}, −20.5 to −12.7 km s^{-1}, and 92.7 to 105 km s^{-1}, respectively.

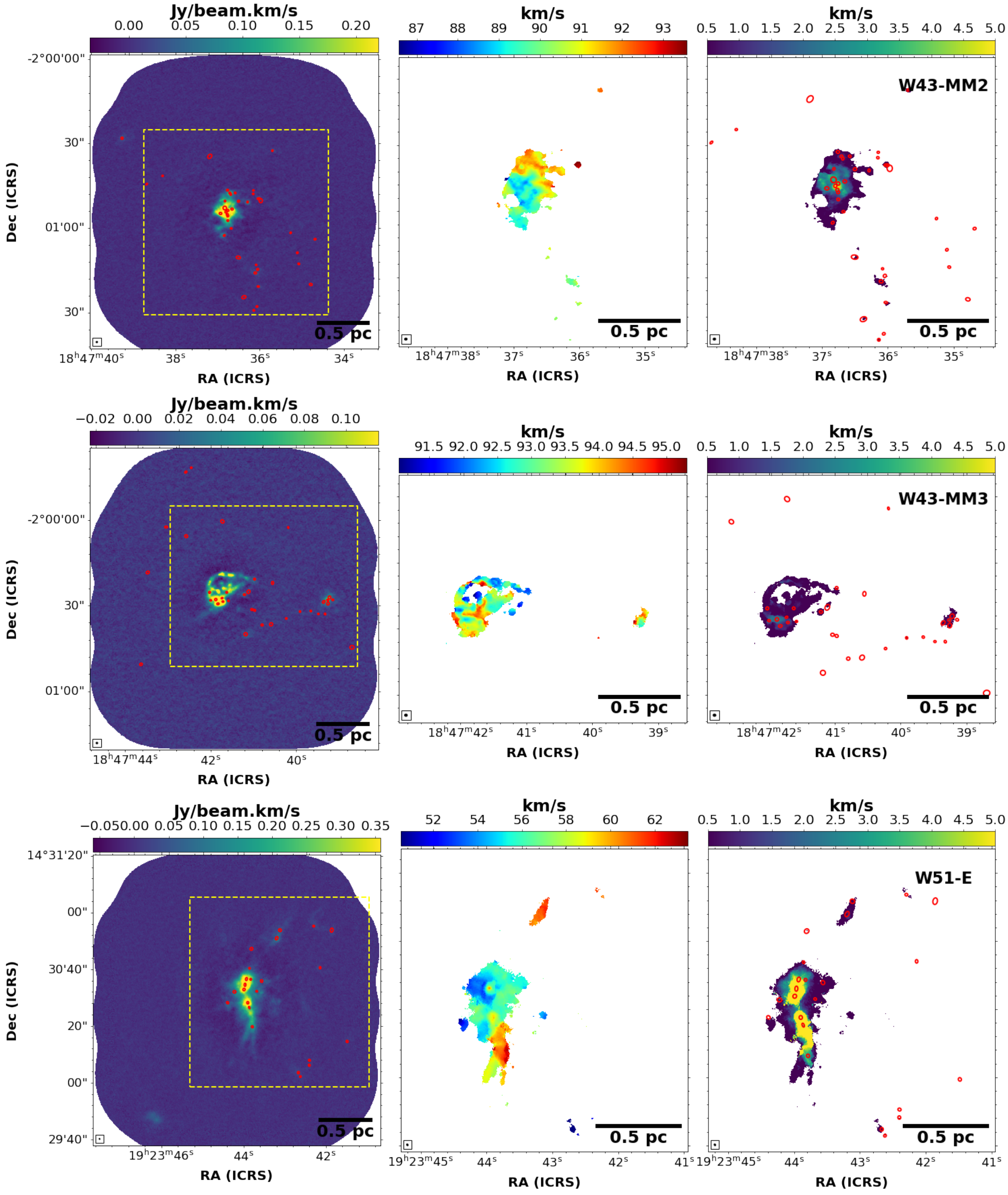

Fig. D.1. continued. Moment maps (Moment 0, 1, and 2 in the left, centre, and right panels, respectively) of DCN (3-2) for W43-MM2 (top), W43-MM3 (middle), and W51-E (bottom). Maps were calculated over a velocity range of 85.7 to 94 km s^{-1}, 90.4 to 95.8 km s^{-1}, and 46 to 64 km s^{-1}, respectively.

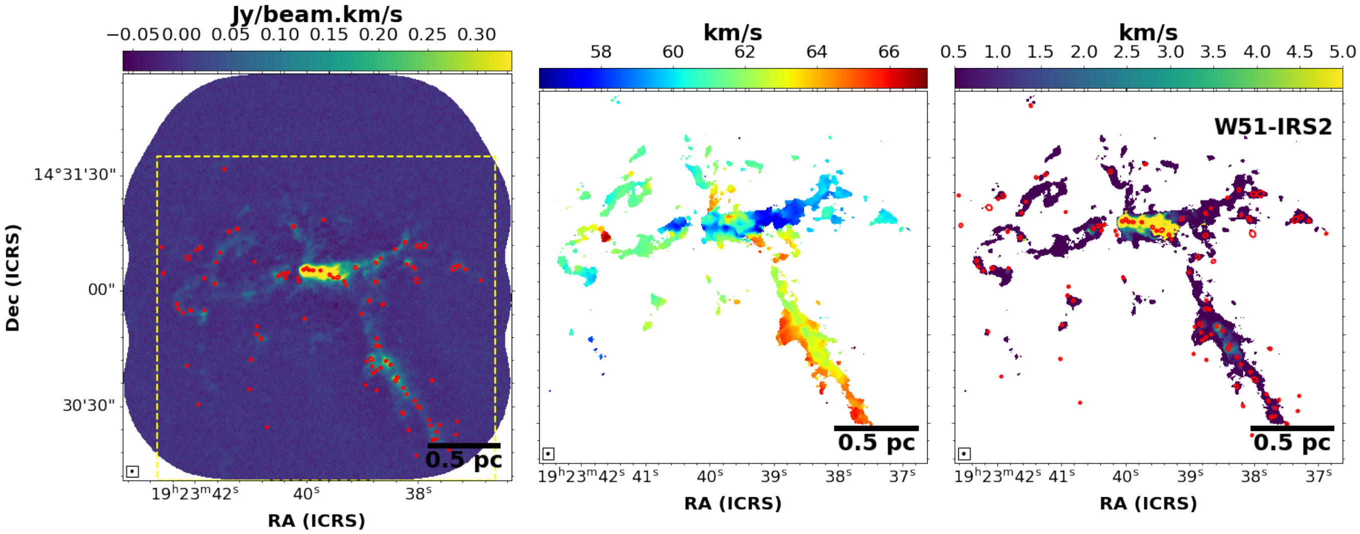

Fig. D.1. continued. Moment maps (Moment 0, 1, and 2 in the left, centre and right panels, respectively) of DCN (3-2) for W51-IRS2. Maps were calculated over a velocity range of 52.4 to 68 km s^{-1}.

Appendix E: DCN line extraction, background subtraction, and hyperfine fitting

We used `spectral-cube`[16] (Ginsburg et al. 2019) to extract the DCN (3-2) emission from the Band 6 spectral window 1 cube. First, we shifted the cubes into the frequency rest frame of the DCN (3-2) transition, and then for each protocluster, we extracted a subcube with a 50 km s^{-1} width centred on the $V_{\rm LSR}$ of the protocluster. We then extracted a core-averaged, background-subtracted DCN (3-2) spectrum for each continuum core. We used the smoothed core catalogue from Louvet et al. (2023) to obtain the positions and core sizes for the 595 continuum cores over the 15 ALMA-IMF protoclusters. We extracted the core-averaged DCN (3-2) spectrum from all pixels within an elliptical aperture with a major (minor) axis length twice that of the continuum source major (minor) FWHM. We subtracted from this an average background spectrum taken from within an elliptical annulus with an inner major (minor) axis size equal to the size of the spectral aperture (i.e. twice the continuum source major (minor) FWHM) and outer radius size 1.5x larger (i.e. three times the continuum source major (minor) FWHM). As nearby cores can overlap with the background annulus, we excluded those pixels from neighbouring cores that spatially overlap with the background annulus, creating a background ‘crown’. An example of the core and background annulus-crown definition can be seen in Fig. E.1. The resulting core-averaged, background-subtracted spectrum for each core was then fitted using `PySpecKit` (Ginsburg & Mirocha 2011; Ginsburg et al. 2022b) with an adapted single component hyperfine model (HFS), to account for the hyperfine structure in the DCN (3-2) line. The values for the specified hyperfine model were taken from the CDMS catalogue to define the frequencies and relative weights of the hyperfine lines (Endres et al. 2016; Müller et al. 2001, 2005). They are presented in Table E.2. An example of the positions of the hyperfine components overlaid on an example DCN spectrum is presented in Fig. E.2.

E.1. Single- and complex-type spectral classification

To classify a spectrum as either detection or non-detection, we require an S/N of at least 4 σ between its peak and estimated noise and a velocity dispersion of > 0.2 km s^{-1}. The noise in the spectrum is estimated from the MAD[10] in 30 continuous channels (~10 km s^{-1}) from either the lower or upper part of the spectrum (shaded pink regions in the DCN spectra) that were identified by eye to be in a line free part of the spectrum. We then split the detected spectra into single- or complex-type. This is done manually by visually inspecting the DCN (3-2) spectra after fitting. Again, we use the higher noise estimates in units of mJy per dirty beam. If multiple components are present in the spectrum, we also classify them as complex-type and remove them from the analysis. The extracted single- and complex-type DCN spectra for each core in each protocluster are shown in Appendix F.

E.2. Comparison of the background and non-background subtracted DCN spectra

In Figures F.11, and E.3, we show the DCN (3-2) detected single- and complex-type spectra identified when performing background-subtraction, and non-background subtraction, respectively, for G338.93. In Figure E.4, for reference, we also show the background spectra. Some of the ’absorption features’ in the background-subtracted spectra result from the background subtraction (e.g. core 13 and 29). The background subtraction also results in some cores with initially complex-type spectra due to the background contamination becoming single-type spectra (e.g. core 16). The background and non-background subtraction detection rates are similar in G338.93, with 18 and 21 detected single-type cores, respectively (with slight differences between which cores are single-type in the two sets), and eight cores with complex-type spectra in both. Furthermore, the average $V_{\rm LSR}$ extracted from all cores is the same (-61 km s^{-1}) when considering either background- or non-background-subtraction. The average linewidth of the fits, however, is smaller (~1.6 km s^{-1}) for the background-subtracted compared with (~2.1 km s^{-1}) for the non-background subtracted, which is due to the removal of the background contribution. These background-subtracted spectra are likely more representative of the gas associated with the cores. In Table E.1, we show the same table as in Table 4 but from fitting the non-background subtracted spectra for all cores in each protocluster. This highlights that the general trends across the sample are the same regardless of whether the background or non-background spectra are used.

---

[16] https://spectral-cube.readthedocs.io/en/latest/

Table E.1. Characteristic parameters of the DCN (3-2) hyperfine fits for the non-background subtracted.

Protocluster cloud name	Number[1] of Cores	Number[2] detected (complex)	Detection[2] rate [%] (complex)	Velocity[3] range [km $\mathrm{s^{-1}}$]	V_{LSR}[3] mean [km $\mathrm{s^{-1}}$]	V_{LSR}[3] std [km $\mathrm{s^{-1}}$]	Linewidth[3] mean [km $\mathrm{s^{-1}}$]	Linewidth[3] median [km $\mathrm{s^{-1}}$]	Linewidth[3] std [km $\mathrm{s^{-1}}$]
Young									
G327.29	32	18 (23)	56 (72)%	5.3	-44.9	1.9	1.7	1.7	0.5
G328.25	11	3 (4)	27 (36)%	1.4	-43.1	0.6	1.9	1.6	0.9
G338.93	42	21 (29)	50 (69)%	6.9	-60.9	2.0	2.1	2.0	0.7
G337.92	22	10 (17)	45 (77)%	4.0	-39.2	1.3	2.1	2.0	1.1
W43-MM1	70	32 (51)	46 (73)%	7.5	97.2	2.1	1.9	1.6	1.1
W43-MM2	40	23 (30)	58 (75)%	4.3	90.8	1.3	1.9	1.6	0.9
Average	36	18(26)	49 (71)%	4.9		1.8	1.9	1.7	0.9
Total	217	107 (154)							
Intermediate									
G351.77	18	5 (14)	28 (78)%	5.9	-4.5	2.1	2.0	1.6	0.6
G353.41	45	17 (22)	38 (49)%	7.4	-17.3	1.8	1.7	1.5	0.8
G008.67	19	8 (13)	42 (68)%	6.6	35.8	2.0	2.0	1.9	0.6
W43-MM3	36	12 (18)	33 (50)%	2.6	93.1	0.8	1.8	2.0	0.7
W51-E	23	12 (21)	52 (91)%	11.1	56.8	3.9	2.0	1.6	1.0
Average	28	11(18)	38 (62)%	6.7		2.8	1.8	1.6	0.8
Total	141	54 (88)							
Evolved									
G333.60	52	36 (42)	69 (81)%	10.0	-47.8	1.9	1.7	1.7	0.5
G010.62	42	28 (37)	67 (88)%	9.3	-2.5	2.1	1.4	1.3	0.6
G012.80	46	38 (40)	83 (87)%	6.4	36.1	1.4	1.4	1.2	0.6
W51-IRS2	97	69 (84)	71 (87)%	18.3	61.9	2.9	1.5	1.3	0.8
Average	59	43 (51)	72 (86)%	11.0		2.5	1.5	1.3	0.7
Total	237	171 (203)							

[1] The number of continuum cores is taken from the smoothed core catalogue from Louvet et al. (2023). [2] The number of cores detected and the detection rates (given in percentages) are for single-type DCN detections. The numbers within the brackets are for the sum of the single- and complex-type DCN detections. Spectra described as complex-type spectra are not well fit by a single component. We provide the percentages and number of detections, but cores with a complex-type spectrum are not included in the estimates of the velocity range, V_{LSR}, or linewidth. [3] Only single-type DCN spectra (fit with a single component) and listed as single in the Tables of the DCN fits (e.g. Table 3) are included in the estimates of the velocity ranges, V_{LSR} and linewidth for each protocluster.

Table E.2. DCN hyperfine model.

Hyperfine transition	Frequency [GHz]	Relative Velocity [$\mathrm{kms^{-1}}$]	Relative Line Strength
f1	217.236999	2.12	7
f2	217.238300	0.328	5
f3	217.238538	0.0	21
f4	217.238555	-0.02373	7
f5	217.238612	-0.10239	9
f6	217.239079	-0.7468	5
f7	217.240622	-2.8762	5

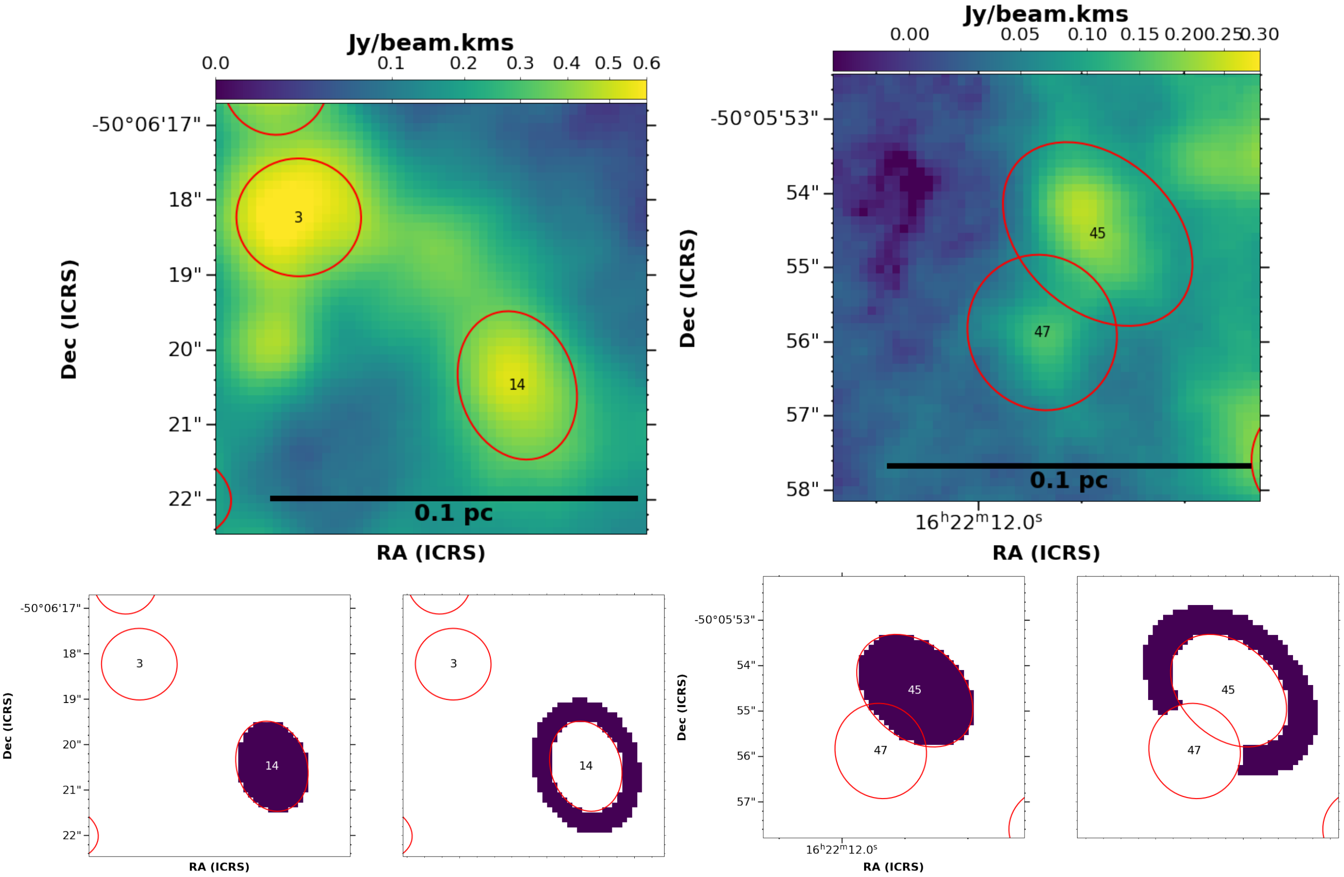

Fig. E.1. Zoom in towards cores 14 (top-left panel) and 45 (top-right panel) overlaid on the DCN moment 0 map in the protocluster G333.60. The red ellipses are 2 times the major (minor) FWHM of the continuum cores. In the bottom panels, we show examples of the masks (shaded blue areas) and their respective annulus (for core 14) or crown (for core 45), that is used to estimate the core-averaged, background-subtracted DCN (3-2) spectra. The background annulus is defined as 2-3 times the core major (minor) FWHMs from Louvet et al. (2023), with pixels from overlapping cores being masked out (i.e. the resulting crown in core 45).

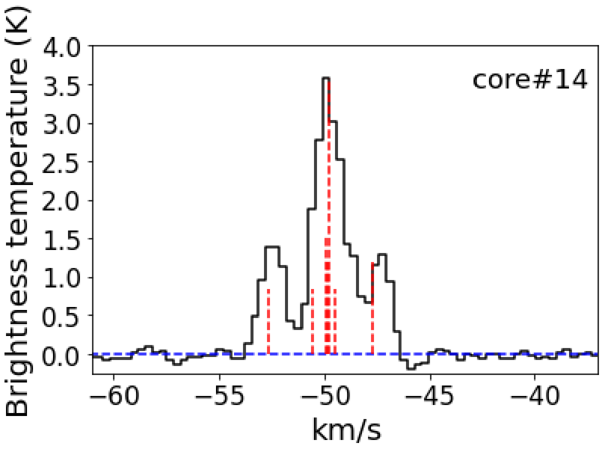

Fig. E.2. Example of the DCN (3-2) core-averaged, background-subtracted spectrum extracted for core 14, in G333.60 with the DCN hyperfine model (see Table E.2) overlaid in red vertical dashed lines and are set relative to the central core $V_{\rm LSR}$.

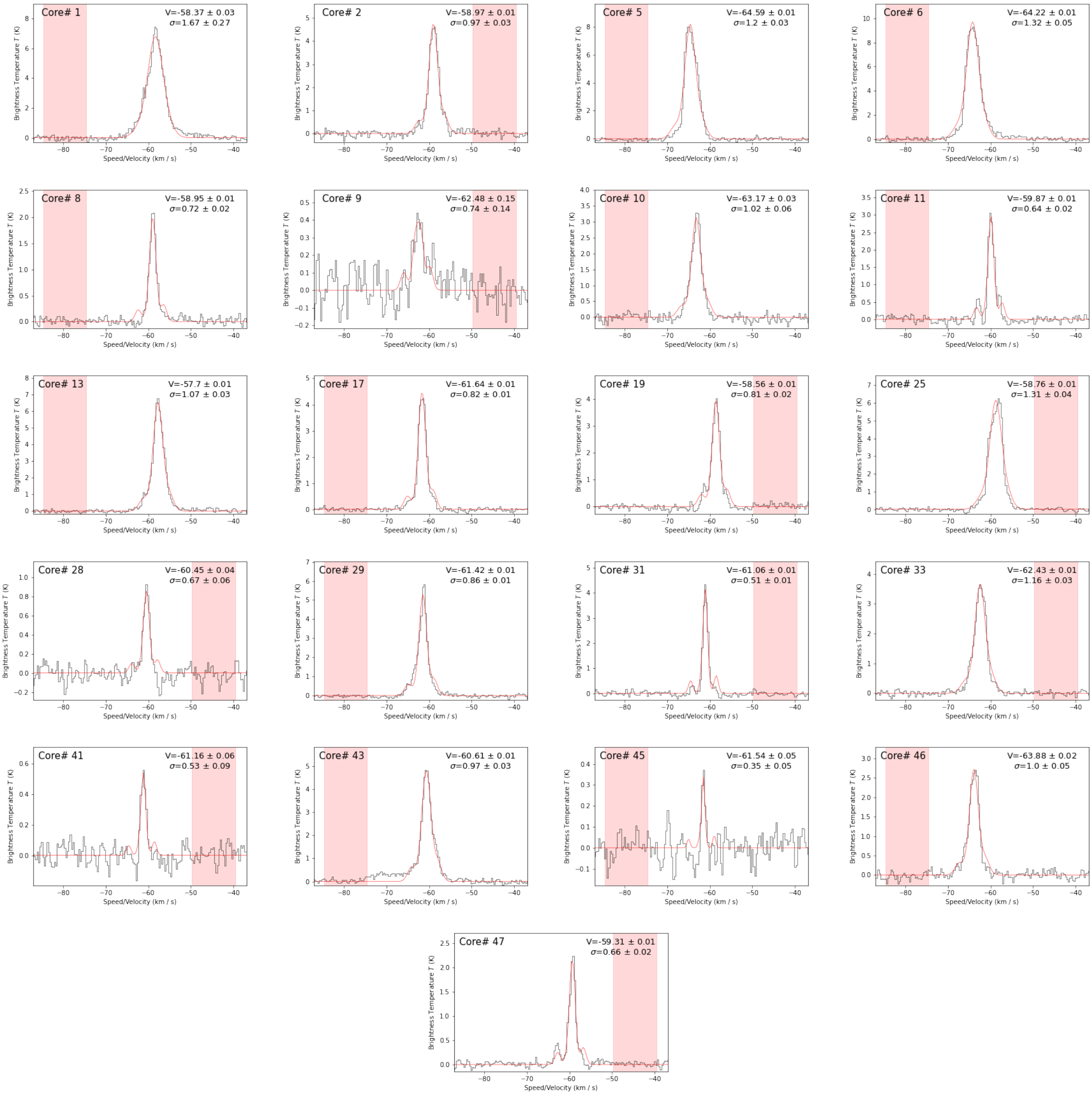

Fig. E.3. Single-type non-background subtracted spectra in the young protocluster G338.93. They are classified in the same way as the background-subtracted spectra. The associated continuum core number is given in the top left of each panel (the core numbering is taken from Louvet et al. 2023) the core V_{LSR} (V) and velocity dispersion (σ) both in units of km s^{-1} from the HSF fit are given in the top right. The pink shaded region represents the part of the spectrum used to estimate the MAD noise.

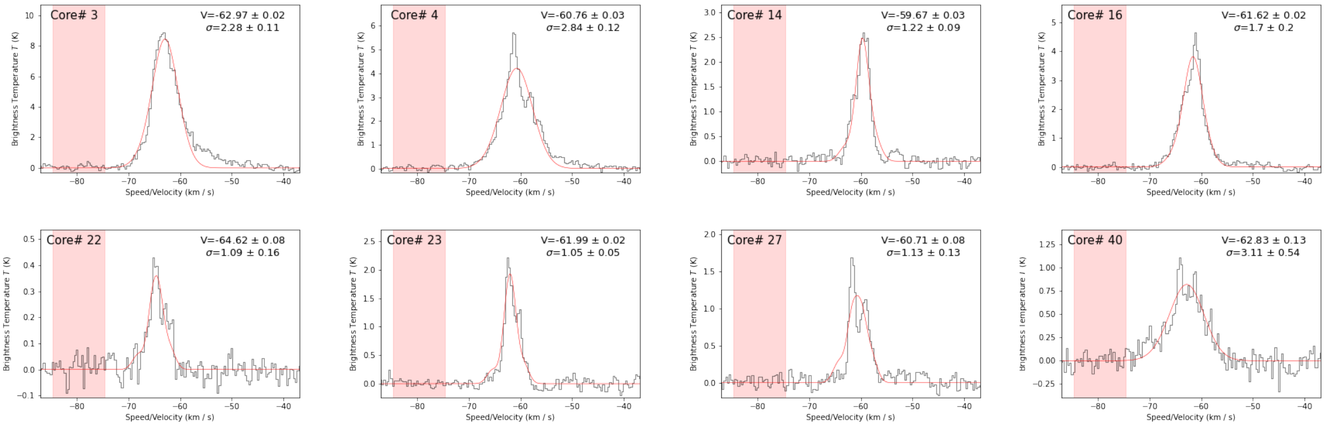

Fig. E.3. continued: Complex-type, non-background subtracted spectra towards the young protocluster G338.93.

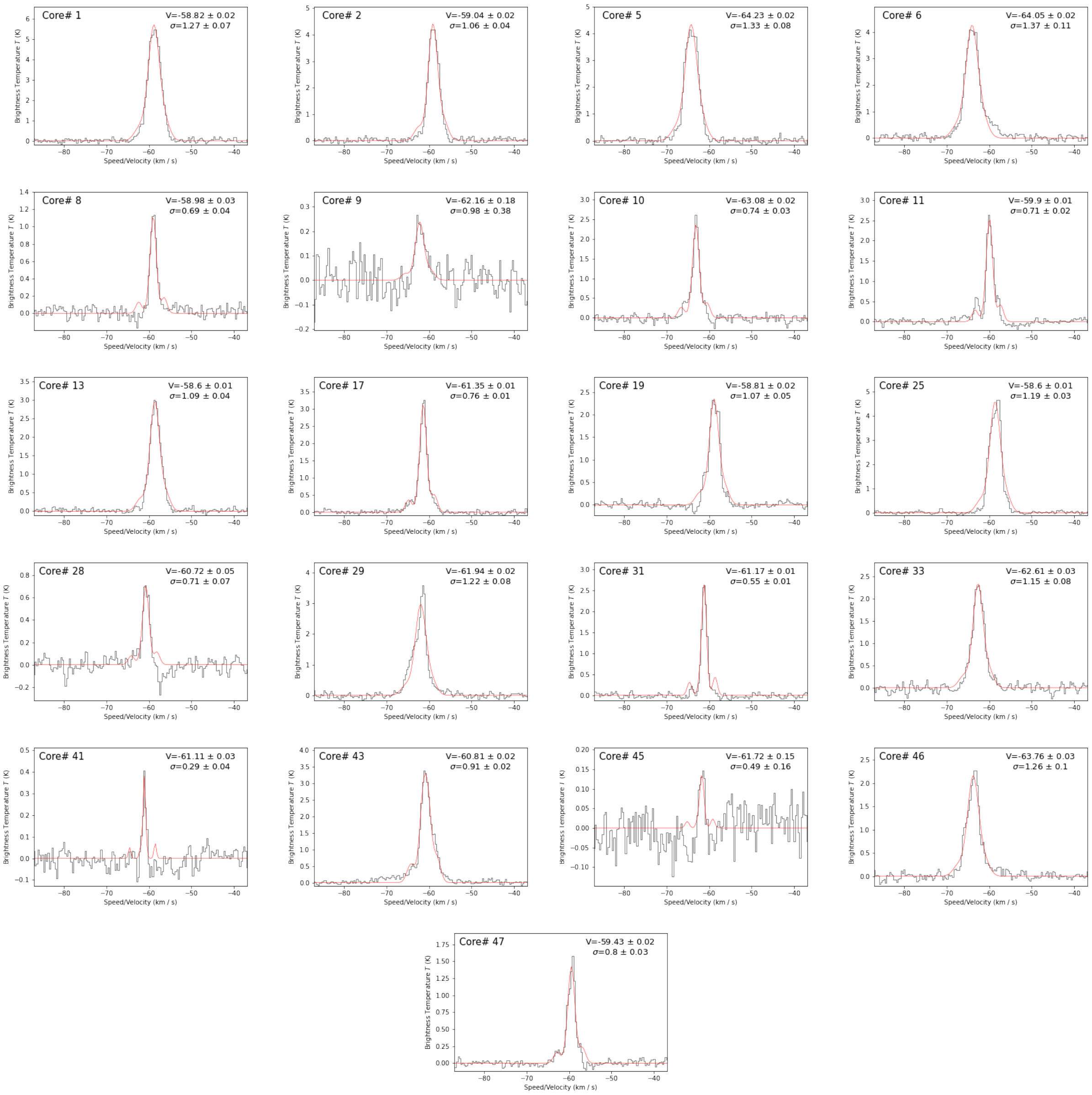

Fig. E.4. Background spectra which are the average spectra from the background annulus or crown towards the positions of the single-type cores shown in Fig. E.3 in the young protocluster G338.93. The associated core numbers are provided in the top left of each panel.

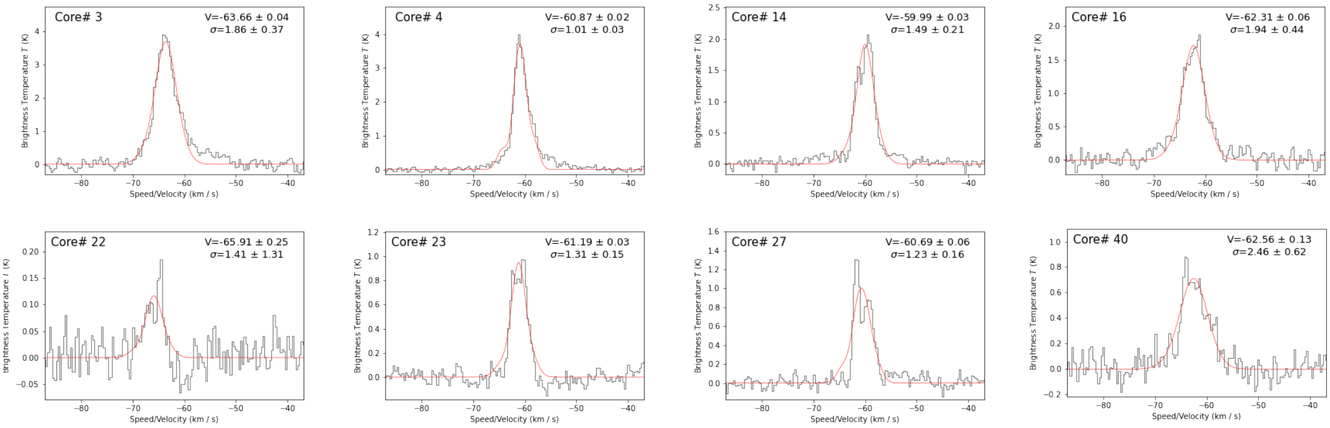

Fig. E.4. continued: Background spectra which are the average spectra from the background annulus towards the positions of the complex-type cores shown in Fig. E.3 in the young protocluster G338.93.

Appendix F: DCN line fits and spectra

We show the extracted single- and complex-type DCN (3-2) spectra for all cores in each of the 15 protoclusters in the ALMA-IMF survey. We also provide the tables of the associated core number, core name, position, and major and minor axes taken from Louvet et al. (2023) along with the DCN line fits extracted for each respective core. If no fit parameters are provided or the name single or complex is not provided, the core was not detected in DCN.

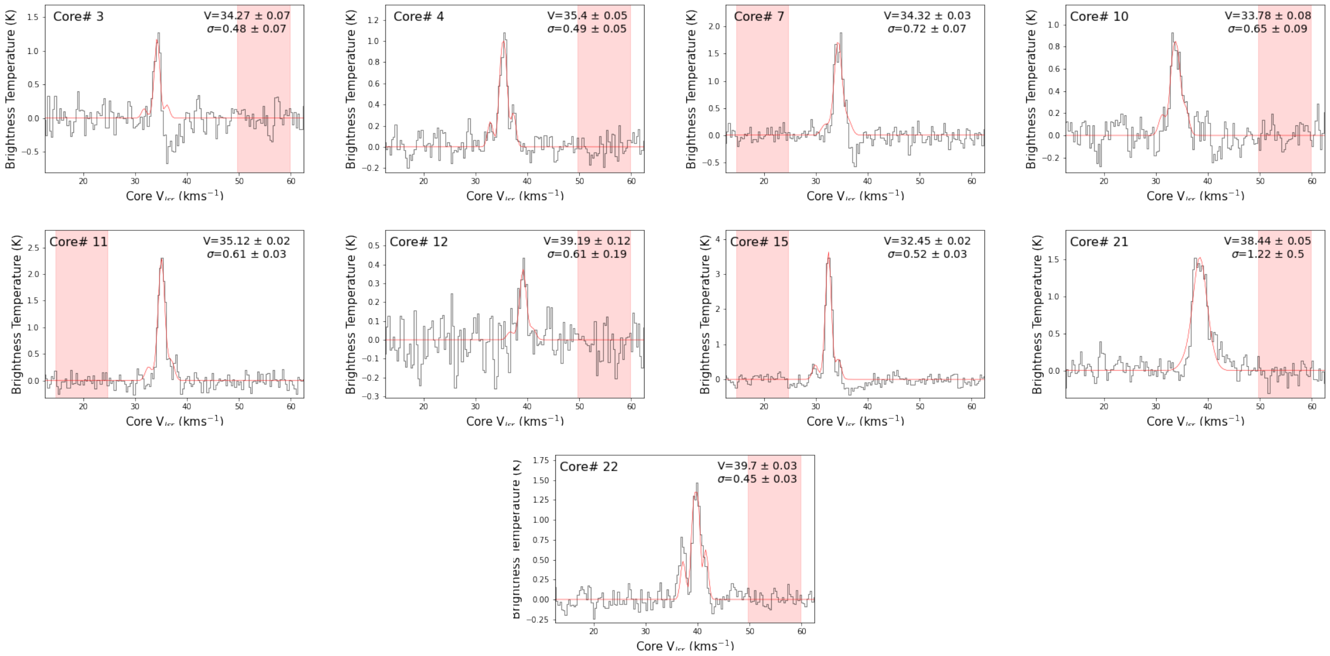

Fig. F.1. Single-type core-averaged, background-subtracted DCN spectra extracted from the cores in the intermediate protocluster G008.67. See Table F.1 for the line fit parameters for each core. The associated continuum core number is given in the top left of each panel (the core numbering is taken from Louvet et al. 2023) the core $V_{\rm LSR}$ (V) and velocity dispersion (σ) both in units of km s^{-1} from the HSF fit are given in the top right. The pink shaded region represents the part of the spectrum used to estimate the MAD noise.

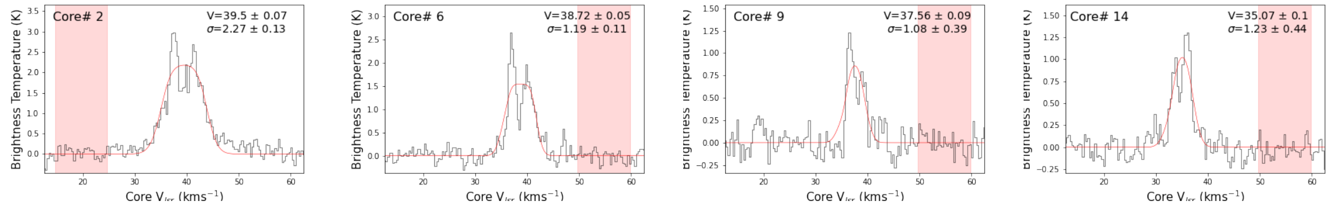

Fig. F.2. Complex-type core-averaged, background-subtracted DCN spectra extracted from cores in the intermediate protocluster G008.67. See Table F.1 for the line fit parameters for each core.

Table F.1. DCN fits towards the core population of the intermediate protocluster G008.67.

n	Core Name	RA [ICRS]	DEC [ICRS]	F_A [″]	F_B [″]	PA [deg]	T [K]	$V_{\rm LSR}$ [km s^{-1}]	Linewidth [km s^{-1}]	Spectral Type
2	271.5978343-21.6195911	18:06:23.48	-21:37:10.53	0.96	0.87	92	100 ± 50	39.5 ± 0.07	–	complex
3	271.5796091-21.6250348	18:06:19.11	-21:37:30.13	0.9	0.79	71	34 ± 7	34.27 ± 0.07	1.14 ± 0.16	single
4	271.580761-21.6237093	18:06:19.38	-21:37:25.35	1.42	1.35	168	27 ± 6	35.4 ± 0.05	1.16 ± 0.11	single
5	271.5785345-21.6222306	18:06:18.85	-21:37:20.03	1.06	0.91	95	24 ± 5	–	–	–
6	271.5980489-21.6198889	18:06:23.53	-21:37:11.60	1.13	1.11	4	29 ± 6	38.72 ± 0.05	–	complex
7	271.5800126-21.6251966	18:06:19.20	-21:37:30.71	1.35	0.96	92	33 ± 7	34.32 ± 0.03	1.69 ± 0.17	single
8	271.5954206-21.620392	18:06:22.90	-21:37:13.41	0.97	0.73	80	25 ± 5	–	–	–
9	271.5985087-21.6198427	18:06:23.64	-21:37:11.43	1.09	0.85	99	28 ± 6	37.56 ± 0.09	–	complex
10	271.5774356-21.6271193	18:06:18.58	-21:37:37.63	1.62	1.29	153	32 ± 6	33.78 ± 0.08	1.53 ± 0.21	single
11	271.5791461-21.6247713	18:06:19.00	-21:37:29.18	1.14	1.03	156	32 ± 7	35.12 ± 0.02	1.43 ± 0.08	single
12	271.5796516-21.6208729	18:06:19.12	-21:37:15.14	1.18	0.98	28	22 ± 5	39.19 ± 0.12	1.43 ± 0.45	single
13	271.5781549-21.622259	18:06:18.76	-21:37:20.13	0.95	0.81	94	24 ± 5	–	–	–
14	271.5798029-21.6239806	18:06:19.15	-21:37:26.33	1.24	1.06	1	28 ± 6	35.07 ± 0.1	–	complex
15	271.5785913-21.6271084	18:06:18.86	-21:37:37.59	1.25	1.15	148	32 ± 6	32.45 ± 0.02	1.24 ± 0.08	single
16	271.5938426-21.6182732	18:06:22.52	-21:37:5.780	1.25	1.05	77	19 ± 4	–	–	–
17	271.5797502-21.6218939	18:06:19.14	-21:37:18.82	1.04	0.83	91	23 ± 5	–	–	–
19	271.5916065-21.6190688	18:06:21.99	-21:37:8.650	2.16	1.4	52	18 ± 4	–	–	–
21	271.5977539-21.6190685	18:06:23.46	-21:37:8.650	1.62	1.21	4	29 ± 6	38.44 ± 0.05	2.87 ± 1.19	single
22	271.5979817-21.6202471	18:06:23.52	-21:37:12.89	1.47	1.41	31	29 ± 6	39.7 ± 0.03	1.06 ± 0.06	single

Table F.2. DCN fits towards the core population of the evolved protocluster G010.62.

n	Core Name	RA [ICRS]	DEC [ICRS]	F_A [″]	F_B [″]	PA [deg]	T [K]	$V_{\rm LSR}$ [km s^{-1}]	Linewidth [km s^{-1}]	Spectral Type
2	272.6133567-19.9299385	18:10:27.21	-19:55:47.78	1.44	0.88	76	29 ± 6	-3.15 ± 0.04	0.98 ± 0.11	single
3	272.6158612-19.9284295	18:10:27.81	-19:55:42.35	1.09	1.03	66	29 ± 6	-2.49 ± 0.02	1.28 ± 0.08	single
4	272.6216933-19.9291438	18:10:29.21	-19:55:44.92	0.71	0.62	97	33 ± 7	-7.64 ± 0.02	1.27 ± 0.06	single
5	272.6106772-19.9271061	18:10:26.56	-19:55:37.58	0.72	0.56	93	25 ± 5	–	–	–
6	272.6218286-19.9280416	18:10:29.24	-19:55:40.95	0.71	0.53	81	100 ± 50	-0.0 ± 0.01	1.22 ± 0.04	single
7	272.6243153-19.9230489	18:10:29.84	-19:55:22.98	0.74	0.62	61	24 ± 5	-1.9 ± 0.09	1.13 ± 0.37	single
8	272.6185252-19.9301787	18:10:28.45	-19:55:48.64	0.64	0.55	114	38 ± 8	1.24 ± 0.07	–	complex
9	272.6130348-19.9319451	18:10:27.13	-19:55:55.00	0.72	0.6	125	29 ± 6	-5.16 ± 0.02	0.62 ± 0.04	single
11	272.6241652-19.9229069	18:10:29.80	-19:55:22.46	0.76	0.57	90	24 ± 5	-1.74 ± 0.05	1.11 ± 0.17	single
14	272.6213499-19.9296433	18:10:29.12	-19:55:46.72	0.92	0.72	86	36 ± 7	-7.43 ± 0.04	–	complex
16	272.6207417-19.929286	18:10:28.98	-19:55:45.43	0.7	0.59	101	36 ± 7	-5.6 ± 0.02	0.69 ± 0.08	single
17	272.6303738-19.922395	18:10:31.29	-19:55:20.62	0.64	0.55	124	19 ± 4	–	–	–
19	272.6234089-19.9273408	18:10:29.62	-19:55:38.43	0.81	0.68	158	29 ± 6	-0.19 ± 0.02	0.86 ± 0.09	single
20	272.6212378-19.9292402	18:10:29.10	-19:55:45.26	0.72	0.49	126	35 ± 7	-6.6 ± 0.07	2.03 ± 0.36	single
21	272.6230891-19.9281344	18:10:29.54	-19:55:41.28	0.76	0.66	110	29 ± 6	–	–	–
22	272.6162629-19.9281751	18:10:27.90	-19:55:41.43	1.94	1.2	165	29 ± 6	-2.44 ± 0.01	1.39 ± 0.05	single
24	272.6222764-19.930054	18:10:29.35	-19:55:48.19	0.93	0.73	113	32 ± 6	-3.32 ± 0.03	–	complex
25	272.6122967-19.9309094	18:10:26.95	-19:55:51.27	0.86	0.73	149	28 ± 6	-4.05 ± 0.01	1.08 ± 0.05	single
26	272.6209449-19.9291949	18:10:29.03	-19:55:45.10	0.79	0.59	73	35 ± 7	-5.6 ± 0.06	0.56 ± 0.13	single
27	272.6175606-19.9309193	18:10:28.21	-19:55:51.31	0.86	0.68	42	34 ± 7	-2.32 ± 0.03	1.1 ± 0.1	single
29	272.6159709-19.9240334	18:10:27.83	-19:55:26.52	1.3	1.26	110	27 ± 5	-1.36 ± 0.04	0.99 ± 0.17	single
33	272.6157835-19.9245689	18:10:27.79	-19:55:28.45	1.02	0.97	176	27 ± 6	-1.03 ± 0.02	0.64 ± 0.07	single
34	272.6177509-19.9302971	18:10:28.26	-19:55:49.07	0.72	0.53	73	35 ± 7	2.43 ± 0.03	1.69 ± 0.07	single
37	272.6222902-19.9232388	18:10:29.35	-19:55:23.66	1.92	1.31	38	25 ± 5	–	–	–
38	272.6243811-19.9276902	18:10:29.85	-19:55:39.68	0.98	0.62	149	27 ± 5	–	–	–
39	272.6205793-19.9284073	18:10:28.94	-19:55:42.27	0.94	0.84	137	32 ± 7	-6.94 ± 0.01	1.17 ± 0.03	single
40	272.6276189-19.922909	18:10:30.63	-19:55:22.47	0.82	0.6	88	21 ± 4	–	–	–
42	272.6163507-19.9286735	18:10:27.92	-19:55:43.22	0.86	0.77	165	29 ± 6	-2.72 ± 0.02	1.64 ± 0.08	single
43	272.6139595-19.9339321	18:10:27.35	-19:56:2.160	0.86	0.62	58	28 ± 6	-0.85 ± 0.02	0.72 ± 0.09	single
44	272.6157525-19.9322865	18:10:27.78	-19:55:56.23	1.22	1.08	92	32 ± 6	-3.07 ± 0.02	1.19 ± 0.09	single
45	272.6172993-19.9301129	18:10:28.15	-19:55:48.41	1.0	0.88	141	33 ± 7	2.04 ± 0.02	–	complex
46	272.6164851-19.9303554	18:10:27.96	-19:55:49.28	0.82	0.78	18	33 ± 7	1.27 ± 0.02	–	complex
47	272.6188053-19.9306895	18:10:28.51	-19:55:50.48	0.73	0.62	54	38 ± 8	-1.97 ± 0.07	1.19 ± 0.12	single
48	272.6121657-19.9212008	18:10:26.92	-19:55:16.32	1.73	1.36	37	23 ± 5	–	–	–
49	272.6190151-19.9284127	18:10:28.56	-19:55:42.29	1.0	0.74	119	33 ± 7	-1.09 ± 0.02	1.12 ± 0.06	single
50	272.6193111-19.9274685	18:10:28.63	-19:55:38.89	0.93	0.79	92	31 ± 6	0.32 ± 0.02	1.45 ± 0.06	single
52	272.6160332-19.9308294	18:10:27.85	-19:55:50.99	1.07	0.8	81	32 ± 7	-2.33 ± 0.12	–	complex
53	272.6236904-19.9272934	18:10:29.69	-19:55:38.26	0.78	0.58	111	28 ± 6	-0.79 ± 0.06	1.3 ± 0.24	single
56	272.6156542-19.9314086	18:10:27.76	-19:55:53.07	0.87	0.74	59	32 ± 6	-3.92 ± 0.03	0.81 ± 0.11	single
58	272.6247409-19.9229049	18:10:29.94	-19:55:22.46	1.33	0.69	55	24 ± 5	–	–	–
60	272.6227533-19.9295616	18:10:29.46	-19:55:46.42	1.08	0.84	69	30 ± 6	-5.29 ± 0.05	1.08 ± 0.17	single
62	272.6145473-19.924069	18:10:27.49	-19:55:26.65	1.04	0.83	156	25 ± 5	-1.65 ± 0.03	0.76 ± 0.12	single

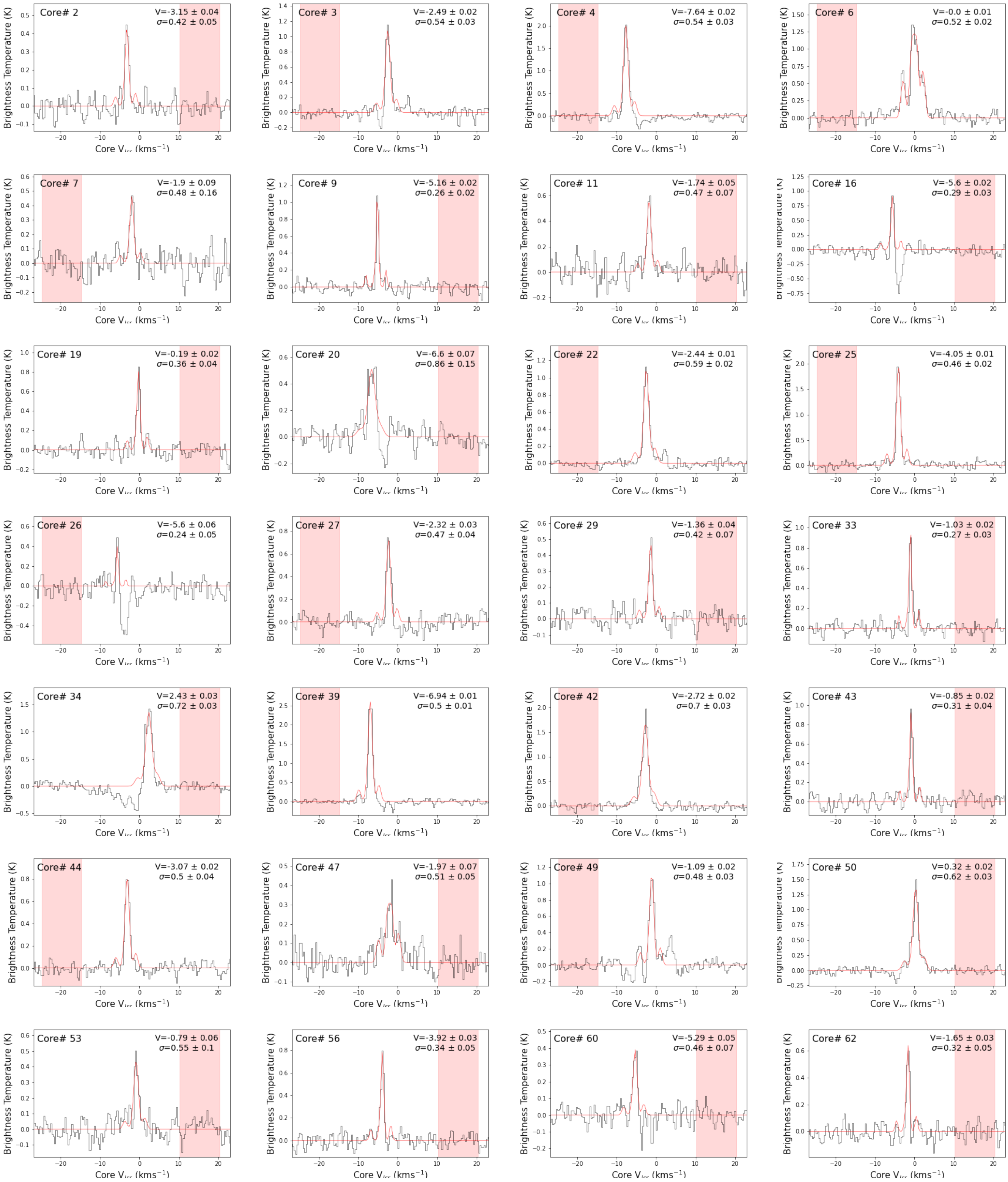

Fig. F.3. Single-type core-averaged, background-subtracted DCN spectra extracted from the cores in the evolved protocluster G010.62. See Table F.2 for the line fit parameters for each core.

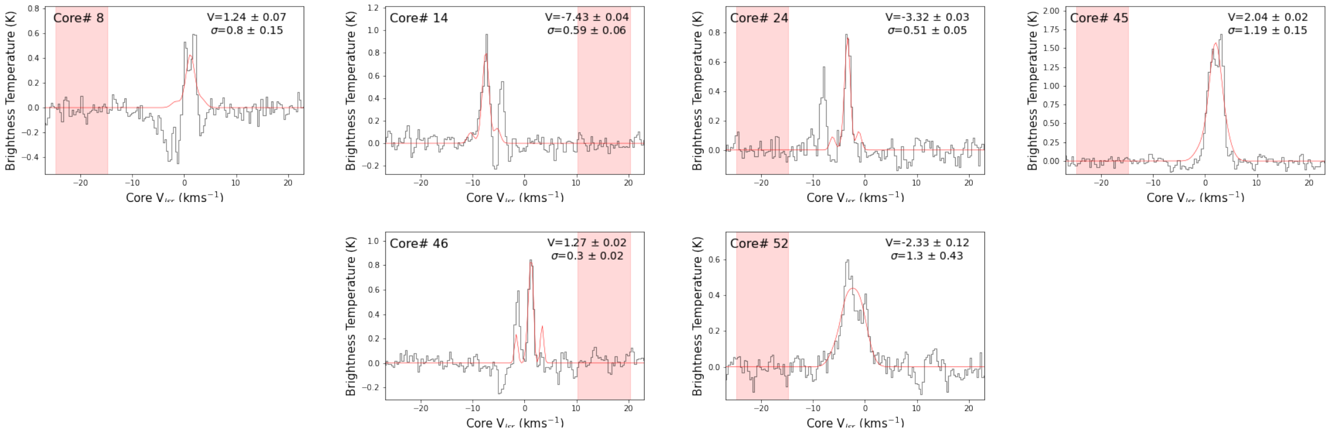

Fig. F.3. Complex-type core-averaged, background-subtracted DCN spectra extracted from the cores in the evolved protocluster G010.62. See Table F.2 for the line fit parameters for each core.

Table F.3. DCN fits towards the core population of the evolved protocluster G012.80.

n	Core Name	RA [ICRS]	DEC [ICRS]	F$_A$ [″]	F$_B$ [″]	PA [deg]	T [K]	V_{LSR} [km s^{-1}]	Linewidth [km s^{-1}]	Spectral Type
1	273.5493292-17.9256817	18:14:11.84	-17:55:32.45	1.6	1.17	57	100 ± 50	37.06 ± 0.06	4.1 ± 0.7	single
3	273.5573504-17.9225106	18:14:13.76	-17:55:21.04	1.84	1.52	8	100 ± 50	36.16 ± 0.04	–	complex
4	273.5444266-17.9375329	18:14:10.66	-17:56:15.12	1.41	1.09	92	25 ± 5	36.16 ± 0.08	1.54 ± 0.27	single
5	273.5482204-17.9458195	18:14:11.57	-17:56:44.95	1.44	1.14	89	23 ± 5	–	–	–
6	273.5531484-17.9208183	18:14:12.76	-17:55:14.95	1.59	1.11	54	29 ± 6	32.6 ± 0.12	2.9 ± 2.8	single
8	273.548615-17.9262103	18:14:11.67	-17:55:34.36	2.35	1.54	69	31 ± 6	36.5 ± 0.03	1.81 ± 0.16	single
9	273.5557419-17.9151082	18:14:13.38	-17:54:54.39	1.46	1.4	26	25 ± 5	–	–	–
10	273.554211-17.9141627	18:14:13.01	-17:54:50.99	1.53	1.09	73	24 ± 5	–	–	–
11	273.5547682-17.9278997	18:14:13.14	-17:55:40.44	1.72	1.42	77	38 ± 8	35.82 ± 0.03	1.65 ± 0.15	single
12	273.5444858-17.9302895	18:14:10.68	-17:55:49.04	1.5	1.37	72	27 ± 5	36.87 ± 0.04	1.22 ± 0.17	single
13	273.5484365-17.9412478	18:14:11.62	-17:56:28.49	1.75	1.54	17	27 ± 5	35.4 ± 0.05	0.84 ± 0.17	single
16	273.5526754-17.9285675	18:14:12.64	-17:55:42.84	1.35	1.07	67	38 ± 8	33.87 ± 0.03	1.26 ± 0.13	single
19	273.5561582-17.9212927	18:14:13.48	-17:55:16.65	1.78	1.46	176	33 ± 7	34.78 ± 0.06	1.43 ± 0.26	single
20	273.5569282-17.9233073	18:14:13.66	-17:55:23.91	1.82	1.27	41	35 ± 7	36.27 ± 0.08	1.28 ± 0.33	single
22	273.5661028-17.9234199	18:14:15.86	-17:55:24.31	1.56	1.18	54	28 ± 6	35.44 ± 0.02	1.06 ± 0.05	single
23	273.5464417-17.9286205	18:14:11.15	-17:55:43.03	1.68	1.35	61	29 ± 6	37.05 ± 0.02	1.05 ± 0.07	single
24	273.5689656-17.9390182	18:14:16.55	-17:56:20.47	2.1	1.31	68	32 ± 6	37.31 ± 0.08	0.92 ± 0.27	single
25	273.5690243-17.9247231	18:14:16.57	-17:55:29.00	1.85	1.23	90	26 ± 5	36.09 ± 0.03	0.71 ± 0.09	single
26	273.5419973-17.932744	18:14:10.08	-17:55:57.88	1.98	1.29	57	25 ± 5	–	–	–
27	273.5561592-17.9348499	18:14:13.48	-17:56:5.460	1.97	1.82	171	30 ± 6	37.53 ± 0.02	0.79 ± 0.09	single
29	273.5516652-17.9189507	18:14:12.40	-17:55:8.220	1.91	1.67	112	27 ± 5	35.87 ± 0.09	1.31 ± 0.27	single
30	273.5576077-17.9311763	18:14:13.83	-17:55:52.23	1.68	1.49	16	32 ± 7	40.0 ± 0.07	2.2 ± 0.75	single
31	273.5676865-17.9204887	18:14:16.24	-17:55:13.76	2.18	1.55	158	26 ± 5	33.52 ± 0.07	0.98 ± 0.19	single
32	273.5470383-17.9333909	18:14:11.29	-17:56:0.210	1.6	1.32	30	27 ± 5	35.39 ± 0.08	1.19 ± 0.28	single
33	273.5581592-17.9252346	18:14:13.96	-17:55:30.84	2.16	1.68	25	34 ± 7	35.31 ± 0.02	0.89 ± 0.07	single
34	273.5465089-17.9276804	18:14:11.16	-17:55:39.65	1.63	1.42	37	29 ± 6	37.57 ± 0.02	1.1 ± 0.06	single
36	273.5569394-17.9239001	18:14:13.67	-17:55:26.04	1.71	1.45	68	35 ± 7	35.82 ± 0.03	1.39 ± 0.14	single
39	273.5665414-17.9228278	18:14:15.97	-17:55:22.18	1.8	1.36	50	27 ± 5	35.17 ± 0.02	1.02 ± 0.05	single
40	273.5457926-17.9284661	18:14:10.99	-17:55:42.48	2.12	1.76	40	28 ± 6	37.31 ± 0.02	1.53 ± 0.09	single
41	273.5662283-17.9256745	18:14:15.89	-17:55:32.43	1.69	1.47	48	29 ± 6	35.02 ± 0.07	1.15 ± 0.28	single
42	273.564807-17.9262439	18:14:15.55	-17:55:34.48	2.01	1.65	98	32 ± 6	36.09 ± 0.06	1.34 ± 0.17	single
44	273.5714882-17.9249465	18:14:17.16	-17:55:29.81	1.37	1.0	73	26 ± 5	–	–	–
45	273.5557839-17.9182388	18:14:13.39	-17:55:5.660	2.75	2.44	7	28 ± 6	35.99 ± 0.08	0.74 ± 0.24	single
46	273.5579243-17.9306652	18:14:13.90	-17:55:50.39	1.83	1.75	45	33 ± 7	39.71 ± 0.05	1.33 ± 0.1	single
47	273.5479984-17.9272905	18:14:11.52	-17:55:38.25	2.22	1.72	44	30 ± 6	35.98 ± 0.02	0.62 ± 0.06	single
51	273.5458037-17.9289719	18:14:10.99	-17:55:44.30	1.75	1.43	77	28 ± 6	37.23 ± 0.02	1.19 ± 0.07	single
52	273.5503813-17.9228494	18:14:12.09	-17:55:22.26	1.6	1.12	67	30 ± 6	34.41 ± 0.05	0.72 ± 0.17	single
53	273.5463654-17.942157	18:14:11.13	-17:56:31.77	1.84	1.37	34	26 ± 5	36.48 ± 0.07	0.6 ± 0.24	single
55	273.5551571-17.9357044	18:14:13.24	-17:56:8.540	2.55	1.99	136	29 ± 6	–	–	–
57	273.5614471-17.9187094	18:14:14.75	-17:55:7.350	2.34	1.89	61	30 ± 6	35.71 ± 0.02	0.74 ± 0.09	single
58	273.559544-17.9178954	18:14:14.29	-17:55:4.420	1.59	1.45	158	30 ± 6	34.27 ± 0.07	1.59 ± 0.33	single
59	273.5529774-17.9374942	18:14:12.71	-17:56:14.98	1.71	1.46	117	29 ± 6	–	–	–
61	273.5475497-17.92664	18:14:11.41	-17:55:35.90	1.69	1.04	60	30 ± 6	37.8 ± 0.02	1.32 ± 0.09	single
62	273.5533917-17.9280329	18:14:12.81	-17:55:40.92	2.13	1.63	94	38 ± 8	34.03 ± 0.02	0.87 ± 0.07	single
65	273.5597707-17.918686	18:14:14.34	-17:55:7.270	1.7	1.52	51	32 ± 6	34.85 ± 0.06	1.65 ± 0.25	single
66	273.5477174-17.9307289	18:14:11.45	-17:55:50.62	2.13	1.44	75	29 ± 6	–	–	–

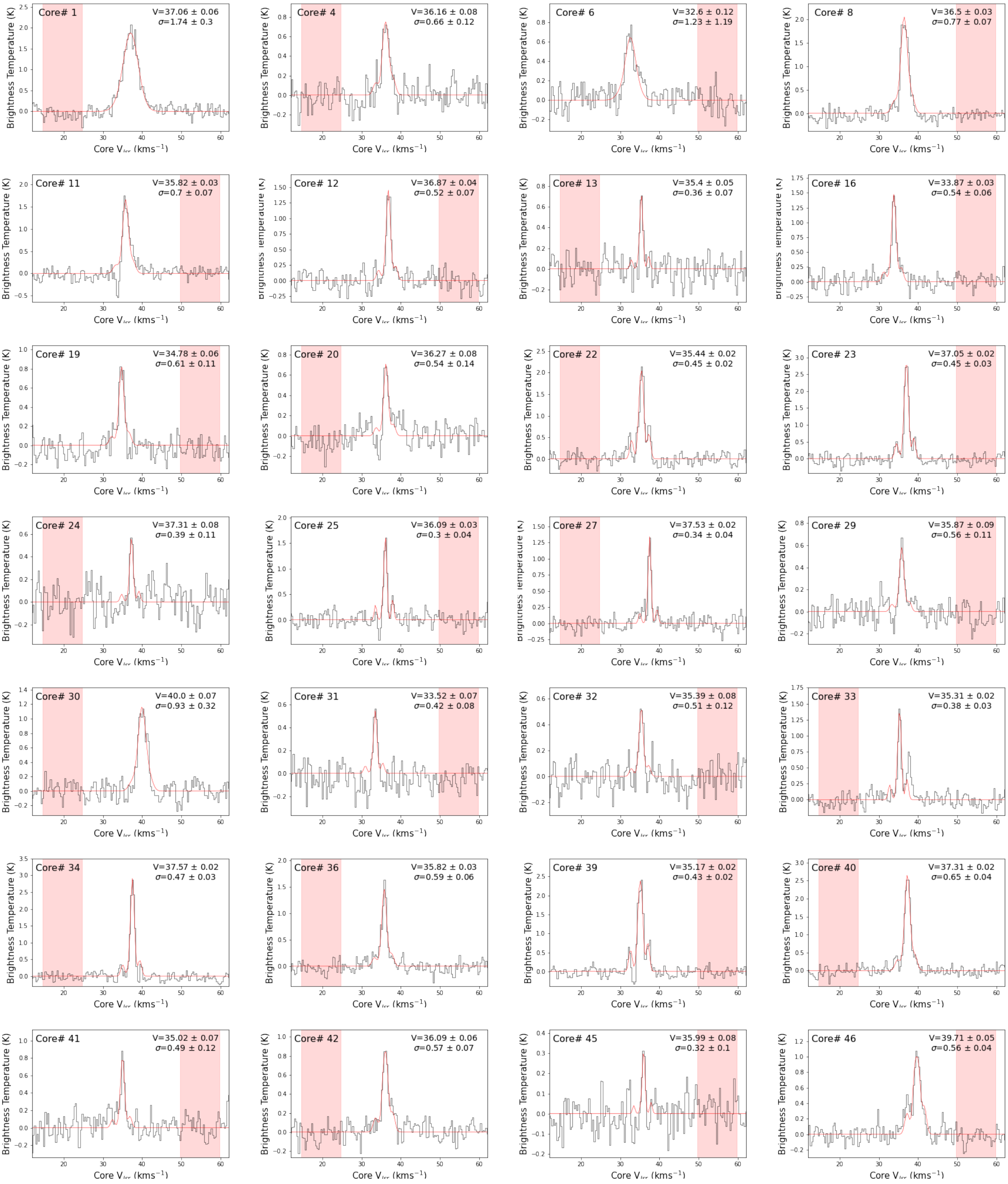

Fig. F.4. Single-type core-averaged, background-subtracted DCN spectra extracted from the cores in the evolved protocluster G012.80. See Table F.3 for the line fit parameters for each core.

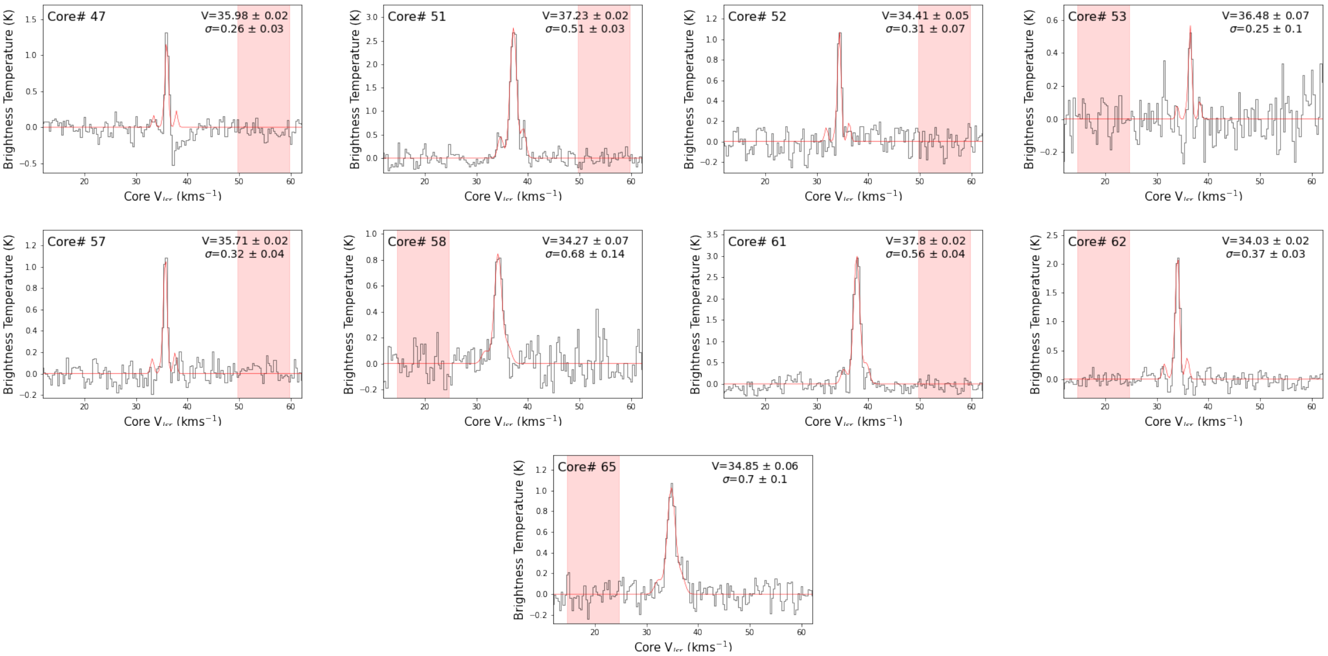

Fig. F.4. continued: Single-type core-averaged, background-subtracted DCN spectra extracted from the cores in the evolved protocluster G012.80. See Table F.3 for the line fit parameters for each core.

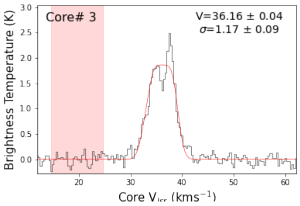

Fig. F.5. Complex-type core-averaged, background-subtracted DCN spectra extracted from the cores in the evolved protocluster G012.80. See Table F.3 for the line fit parameters for each core.

Table F.4. DCN fits towards the core population of the young protocluster G327.29.

n	Core Name	RA [ICRS]	DEC [ICRS]	F_A [″]	F_B [″]	PA [deg]	T [K]	V_{LSR} [km s^{-1}]	Linewidth [km s^{-1}]	Spectral Type
1	238.282335-54.618403	15:53:7.760	-54:37:6.250	2.14	2.09	164	100 ± 50	-42.87 ± 0.13	–	complex
2	238.2894812-54.6168557	15:53:9.480	-54:37:0.680	1.78	1.5	152	28 ± 6	–	–	–
3	238.280656-54.6186811	15:53:7.360	-54:37:7.250	1.62	1.47	62	36 ± 7	-42.18 ± 0.05	–	complex
4	238.2936982-54.6114916	15:53:10.49	-54:36:41.37	1.2	1.19	7	25 ± 5	-44.26 ± 0.1	1.36 ± 0.4	single
5	238.2955904-54.6128047	15:53:10.94	-54:36:46.10	1.7	1.45	64	27 ± 5	-47.08 ± 0.03	1.76 ± 0.09	single
6	238.2938644-54.6110507	15:53:10.53	-54:36:39.78	1.24	1.19	53	25 ± 5	-44.57 ± 0.06	1.06 ± 0.21	single
7	238.2961992-54.6133521	15:53:11.09	-54:36:48.07	1.6	1.41	129	26 ± 5	-47.79 ± 0.05	1.98 ± 0.22	single
8	238.2983074-54.6069915	15:53:11.59	-54:36:25.17	1.32	1.19	16	26 ± 5	-47.41 ± 0.08	1.21 ± 0.28	single
9	238.2858254-54.6172552	15:53:8.600	-54:37:2.120	1.39	1.13	73	29 ± 6	-44.42 ± 0.04	0.95 ± 0.15	single
10	238.2605463-54.6233229	15:53:2.530	-54:37:23.96	1.16	1.04	134	24 ± 5	–	–	–
11	238.2800319-54.6194279	15:53:7.210	-54:37:9.940	2.35	1.32	32	33 ± 7	-42.11 ± 0.02	1.1 ± 0.06	single
12	238.2838451-54.6216681	15:53:8.120	-54:37:18.01	1.72	1.38	59	24 ± 5	–	–	–
13	238.2903446-54.6123086	15:53:9.680	-54:36:44.31	1.35	1.26	36	24 ± 5	–	–	–
14	238.2971584-54.609653	15:53:11.32	-54:36:34.75	1.34	1.26	163	25 ± 5	-47.17 ± 0.06	1.26 ± 0.21	single
15	238.2867749-54.6166625	15:53:8.830	-54:36:59.98	1.76	1.44	47	28 ± 6	-43.64 ± 0.03	1.76 ± 0.15	single
16	238.2891016-54.6143036	15:53:9.380	-54:36:51.49	1.64	1.47	114	25 ± 5	–	–	–
17	238.2893864-54.6162879	15:53:9.450	-54:36:58.64	1.49	1.21	114	27 ± 6	-45.32 ± 0.2	–	complex
18	238.2800971-54.6177887	15:53:7.220	-54:37:4.040	1.14	1.03	76	32 ± 7	–	–	–
19	238.2810557-54.62136	15:53:7.450	-54:37:16.90	1.99	1.76	113	25 ± 5	-42.75 ± 0.07	1.01 ± 0.23	single
20	238.2935252-54.6140562	15:53:10.45	-54:36:50.60	1.36	1.1	26	24 ± 5	–	–	–
21	238.2959968-54.6118908	15:53:11.04	-54:36:42.81	1.18	1.12	15	25 ± 5	-46.74 ± 0.04	0.9 ± 0.15	single
22	238.2884448-54.6163242	15:53:9.230	-54:36:58.77	1.83	1.64	171	27 ± 6	-45.19 ± 0.05	1.49 ± 0.15	single
23	238.2946778-54.6130334	15:53:10.72	-54:36:46.92	1.37	1.29	113	26 ± 5	-46.49 ± 0.13	–	complex
24	238.2656528-54.6238211	15:53:3.760	-54:37:25.76	3.17	2.47	59	24 ± 5	–	–	–
25	238.2865705-54.6187657	15:53:8.780	-54:37:7.560	2.44	2.21	17	28 ± 6	-42.85 ± 0.05	1.62 ± 0.13	single
26	238.2966528-54.615169	15:53:11.20	-54:36:54.61	2.24	1.92	16	23 ± 5	–	–	–
27	238.2945683-54.6089436	15:53:10.70	-54:36:32.20	1.24	1.02	8	26 ± 5	–	–	–
28	238.2889899-54.6256413	15:53:9.360	-54:37:32.31	3.44	2.78	138	22 ± 5	–	–	–
29	238.2902959-54.6140325	15:53:9.670	-54:36:50.52	1.66	1.56	59	24 ± 5	–	–	–
30	238.2937964-54.610052	15:53:10.51	-54:36:36.19	1.43	1.18	88	25 ± 5	–	–	–
31	238.2856418-54.6266832	15:53:8.550	-54:37:36.06	3.37	2.73	159	23 ± 5	–	–	–
34	238.285875-54.6233919	15:53:8.610	-54:37:24.21	2.18	1.52	149	23 ± 5	–	–	–

Table F.5. DCN fits towards the core population of the young protocluster G328.25.

n	Core Name	RA [ICRS]	DEC [ICRS]	F_A [″]	F_B [″]	PA [deg]	T [K]	V_{LSR} [km s^{-1}]	Linewidth [km s^{-1}]	Spectral Type
1	239.4991778-53.9668493	15:57:59.80	-53:58:0.660	1.49	1.32	29	100 ± 50	-43.09 ± 0.05	–	complex
2	239.4978364-53.9537718	15:57:59.48	-53:57:13.58	1.28	1.16	12	23 ± 5	–	–	–
3	239.5016973-53.954434	15:58:0.410	-53:57:15.96	1.81	1.3	14	23 ± 5	–	–	–
4	239.4941628-53.9528437	15:57:58.60	-53:57:10.24	1.15	1.07	135	22 ± 4	–	–	–
5	239.5209961-53.959408	15:58:5.040	-53:57:33.87	1.32	1.19	145	23 ± 5	–	–	–
6	239.4815006-53.9554302	15:57:55.56	-53:57:19.55	1.34	1.07	118	21 ± 4	–	–	–
7	239.5135243-53.965875	15:58:3.250	-53:57:57.15	1.23	1.01	175	23 ± 5	–	–	–
8	239.5146161-53.968461	15:58:3.510	-53:58:6.460	1.14	1.12	108	23 ± 5	–	–	–
9	239.5000898-53.9663118	15:58:0.020	-53:57:58.72	2.02	1.41	30	36 ± 7	-43.0 ± 0.02	1.21 ± 0.06	single
10	239.4979744-53.9667109	15:57:59.51	-53:58:0.160	2.31	1.93	102	37 ± 8	-41.27 ± 0.09	3.69 ± 1.24	single
11	239.4964686-53.9654253	15:57:59.15	-53:57:55.53	1.6	1.26	3	33 ± 7	-43.77 ± 0.06	1.11 ± 0.2	single

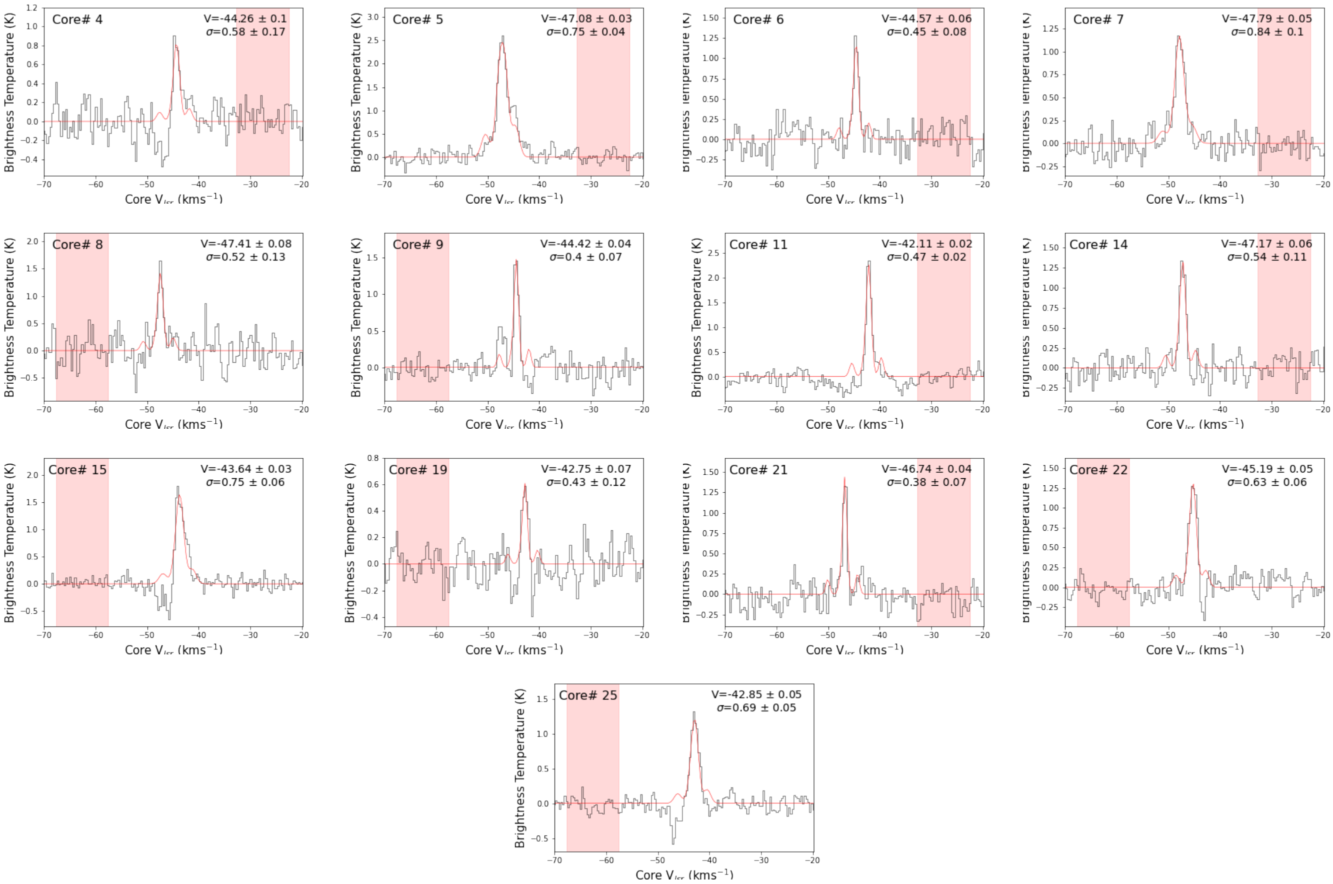

Fig. F.6. single-type core-averaged, background-subtracted DCN spectra extracted from the cores in the young protocluster G327.29. See Table F.4 for the line fit parameters for each core.

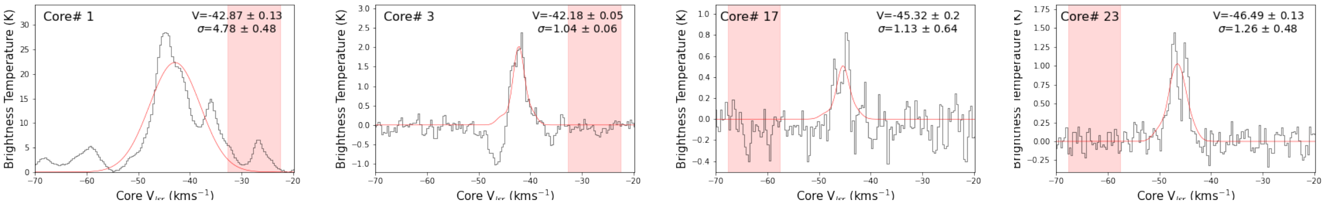

Fig. F.6. Complex-type core-averaged, background-subtracted DCN spectra extracted from the cores in the young protocluster G327.29. See Table F.4 for the line fit parameters for each core.

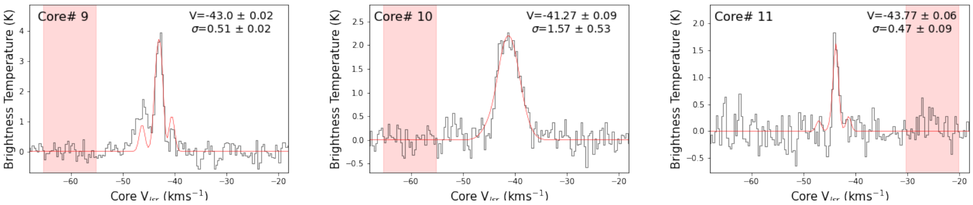

Fig. F.7. Single-type core-averaged, background-subtracted DCN spectra extracted from the cores in the young protocluster G328.25. See Table F.5 for the line fit parameters for each core.

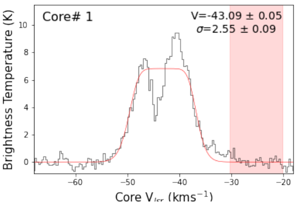

Fig. F.8. Complex-type core-averaged, background-subtracted DCN spectra extracted from the cores in the young protocluster G328.25. See Table F.5 for the line fit parameters for each core.

Table F.6. DCN fits towards the core population of the young protocluster G337.92.

n	Core Name	RA [ICRS]	DEC [ICRS]	F$_A$ [″]	F$_B$ [″]	PA [deg]	T [K]	$V_{\rm LSR}$ [km s^{-1}]	Linewidth [km s^{-1}]	Spectral Type
1	250.2935548-47.1342727	16:41:10.45	-47:08:3.380	1.61	1.23	105	100 ± 50	-41.92 ± 0.02	–	complex
2	250.2936172-47.133748	16:41:10.47	-47:08:1.490	1.85	1.27	69	35 ± 10	-38.58 ± 0.01	–	complex
3	250.2949021-47.1343006	16:41:10.78	-47:08:3.480	1.51	1.35	170	33 ± 7	0.0 ± 0.0	–	complex
4	250.2922563-47.1415274	16:41:10.14	-47:08:29.50	1.22	1.06	73	18 ± 4	–	–	–
5	250.295556-47.134715	16:41:10.93	-47:08:4.970	1.8	1.46	124	30 ± 6	-36.83 ± 0.02	3.61 ± 0.34	single
6	250.2913536-47.1405094	16:41:9.920	-47:08:25.83	1.19	1.15	8	20 ± 4	–	–	–
7	250.2794944-47.1323197	16:41:7.080	-47:07:56.35	1.3	1.01	115	19 ± 4	-40.4 ± 0.07	1.66 ± 0.29	single
8	250.2927529-47.1352673	16:41:10.26	-47:08:6.960	1.46	1.21	122	31 ± 6	-39.36 ± 0.01	–	complex
9	250.294383-47.1348356	16:41:10.65	-47:08:5.410	1.52	1.41	162	33 ± 7	-39.91 ± 0.07	–	complex
10	250.2841444-47.1340494	16:41:8.190	-47:08:2.580	2.14	1.24	83	22 ± 5	-40.69 ± 0.03	1.16 ± 0.09	single
12	250.2947667-47.1443172	16:41:10.74	-47:08:39.54	1.29	1.09	122	18 ± 4	–	–	–
13	250.293043-47.1316977	16:41:10.33	-47:07:54.11	2.23	1.68	43	28 ± 6	-40.04 ± 0.04	3.09 ± 0.59	single
14	250.2952101-47.1340394	16:41:10.85	-47:08:2.540	1.23	1.06	111	31 ± 6	-37.78 ± 0.04	–	complex
15	250.2920694-47.1443736	16:41:10.10	-47:08:39.74	1.22	1.06	37	18 ± 4	–	–	–
16	250.2886082-47.1330445	16:41:9.270	-47:07:58.96	1.09	1.03	15	26 ± 5	–	–	–
17	250.294635-47.1334957	16:41:10.71	-47:08:0.580	1.81	1.05	66	31 ± 6	-38.12 ± 0.03	4.5 ± 0.5	single
18	250.2879462-47.1399751	16:41:9.110	-47:08:23.91	1.71	1.44	46	21 ± 4	-38.22 ± 0.16	2.18 ± 0.75	single
19	250.2789162-47.1329451	16:41:6.940	-47:07:58.60	1.63	1.14	8	20 ± 4	-39.91 ± 0.04	0.54 ± 0.14	single
20	250.2867777-47.1382501	16:41:8.830	-47:08:17.70	1.82	1.41	165	22 ± 5	-38.4 ± 0.13	–	complex
21	250.2897651-47.1412616	16:41:9.540	-47:08:28.54	1.21	0.92	2	19 ± 4	–	–	–
23	250.2913342-47.1396608	16:41:9.920	-47:08:22.78	1.4	1.26	19	22 ± 4	–	–	–
25	250.2914162-47.134249	16:41:9.940	-47:08:3.300	1.61	1.36	174	30 ± 6	-39.43 ± 0.02	1.8 ± 0.07	single

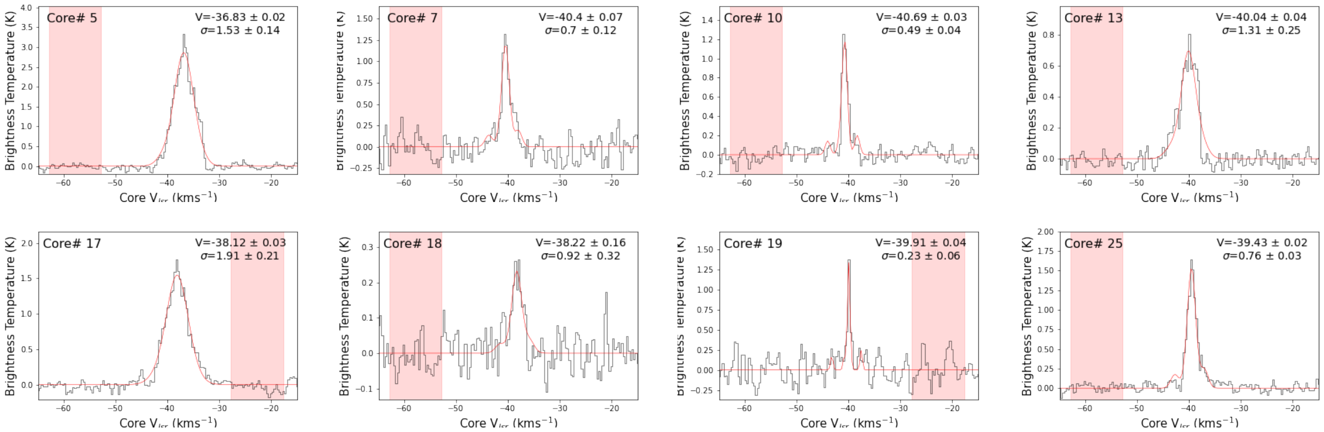

Fig. F.9. Single-type core-averaged, background-subtracted DCN spectra extracted from the cores in the young protocluster G337.92. See Table F.6 for the line fit parameters for each core.

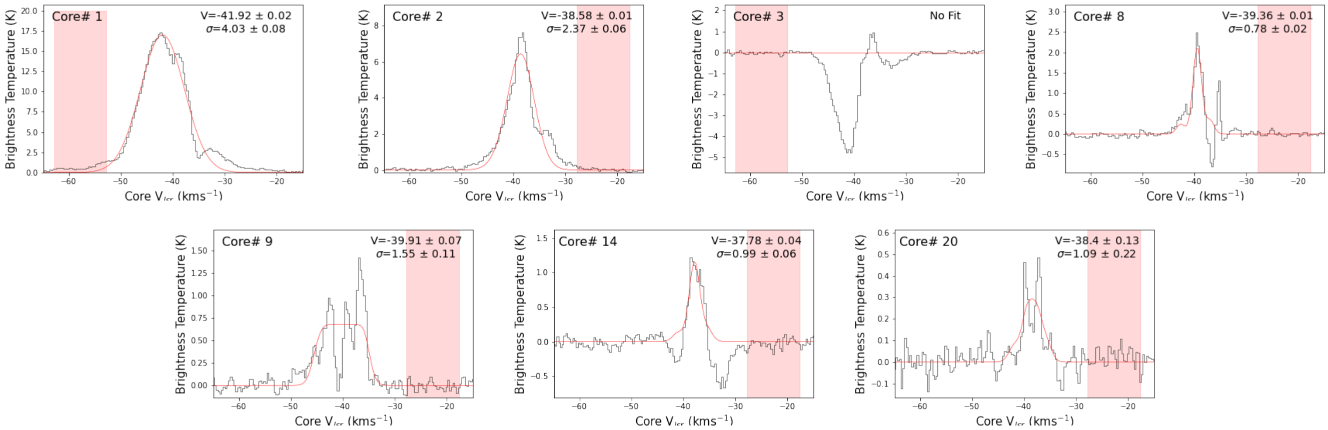

Fig. F.10. Complex-type core-averaged, background-subtracted DCN spectra extracted from the cores in the young protocluster G337.92. See Table F.6 for the line fit parameters for each core.

Table F.7. DCN fits towards the core population of the young protocluster G338.93.

n	Core Name	RA [ICRS]	DEC [ICRS]	F_A [″]	F_B [″]	PA [deg]	T [K]	V_{LSR} [km s^{-1}]	Linewidth [km s^{-1}]	Spectral Type
1	250.1422011-45.6934028	16:40:34.13	-45:41:36.25	0.89	0.79	84	100 ± 50	-57.34 ± 0.08	–	complex
2	250.1427268-45.6936217	16:40:34.25	-45:41:37.04	0.97	0.73	124	100 ± 50	-58.71 ± 0.08	–	complex
3	250.1417044-45.7020244	16:40:34.01	-45:42:7.290	0.86	0.79	92	100 ± 50	-62.49 ± 0.03	–	complex
4	250.1397543-45.6936984	16:40:33.54	-45:41:37.31	0.86	0.82	7	100 ± 50	-60.37 ± 0.04	–	complex
5	250.1417392-45.7025004	16:40:34.02	-45:42:9.000	0.86	0.79	89	36 ± 7	-64.94 ± 0.02	2.19 ± 0.07	single
6	250.1419183-45.7022799	16:40:34.06	-45:42:8.210	1.0	0.86	65	35 ± 10	-64.36 ± 0.01	2.98 ± 0.12	single
7	250.1378537-45.7040233	16:40:33.08	-45:42:14.48	0.81	0.76	56	30 ± 6	–	–	–
8	250.1433977-45.6938542	16:40:34.42	-45:41:37.88	1.42	0.88	119	27 ± 6	-58.93 ± 0.03	1.81 ± 0.12	single
9	250.1497218-45.6929092	16:40:35.93	-45:41:34.47	0.98	0.74	29	24 ± 5	–	–	–
10	250.1403862-45.7027264	16:40:33.69	-45:42:9.820	1.02	0.88	63	100 ± 50	-63.32 ± 0.07	–	complex
11	250.1409277-45.6954519	16:40:33.82	-45:41:43.63	0.87	0.74	15	27 ± 6	-59.8 ± 0.05	0.95 ± 0.2	single
12	250.1444989-45.69665	16:40:34.68	-45:41:47.94	1.99	1.75	16	24 ± 5	–	–	–
13	250.1423231-45.6931039	16:40:34.16	-45:41:35.17	1.06	1.04	129	29 ± 6	-57.29 ± 0.02	2.12 ± 0.09	single
14	250.1394346-45.6928199	16:40:33.46	-45:41:34.15	0.87	0.7	72	28 ± 6	-59.26 ± 0.06	1.69 ± 0.17	single
15	250.1461922-45.6894135	16:40:35.09	-45:41:21.89	1.68	1.26	124	24 ± 5	–	–	–
16	250.1418854-45.701708	16:40:34.05	-45:42:6.150	1.06	0.98	72	33 ± 7	-61.06 ± 0.03	2.78 ± 0.2	single
17	250.139044-45.6942019	16:40:33.37	-45:41:39.13	1.25	1.05	20	30 ± 6	-62.1 ± 0.01	1.44 ± 0.04	single
18	250.1508635-45.6953106	16:40:36.21	-45:41:43.12	1.28	1.1	63	24 ± 5	–	–	–
19	250.1409412-45.693164	16:40:33.83	-45:41:35.39	0.92	0.89	118	26 ± 5	-58.47 ± 0.01	1.03 ± 0.04	single
21	250.1528564-45.6839538	16:40:36.69	-45:41:2.230	1.23	0.99	114	24 ± 5	–	–	–
22	250.1435778-45.6996258	16:40:34.46	-45:41:58.65	2.09	1.82	21	25 ± 5	-63.63 ± 0.19	–	complex
23	250.1390889-45.6957652	16:40:33.38	-45:41:44.75	1.01	0.89	170	28 ± 6	-62.41 ± 0.03	1.79 ± 0.14	single
24	250.1386357-45.6860028	16:40:33.27	-45:41:9.610	0.78	0.75	86	24 ± 5	–	–	–
25	250.1417571-45.6936655	16:40:34.02	-45:41:37.20	1.12	1.03	40	28 ± 6	-59.3 ± 0.03	–	complex
27	250.1396701-45.6923769	16:40:33.52	-45:41:32.56	0.92	0.73	32	26 ± 5	-60.67 ± 0.28	–	complex
28	250.138712-45.6950579	16:40:33.29	-45:41:42.21	0.93	0.81	172	29 ± 6	-60.03 ± 0.08	1.02 ± 0.32	single
29	250.1412979-45.7015713	16:40:33.91	-45:42:5.660	1.33	1.1	129	32 ± 7	-61.06 ± 0.02	1.46 ± 0.04	single
30	250.1517326-45.6946186	16:40:36.42	-45:41:40.63	1.06	0.88	180	24 ± 5	–	–	–
31	250.1380669-45.6941846	16:40:33.14	-45:41:39.06	1.0	0.91	112	30 ± 6	-60.93 ± 0.02	1.05 ± 0.05	single
33	250.1415524-45.7011978	16:40:33.97	-45:42:4.310	1.09	1.0	21	29 ± 6	-62.1 ± 0.04	2.53 ± 0.25	single
34	250.1519045-45.6953464	16:40:36.46	-45:41:43.25	1.21	1.05	144	24 ± 5	–	–	–
35	250.1430564-45.7006254	16:40:34.33	-45:42:2.250	1.52	1.39	30	26 ± 5	–	–	–
37	250.1366979-45.6914341	16:40:32.81	-45:41:29.16	1.57	1.47	155	27 ± 5	-61.98 ± 0.07	0.66 ± 0.24	single
38	250.1355573-45.7039553	16:40:32.53	-45:42:14.24	1.53	1.29	180	25 ± 5	–	–	–
39	250.1511653-45.6876105	16:40:36.28	-45:41:15.40	2.35	1.71	179	24 ± 5	–	–	–
40	250.1425257-45.7017414	16:40:34.21	-45:42:6.270	0.83	0.57	71	31 ± 6	–	–	–
41	250.1363471-45.6947624	16:40:32.72	-45:41:41.14	1.33	1.24	80	27 ± 6	–	–	–
42	250.1380589-45.697165	16:40:33.13	-45:41:49.79	1.5	1.26	90	26 ± 5	–	–	–
43	250.1392522-45.6932893	16:40:33.42	-45:41:35.84	1.2	0.8	134	30 ± 6	-60.3 ± 0.02	1.76 ± 0.09	single
45	250.1373942-45.6927488	16:40:32.97	-45:41:33.90	1.44	0.97	157	28 ± 6	–	–	–
46	250.1406937-45.7022641	16:40:33.77	-45:42:8.150	1.11	0.82	38	34 ± 7	-64.11 ± 0.07	1.22 ± 0.29	single
47	250.1421862-45.6953419	16:40:34.12	-45:41:43.23	1.47	1.17	106	26 ± 5	-59.23 ± 0.03	0.96 ± 0.11	single

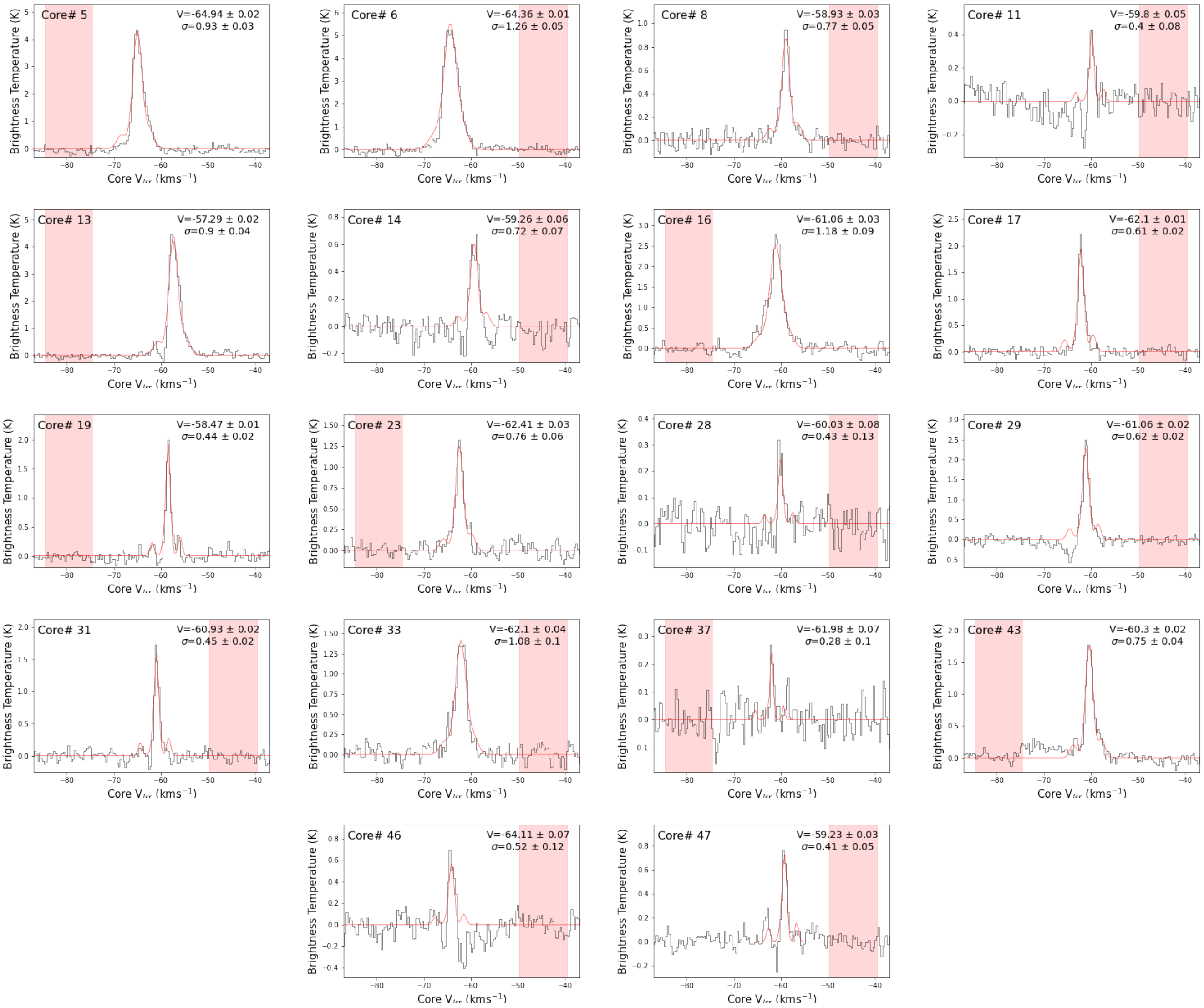

Fig. F.11. Single-type core-averaged, background-subtracted DCN spectra extracted from the cores in the young protocluster G338.93. See Table F.7 for the line fit parameters for each core.

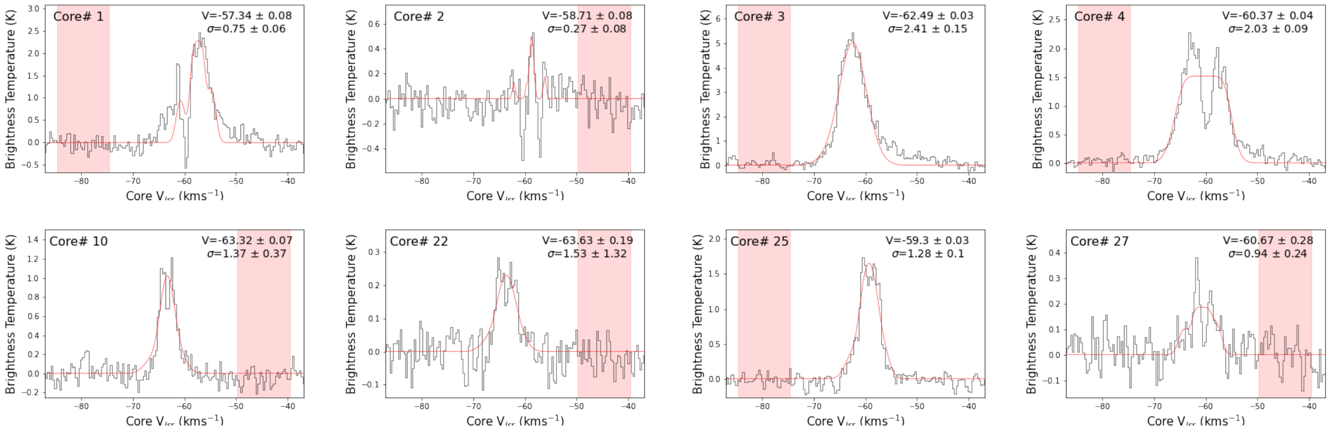

Fig. F.12. Complex-type core-averaged, background-subtracted DCN spectra extracted from the cores in the young protocluster G338.93. See Table F.7 for the line fit parameters for each core.

Table F.8. DCN fits towards the core population of the evolved protocluster G333.60.

n	Core Name	RA [ICRS]	DEC [ICRS]	F_A [″]	F_B [″]	PA [deg]	T [K]	$V_{\rm LSR}$ [km s^{-1}]	Linewidth [km s^{-1}]	Spectral Type
1	245.5468006-50.0988073	16:22:11.23	-50:05:55.71	1.41	0.9	67	38 ± 8	-49.51 ± 0.02	1.99 ± 0.1	single
2	245.5356169-50.104813	16:22:8.550	-50:06:17.33	0.94	0.75	67	37 ± 8	-48.48 ± 0.03	–	complex
3	245.528392-50.1050657	16:22:6.810	-50:06:18.24	0.83	0.79	88	33 ± 7	-49.87 ± 0.02	–	complex
4	245.5460571-50.0990531	16:22:11.05	-50:05:56.59	0.85	0.63	47	100 ± 50	-51.35 ± 0.07	–	complex
5	245.5285258-50.1045541	16:22:6.850	-50:06:16.39	0.74	0.71	8	32 ± 7	-48.75 ± 0.04	–	complex
7	245.5370048-50.1027976	16:22:8.880	-50:06:10.07	1.3	0.96	24	38 ± 8	-46.37 ± 0.04	2.76 ± 0.31	single
8	245.5282954-50.1068134	16:22:6.790	-50:06:24.53	1.0	0.77	50	30 ± 6	-50.16 ± 0.01	1.22 ± 0.03	single
11	245.5357042-50.1033887	16:22:8.570	-50:06:12.20	1.33	1.13	36	100 ± 50	-47.33 ± 0.02	2.02 ± 0.09	single
14	245.5271272-50.1056891	16:22:6.510	-50:06:20.48	1.01	0.77	18	31 ± 6	-49.83 ± 0.01	1.25 ± 0.02	single
18	245.5296271-50.1064415	16:22:7.110	-50:06:23.19	0.69	0.6	43	31 ± 6	-50.22 ± 0.07	–	complex
19	245.5270406-50.1089457	16:22:6.490	-50:06:32.20	1.25	1.07	151	28 ± 6	-47.89 ± 0.01	1.15 ± 0.04	single
21	245.5311806-50.1042724	16:22:7.480	-50:06:15.38	1.17	1.04	16	34 ± 7	-50.18 ± 0.01	1.25 ± 0.03	single
22	245.5170221-50.1089966	16:22:4.090	-50:06:32.39	0.86	0.7	54	28 ± 6	-46.04 ± 0.04	0.86 ± 0.11	single
23	245.5474175-50.0959979	16:22:11.38	-50:05:45.59	1.08	0.82	150	36 ± 7	-44.09 ± 0.01	1.22 ± 0.03	single
25	245.5167915-50.108572	16:22:4.030	-50:06:30.86	0.76	0.62	174	28 ± 6	-47.89 ± 0.05	1.24 ± 0.21	single
26	245.535353-50.1041745	16:22:8.480	-50:06:15.03	0.95	0.75	148	38 ± 8	-47.69 ± 0.11	–	complex
28	245.5508287-50.0914106	16:22:12.20	-50:05:29.08	1.34	0.9	169	32 ± 6	-45.93 ± 0.04	1.05 ± 0.16	single
29	245.5475066-50.0997527	16:22:11.40	-50:05:59.11	0.95	0.84	19	37 ± 7	-50.1 ± 0.06	0.98 ± 0.21	single
30	245.5475313-50.0989706	16:22:11.41	-50:05:56.29	1.68	1.32	117	38 ± 8	-49.63 ± 0.02	–	complex
31	245.547985-50.0993306	16:22:11.52	-50:05:57.59	0.97	0.91	95	37 ± 8	-49.78 ± 0.04	–	complex
33	245.5496874-50.0921633	16:22:11.92	-50:05:31.79	1.7	1.11	168	31 ± 6	-47.01 ± 0.03	1.02 ± 0.08	single
35	245.5174577-50.1082967	16:22:4.190	-50:06:29.87	0.96	0.82	129	28 ± 6	-48.53 ± 0.02	1.1 ± 0.07	single
37	245.530804-50.1034521	16:22:7.390	-50:06:12.43	1.29	1.16	132	34 ± 7	-49.7 ± 0.05	–	complex
43	245.5223011-50.1105471	16:22:5.350	-50:06:37.97	0.81	0.69	113	25 ± 5	–	–	–
44	245.5165096-50.1098853	16:22:3.960	-50:06:35.59	1.57	1.26	44	27 ± 6	–	–	–
45	245.549303-50.0984873	16:22:11.83	-50:05:54.55	1.45	1.03	48	35 ± 7	-49.0 ± 0.01	1.19 ± 0.05	single
46	245.5530669-50.0886225	16:22:12.74	-50:05:19.04	1.24	1.08	42	28 ± 6	-47.58 ± 0.07	1.1 ± 0.29	single
47	245.5496272-50.0988558	16:22:11.91	-50:05:55.88	1.06	1.0	26	35 ± 7	-49.75 ± 0.02	1.32 ± 0.09	single
49	245.5471944-50.0982171	16:22:11.33	-50:05:53.58	1.33	0.94	38	37 ± 8	-46.03 ± 0.02	1.41 ± 0.07	single
61	245.551584-50.0920068	16:22:12.38	-50:05:31.22	1.23	1.03	3	32 ± 6	-46.71 ± 0.07	0.89 ± 0.19	single
63	245.5332111-50.0860966	16:22:7.970	-50:05:9.950	1.86	1.14	92	24 ± 5	-39.83 ± 0.05	1.25 ± 0.18	single
65	245.5394054-50.1081881	16:22:9.460	-50:06:29.48	1.17	0.9	113	35 ± 7	–	–	–
66	245.5292379-50.1060849	16:22:7.020	-50:06:21.91	1.06	0.67	80	31 ± 6	-49.46 ± 0.02	1.24 ± 0.06	single
71	245.5554581-50.1093706	16:22:13.31	-50:06:33.73	1.52	1.21	45	26 ± 5	–	–	–
74	245.526505-50.0998535	16:22:6.360	-50:05:59.47	1.11	0.9	159	30 ± 6	-46.71 ± 0.02	0.95 ± 0.1	single
76	245.5321185-50.1024642	16:22:7.710	-50:06:8.870	0.86	0.7	20	36 ± 7	-49.77 ± 0.01	1.51 ± 0.04	single
77	245.509509-50.108116	16:22:2.280	-50:06:29.22	0.78	0.57	18	22 ± 4	–	–	–
80	245.5338592-50.1044306	16:22:8.130	-50:06:15.95	1.47	1.15	59	36 ± 7	-48.01 ± 0.01	1.12 ± 0.04	single
81	245.5157057-50.1118428	16:22:3.770	-50:06:42.63	1.42	1.16	106	25 ± 5	–	–	–
84	245.5171073-50.1084609	16:22:4.110	-50:06:30.46	0.95	0.67	159	28 ± 6	-48.05 ± 0.03	0.97 ± 0.08	single
85	245.514463-50.1066733	16:22:3.470	-50:06:24.02	1.27	1.18	97	23 ± 5	–	–	–
88	245.5487618-50.1045099	16:22:11.70	-50:06:16.24	0.94	0.78	17	36 ± 7	–	–	–
90	245.533779-50.1030615	16:22:8.110	-50:06:11.02	0.96	0.8	173	36 ± 7	–	–	–
91	245.5563744-50.1099885	16:22:13.53	-50:06:35.96	1.05	0.8	42	25 ± 5	–	–	–
94	245.5546166-50.1076554	16:22:13.11	-50:06:27.56	1.17	1.08	49	25 ± 5	–	–	–
98	245.5313456-50.1018072	16:22:7.520	-50:06:6.510	0.83	0.73	68	35 ± 7	-47.83 ± 0.02	1.57 ± 0.08	single
99	245.5583826-50.1029587	16:22:14.01	-50:06:10.65	0.85	0.82	18	23 ± 5	–	–	–
101	245.5267009-50.1004679	16:22:6.410	-50:06:1.680	1.52	1.14	39	30 ± 6	–	–	–
103	245.5326259-50.0866914	16:22:7.830	-50:05:12.09	0.8	0.7	68	24 ± 5	–	–	–
104	245.535577-50.1053101	16:22:8.540	-50:06:19.12	0.93	0.8	178	36 ± 7	-48.39 ± 0.06	–	complex
108	245.5246254-50.103576	16:22:5.910	-50:06:12.87	1.71	1.39	46	29 ± 6	-48.41 ± 0.04	0.8 ± 0.1	single
116	245.526364-50.1034004	16:22:6.330	-50:06:12.24	1.24	0.99	78	30 ± 6	-49.36 ± 0.05	1.14 ± 0.2	single

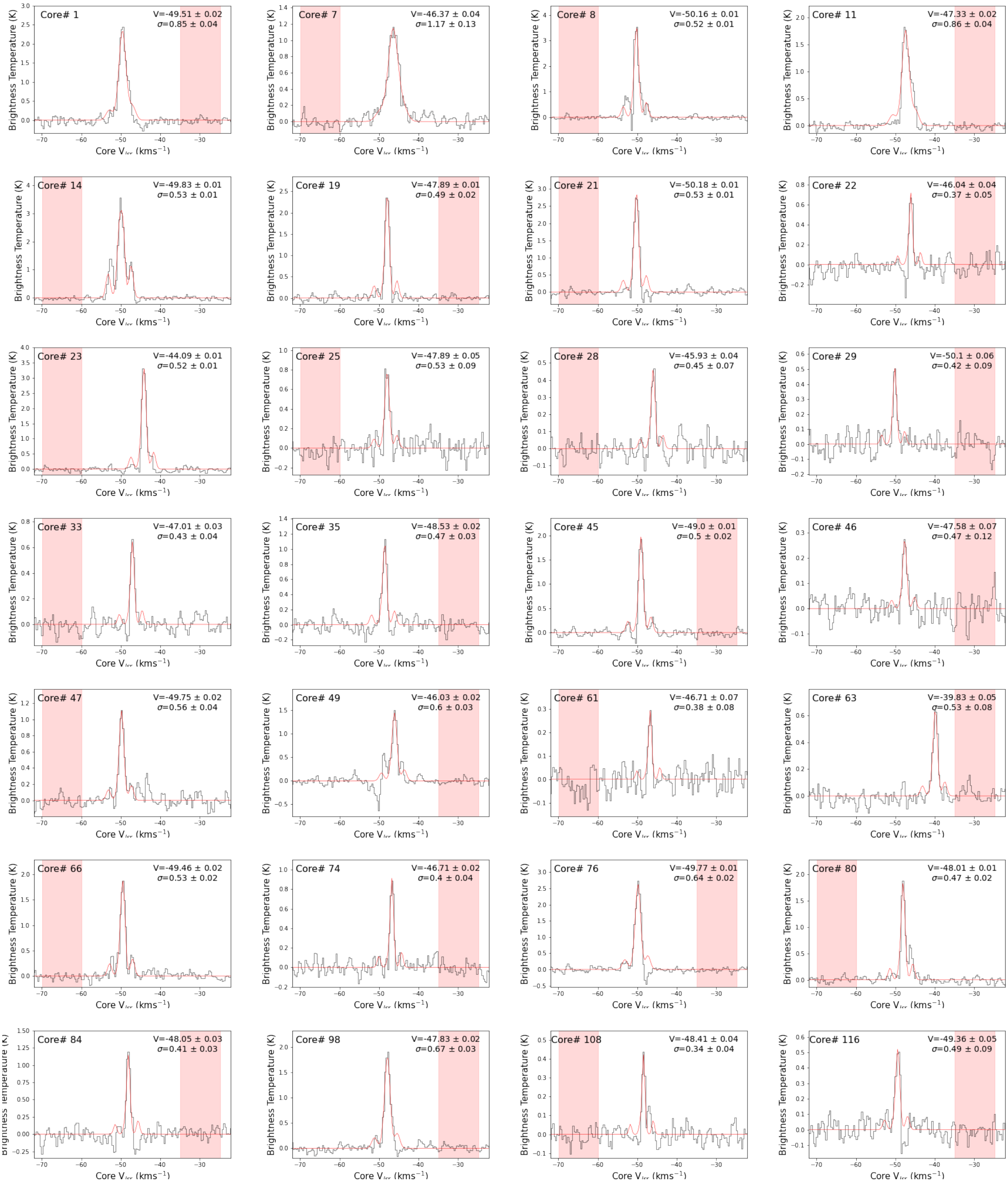

Fig. F.13. Single-type core-averaged, background-subtracted DCN spectra extracted from the cores in the evolved protocluster G333.60. See Table F.8 for the line fit parameters extracted for each core.

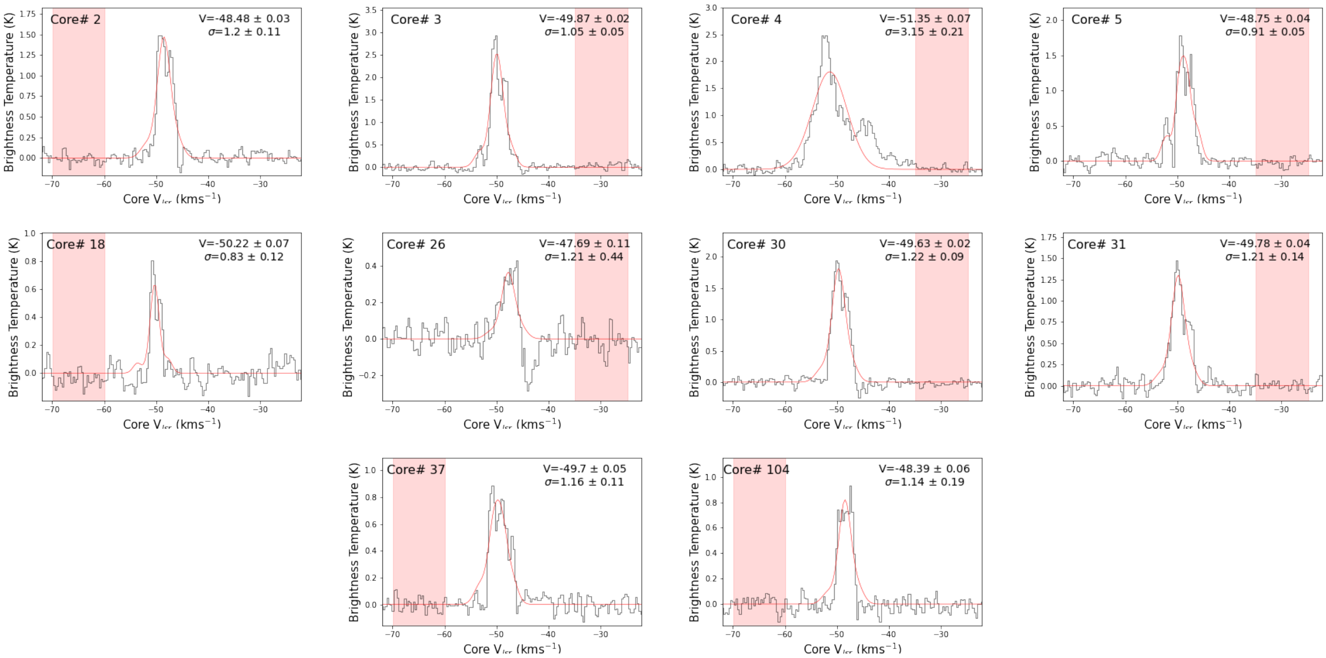

Fig. F.14. Complex-type core-averaged, background-subtracted DCN spectra extracted from the cores in the evolved protocluster G333.60. See Table F.8 for the line fit parameters extracted for each core.

Table F.9. DCN fits towards the core population of the intermediate protocluster G351.77.

n	Core Name	RA [ICRS]	DEC [ICRS]	F_A [″]	F_B [″]	PA [deg]	T [K]	$V_{\rm LSR}$ [km s^{-1}]	Linewidth [km s^{-1}]	Spectral Type
1	261.677251-36.1547987	17:26:42.54	-36:09:17.28	2.4	1.79	91	100 ± 50	-2.44 ± 0.04	–	complex
2	261.6767723-36.1551725	17:26:42.43	-36:09:18.62	2.88	2.22	126	100 ± 50	-1.96 ± 0.03	–	complex
4	261.6761591-36.1549329	17:26:42.28	-36:09:17.76	1.62	1.33	78	35 ± 10	-1.06 ± 0.02	–	complex
5	261.6783746-36.1556996	17:26:42.81	-36:09:20.52	1.56	1.46	122	100 ± 50	-4.84 ± 0.04	–	complex
6	261.6778603-36.1551246	17:26:42.69	-36:09:18.45	2.3	2.05	45	35 ± 10	-3.02 ± 0.05	–	complex
7	261.6788098-36.1553482	17:26:42.91	-36:09:19.25	1.84	1.72	99	38 ± 8	-4.51 ± 0.1	–	complex
8	261.67848-36.1431525	17:26:42.84	-36:08:35.35	1.42	1.28	61	29 ± 6	–	–	–
10	261.6882344-36.1502759	17:26:45.18	-36:09:0.990	1.76	1.51	149	26 ± 5	–	–	–
11	261.6753281-36.1587854	17:26:42.08	-36:09:31.63	1.88	1.62	84	33 ± 7	-0.73 ± 0.06	1.32 ± 0.21	single
12	261.6743392-36.1526192	17:26:41.84	-36:09:9.430	1.76	1.55	111	37 ± 8	-2.42 ± 0.02	0.89 ± 0.07	single
13	261.6878699-36.1553934	17:26:45.09	-36:09:19.42	1.64	1.48	155	29 ± 6	–	–	–
14	261.6800995-36.1544281	17:26:43.22	-36:09:15.94	2.04	1.68	92	38 ± 8	-4.0 ± 0.02	–	complex
15	261.6757897-36.1570022	17:26:42.19	-36:09:25.21	1.97	1.67	141	36 ± 7	0.37 ± 0.18	–	complex
16	261.6734791-36.1466672	17:26:41.63	-36:08:48.00	1.78	1.68	153	30 ± 6	–	–	–
18	261.6780185-36.1506715	17:26:42.72	-36:09:2.420	1.95	1.68	82	35 ± 7	-5.73 ± 0.12	1.83 ± 0.3	single
19	261.6820301-36.1518086	17:26:43.69	-36:09:6.510	1.95	1.72	65	33 ± 7	–	–	–
20	261.6784625-36.153325	17:26:42.83	-36:09:11.97	2.05	1.42	180	39 ± 8	-6.69 ± 0.01	1.59 ± 0.06	single
23	261.6833811-36.1544942	17:26:44.01	-36:09:16.18	1.99	1.73	88	34 ± 7	-4.6 ± 0.08	–	complex

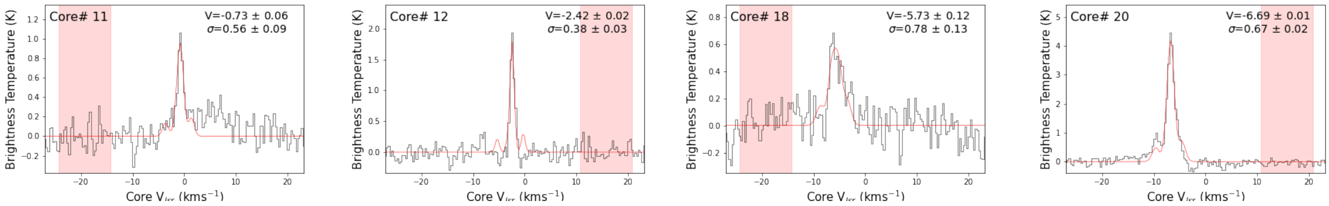

Fig. F.15. Single-type core-averaged, background-subtracted DCN spectra extracted from the cores in the intermediate protocluster G351.77. See Table F.9 for the line fit parameters for each core.

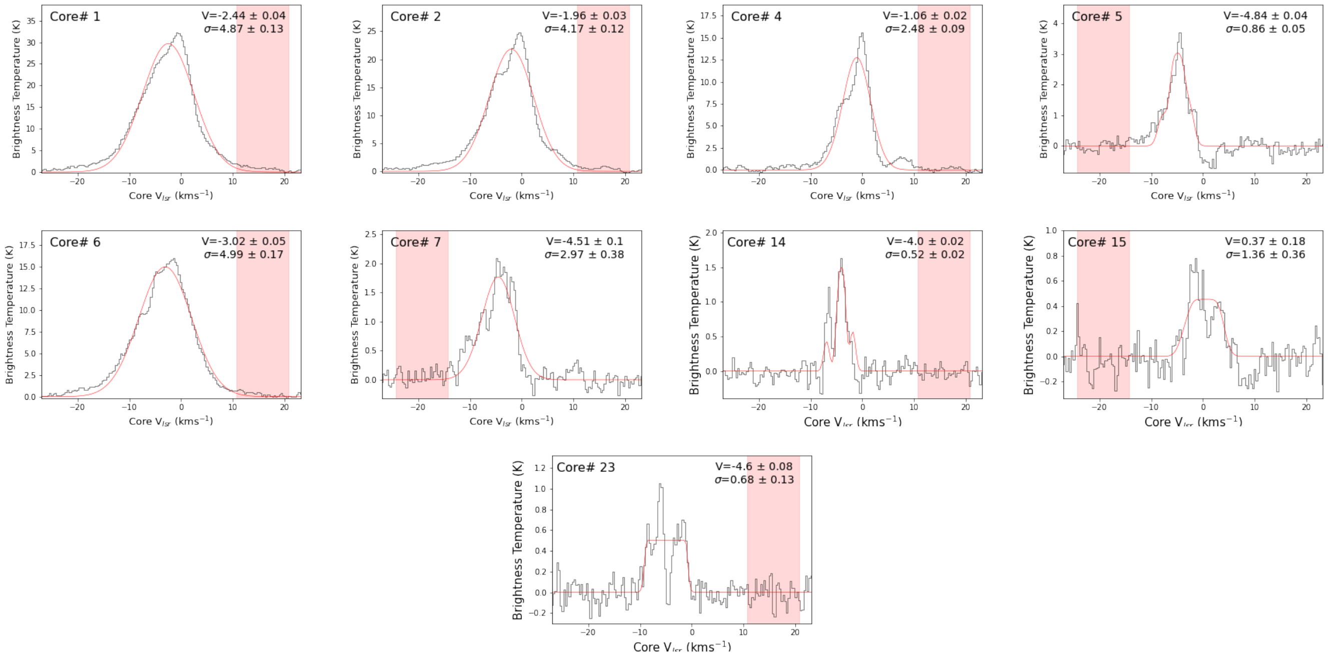

Fig. F.16. Complex-type core-averaged, background-subtracted DCN spectra extracted from the cores in the intermediate protocluster G351.77. See Table F.9 for the line fit parameters for each core.

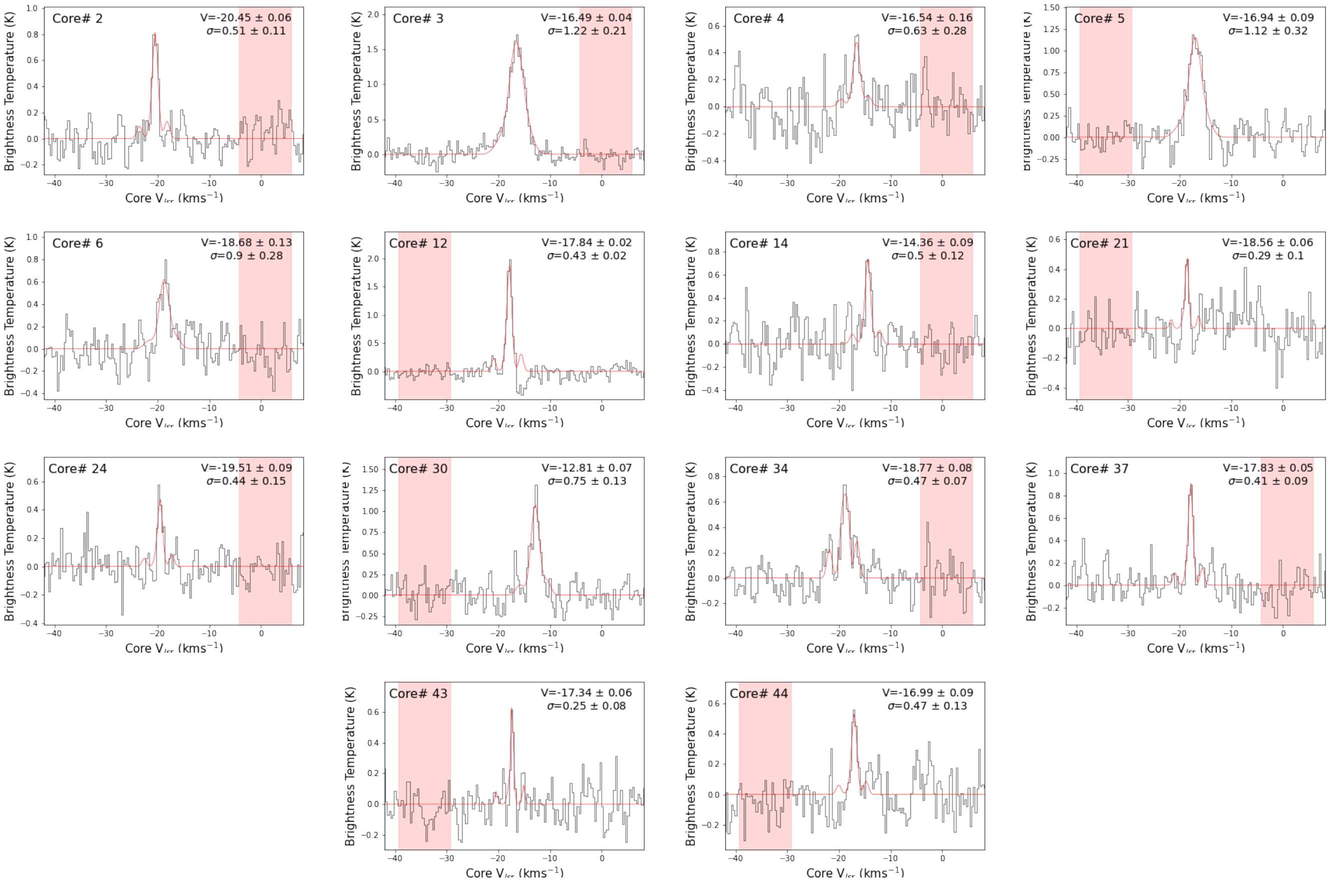

Fig. F.17. Single-type core-averaged, background-subtracted DCN spectra extracted from the cores in the intermediate protocluster G353.41. See Table F.10 for the line fit parameters for each core.

Table F.10. DCN fits towards the core population of the intermediate protocluster G353.41.

n	Core Name	RA [ICRS]	DEC [ICRS]	F_A [$''$]	F_B [$''$]	PA [deg]	T [K]	$V_{\rm LSR}$ [km s^{-1}]	Linewidth [km s^{-1}]	Spectral Type
2	262.6165032-34.6955865	17:30:27.96	-34:41:44.11	1.98	1.59	64	25 ± 5	-20.45 ± 0.06	1.2 ± 0.25	single
3	262.6184156-34.696524	17:30:28.42	-34:41:47.49	2.59	1.79	146	100 ± 50	-16.49 ± 0.04	2.86 ± 0.5	single
4	262.6103159-34.6932659	17:30:26.48	-34:41:35.76	1.56	1.46	104	31 ± 6	-16.54 ± 0.16	1.47 ± 0.66	single
5	262.6101515-34.6960014	17:30:26.44	-34:41:45.61	2.03	1.75	79	30 ± 6	-16.94 ± 0.09	2.63 ± 0.75	single
6	262.6049155-34.6934384	17:30:25.18	-34:41:36.38	1.6	1.48	129	27 ± 5	-18.68 ± 0.13	2.13 ± 0.65	single
7	262.6137738-34.6947298	17:30:27.31	-34:41:41.03	1.63	1.28	81	26 ± 5	–	–	–
8	262.6039531-34.6936374	17:30:24.95	-34:41:37.09	2.26	1.57	97	26 ± 5	–	–	–
9	262.6192359-34.690365	17:30:28.62	-34:41:25.31	2.71	1.93	62	26 ± 5	–	–	–
11	262.6243189-34.688078	17:30:29.84	-34:41:17.08	2.16	1.95	171	29 ± 6	–	–	–
12	262.6072148-34.6969795	17:30:25.73	-34:41:49.13	2.98	2.02	86	28 ± 6	-17.84 ± 0.02	1.02 ± 0.06	single
13	262.6078228-34.6996836	17:30:25.88	-34:41:58.86	1.91	1.47	154	26 ± 5	–	–	–
14	262.6147937-34.6946762	17:30:27.55	-34:41:40.83	2.0	1.58	124	26 ± 5	-14.36 ± 0.09	1.18 ± 0.29	single
15	262.6107433-34.6964412	17:30:26.58	-34:41:47.19	1.96	1.59	94	28 ± 6	-14.79 ± 0.09	–	complex
16	262.6215941-34.6989408	17:30:29.18	-34:41:56.19	2.7	2.5	19	22 ± 5	–	–	–
17	262.5954514-34.6916168	17:30:22.91	-34:41:29.82	1.57	1.43	88	19 ± 4	–	–	–
18	262.5927434-34.7052494	17:30:22.26	-34:42:18.90	1.95	1.53	90	18 ± 4	–	–	–
19	262.6064012-34.7019756	17:30:25.54	-34:42:7.110	1.55	1.2	58	24 ± 5	–	–	–
20	262.6111096-34.6932787	17:30:26.67	-34:41:35.80	1.66	1.62	178	29 ± 6	–	–	–
21	262.613191-34.6939495	17:30:27.17	-34:41:38.22	2.1	1.48	108	26 ± 5	-18.56 ± 0.06	0.69 ± 0.23	single
22	262.6118441-34.694615	17:30:26.84	-34:41:40.61	1.89	1.6	97	28 ± 6	–	–	–
23	262.6028175-34.6925438	17:30:24.68	-34:41:33.16	1.84	1.31	113	24 ± 5	–	–	–
24	262.6198349-34.6960383	17:30:28.76	-34:41:45.74	1.88	1.72	76	24 ± 5	-19.51 ± 0.09	1.03 ± 0.35	single
25	262.6155222-34.6952591	17:30:27.73	-34:41:42.93	1.88	1.2	137	25 ± 5	–	–	–
26	262.6143434-34.6917027	17:30:27.44	-34:41:30.13	1.62	1.35	110	25 ± 5	–	–	–
27	262.6000802-34.6910324	17:30:24.02	-34:41:27.72	3.39	2.5	48	22 ± 4	–	–	–
28	262.6253977-34.6999713	17:30:30.10	-34:41:59.90	2.53	1.88	38	20 ± 4	–	–	–
29	262.6133074-34.6919187	17:30:27.19	-34:41:30.91	1.7	1.32	79	25 ± 5	–	–	–
30	262.6114686-34.6962602	17:30:26.75	-34:41:46.54	1.52	1.41	31	27 ± 6	-12.81 ± 0.07	1.77 ± 0.3	single
31	262.6096651-34.692568	17:30:26.32	-34:41:33.24	1.71	1.33	119	30 ± 6	–	–	–
32	262.6094126-34.6910985	17:30:26.26	-34:41:27.95	3.31	2.99	43	28 ± 6	–	–	–
33	262.6287106-34.6862068	17:30:30.89	-34:41:10.34	2.41	2.0	24	24 ± 5	–	–	–
34	262.5982914-34.6919006	17:30:23.59	-34:41:30.84	1.81	1.36	139	22 ± 5	-18.77 ± 0.08	1.1 ± 0.16	single
35	262.6142011-34.6940134	17:30:27.41	-34:41:38.45	2.32	1.82	111	25 ± 5	–	–	–
36	262.6202758-34.7001995	17:30:28.87	-34:42:0.720	2.29	1.87	92	23 ± 5	–	–	–
37	262.6010398-34.6950114	17:30:24.25	-34:41:42.04	1.74	1.33	75	25 ± 5	-17.83 ± 0.05	0.97 ± 0.21	single
38	262.5971034-34.6920396	17:30:23.30	-34:41:31.34	2.01	1.6	105	21 ± 4	–	–	–
39	262.6054437-34.6963773	17:30:25.31	-34:41:46.96	2.03	1.88	159	29 ± 6	–	–	–
40	262.5917454-34.6897316	17:30:22.02	-34:41:23.03	1.87	1.47	96	18 ± 4	–	–	–
41	262.6095777-34.6983259	17:30:26.30	-34:41:53.97	2.24	1.83	72	26 ± 5	–	–	–
42	262.5975992-34.6876666	17:30:23.42	-34:41:15.60	2.01	1.14	21	18 ± 4	–	–	–
43	262.6035166-34.6966807	17:30:24.84	-34:41:48.05	2.48	1.78	95	27 ± 5	-17.34 ± 0.06	0.59 ± 0.19	single
44	262.6030115-34.6956424	17:30:24.72	-34:41:44.31	1.76	1.55	97	27 ± 5	-17.0 ± 0.09	1.1 ± 0.31	single
45	262.6143008-34.6909376	17:30:27.43	-34:41:27.38	4.09	3.38	67	25 ± 5	–	–	–
46	262.6187648-34.6912377	17:30:28.50	-34:41:28.46	2.76	2.12	53	25 ± 5	–	–	–
47	262.6178453-34.6919943	17:30:28.28	-34:41:31.18	3.17	2.9	168	25 ± 5	–	–	–

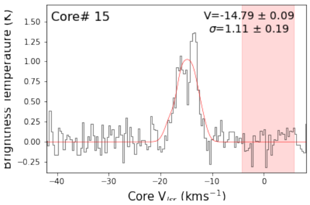

Fig. F.18. Complex-type core-averaged, background-subtracted DCN spectra extracted from the cores in the intermediate protocluster G353.41. See Table F.10 for the line fit parameters for each core.

Table F.11. DCN fits towards the core population of the young protocluster W43-MM1.

n	Core Name	RA [ICRS]	DEC [ICRS]	F_A [″]	F_B [″]	PA [deg]	T [K]	$V_{\rm LSR}$ [km s^{-1}]	Linewidth [km s^{-1}]	Spectral Type
1	281.9459334-1.9074736	18:47:47.02	-01:54:26.90	0.71	0.62	88	100 ± 50	102.22 ± 0.31	–	complex
2	281.9451648-1.9081343	18:47:46.84	-01:54:29.28	0.61	0.56	143	100 ± 50	96.01 ± 0.04	–	complex
3	281.9432069-1.9092736	18:47:46.37	-01:54:33.38	0.72	0.63	37	100 ± 50	96.9 ± 0.08	–	complex
4	281.945748-1.9073463	18:47:46.98	-01:54:26.45	0.82	0.77	62	100 ± 50	103.56 ± 0.36	–	complex
5	281.9469228-1.908243	18:47:47.26	-01:54:29.67	0.65	0.49	96	18 ± 4	99.13 ± 0.07	1.33 ± 0.34	single
6	281.9423152-1.909246	18:47:46.16	-01:54:33.29	0.7	0.54	104	22 ± 4	–	–	–
7	281.9438998-1.9064175	18:47:46.54	-01:54:23.10	0.72	0.5	101	100 ± 50	95.99 ± 0.02	0.73 ± 0.05	single
8	281.938703-1.9102889	18:47:45.29	-01:54:37.04	0.6	0.49	99	21 ± 4	–	–	–
9	281.9448606-1.9086666	18:47:46.77	-01:54:31.20	0.66	0.54	67	100 ± 50	95.9 ± 0.13	–	complex
10	281.9458236-1.9071389	18:47:47.00	-01:54:25.70	0.93	0.86	131	35 ± 10	102.92 ± 0.25	–	complex
11	281.9365573-1.9125569	18:47:44.77	-01:54:45.20	0.69	0.58	101	100 ± 50	94.74 ± 0.05	2.49 ± 0.95	single
12	281.9436641-1.9090461	18:47:46.48	-01:54:32.57	0.65	0.54	91	100 ± 50	95.0 ± 0.14	–	complex
13	281.9427046-1.9092745	18:47:46.25	-01:54:33.39	0.69	0.55	132	22 ± 4	94.52 ± 0.07	–	complex
14	281.944974-1.9044595	18:47:46.79	-01:54:16.05	0.6	0.47	97	100 ± 50	–	–	–
15	281.9438148-1.9067276	18:47:46.52	-01:54:24.22	0.66	0.51	96	100 ± 50	93.98 ± 0.04	–	complex
16	281.9372707-1.9118969	18:47:44.94	-01:54:42.83	0.66	0.54	134	21 ± 4	–	–	–
17	281.9454215-1.9083192	18:47:46.90	-01:54:29.95	0.78	0.67	121	100 ± 50	–	–	–
18	281.9462451-1.9075171	18:47:47.10	-01:54:27.06	0.64	0.57	92	35 ± 10	99.79 ± 0.1	–	complex
20	281.9456983-1.9036124	18:47:46.97	-01:54:13.00	1.07	0.95	39	21 ± 4	–	–	–
21	281.9453834-1.9082357	18:47:46.89	-01:54:29.65	0.74	0.58	121	35 ± 10	–	–	–
22	281.9384338-1.9107821	18:47:45.22	-01:54:38.82	0.6	0.51	122	21 ± 4	–	–	–
23	281.9452927-1.9040458	18:47:46.87	-01:54:14.56	0.57	0.45	86	21 ± 4	–	–	–
24	281.9440629-1.9089	18:47:46.58	-01:54:32.04	0.69	0.49	82	22 ± 5	–	–	–
25	281.9459111-1.9085541	18:47:47.02	-01:54:30.79	0.78	0.6	146	100 ± 50	98.37 ± 0.04	1.39 ± 0.13	single
26	281.94313-1.9081925	18:47:46.35	-01:54:29.49	0.62	0.57	105	23 ± 5	–	–	–
27	281.9472105-1.9035597	18:47:47.33	-01:54:12.81	0.62	0.55	102	20 ± 4	–	–	–
28	281.9453005-1.9071369	18:47:46.87	-01:54:25.69	0.57	0.52	133	100 ± 50	99.91 ± 0.33	–	complex
29	281.9460739-1.9089351	18:47:47.06	-01:54:32.17	0.54	0.44	115	19 ± 4	–	–	–
30	281.9456971-1.9082389	18:47:46.97	-01:54:29.66	0.63	0.47	97	25 ± 5	–	–	–
31	281.9337243-1.9135618	18:47:44.09	-01:54:48.82	0.65	0.57	18	21 ± 4	–	–	–
32	281.9455609-1.9075139	18:47:46.93	-01:54:27.05	0.71	0.56	99	35 ± 10	103.86 ± 0.14	–	complex
33	281.9438197-1.9079708	18:47:46.52	-01:54:28.69	0.68	0.56	73	23 ± 5	97.55 ± 0.02	0.87 ± 0.07	single
34	281.9358647-1.9117019	18:47:44.61	-01:54:42.13	0.57	0.49	88	21 ± 4	96.08 ± 0.05	–	complex
35	281.9385991-1.9110901	18:47:45.26	-01:54:39.92	0.95	0.66	124	21 ± 4	–	–	–
36	281.9443508-1.9053944	18:47:46.64	-01:54:19.42	0.55	0.53	72	24 ± 5	–	–	–
37	281.9454183-1.9067383	18:47:46.90	-01:54:24.26	0.68	0.48	109	100 ± 50	101.59 ± 0.02	0.79 ± 0.05	single
38	281.9507008-1.9010492	18:47:48.17	-01:54:3.780	0.96	0.68	123	18 ± 4	–	–	–
39	281.9365275-1.9129829	18:47:44.77	-01:54:46.74	0.76	0.58	116	21 ± 4	96.97 ± 0.05	0.68 ± 0.15	single
40	281.9440532-1.9057986	18:47:46.57	-01:54:20.87	0.86	0.64	40	25 ± 5	95.79 ± 0.04	0.48 ± 0.1	single
41	281.945843-1.9046555	18:47:47.00	-01:54:16.76	0.59	0.46	104	21 ± 4	–	–	–
42	281.9455026-1.9079514	18:47:46.92	-01:54:28.63	0.64	0.38	104	26 ± 5	98.68 ± 0.08	–	complex
43	281.9558069-1.9010298	18:47:49.39	-01:54:3.710	0.76	0.69	28	20 ± 4	–	–	–
44	281.9465996-1.9059703	18:47:47.18	-01:54:21.49	0.56	0.54	153	20 ± 4	–	–	–
45	281.9446978-1.9048517	18:47:46.73	-01:54:17.47	0.62	0.44	92	22 ± 5	–	–	–
46	281.9473216-1.9037125	18:47:47.36	-01:54:13.36	0.57	0.54	120	20 ± 4	–	–	–
47	281.9350259-1.9116027	18:47:44.41	-01:54:41.77	0.79	0.44	71	21 ± 4	–	–	–
48	281.9377497-1.9116788	18:47:45.06	-01:54:42.04	0.68	0.45	74	21 ± 4	–	–	–
49	281.9408041-1.9090791	18:47:45.79	-01:54:32.68	0.69	0.52	89	21 ± 4	–	–	–
50	281.9494405-1.8997773	18:47:47.87	-01:53:59.20	0.91	0.67	176	18 ± 4	–	–	–
51	281.938249-1.9109571	18:47:45.18	-01:54:39.45	0.66	0.55	85	21 ± 4	–	–	–
52	281.9365434-1.9122622	18:47:44.77	-01:54:44.14	0.65	0.52	92	22 ± 4	–	–	–
53	281.9457328-1.9089106	18:47:46.98	-01:54:32.08	0.6	0.42	97	20 ± 4	99.83 ± 0.06	0.79 ± 0.21	single
54	281.936822-1.9119242	18:47:44.84	-01:54:42.93	0.69	0.6	54	21 ± 4	–	–	–
55	281.9414962-1.9094029	18:47:45.96	-01:54:33.85	0.89	0.72	124	21 ± 4	–	–	–
56	281.9391449-1.9108264	18:47:45.39	-01:54:38.98	0.77	0.69	123	21 ± 4	–	–	–
58	281.9465409-1.9030795	18:47:47.17	-01:54:11.09	0.8	0.66	130	20 ± 4	–	–	–
59	281.9466558-1.9063105	18:47:47.20	-01:54:22.72	0.74	0.69	15	20 ± 4	97.32 ± 0.02	1.26 ± 0.08	single
60	281.9347438-1.9117236	18:47:44.34	-01:54:42.20	1.0	0.93	152	21 ± 4	–	–	–
61	281.9473742-1.9033061	18:47:47.37	-01:54:11.90	0.61	0.54	64	20 ± 4	–	–	–
62	281.9364851-1.9112375	18:47:44.76	-01:54:40.45	0.58	0.5	84	21 ± 4	–	–	–
63	281.9408778-1.9162621	18:47:45.81	-01:54:58.54	1.33	1.25	38	25 ± 5	–	–	–
64	281.9416193-1.9070122	18:47:45.99	-01:54:25.24	0.64	0.51	166	23 ± 5	–	–	–
66	281.9411991-1.9097694	18:47:45.89	-01:54:35.17	1.19	0.91	4	21 ± 4	–	–	–
67	281.9459087-1.9063496	18:47:47.02	-01:54:22.86	0.64	0.46	149	21 ± 4	101.17 ± 0.03	1.13 ± 0.11	single
68	281.9475634-1.907071	18:47:47.42	-01:54:25.46	1.07	0.77	23	19 ± 4	98.57 ± 0.05	1.14 ± 0.2	single

Table F.11. continued DCN fits towards the core population of the young protocluster W43-MM1.

n	Core Name	RA [ICRS]	DEC [ICRS]	F_A [″]	F_B [″]	PA [deg]	T [K]	$V_{\rm LSR}$ [km s^{-1}]	Linewidth [km s^{-1}]	Spectral Type
69	281.946263-1.9095657	18:47:47.10	-01:54:34.44	0.9	0.73	17	18 ± 4	97.8 ± 0.07	0.63 ± 0.26	single
70	281.9449909-1.9057425	18:47:46.80	-01:54:20.67	1.09	0.86	23	22 ± 5	101.7 ± 0.02	1.74 ± 0.25	single
73	281.9458121-1.905854	18:47:46.99	-01:54:21.07	0.66	0.53	143	20 ± 4	100.74 ± 0.02	0.83 ± 0.09	single
74	281.9432263-1.9058611	18:47:46.37	-01:54:21.10	0.82	0.65	161	25 ± 5	–	–	–
75	281.9437613-1.9073486	18:47:46.50	-01:54:26.45	0.82	0.61	129	25 ± 5	–	–	–

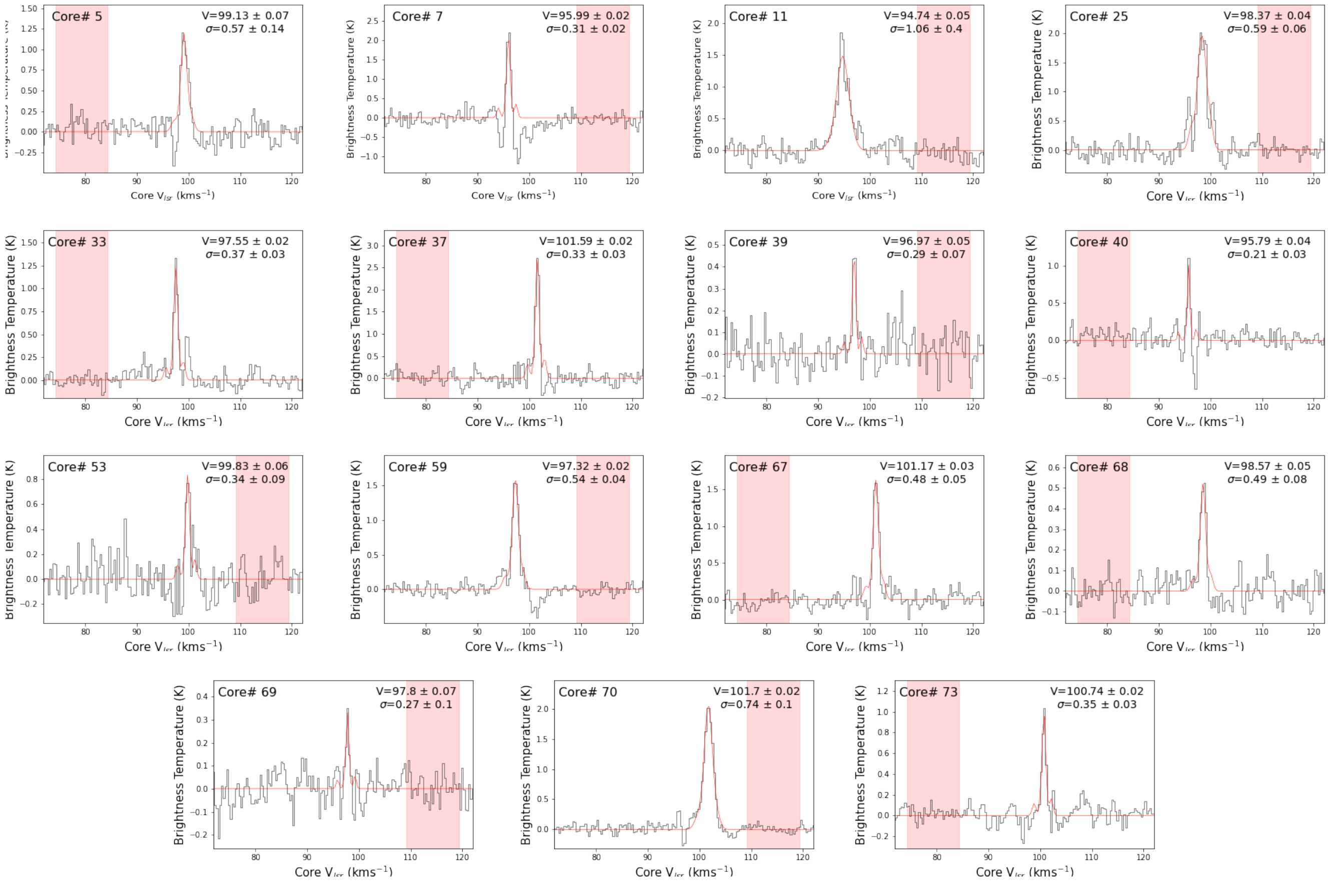

Fig. F.19. single-type core-averaged, background-subtracted DCN spectra extracted from the cores in the young protocluster W43-MM1. Readers can refer to Table F.11 for the line fit parameters for each core.

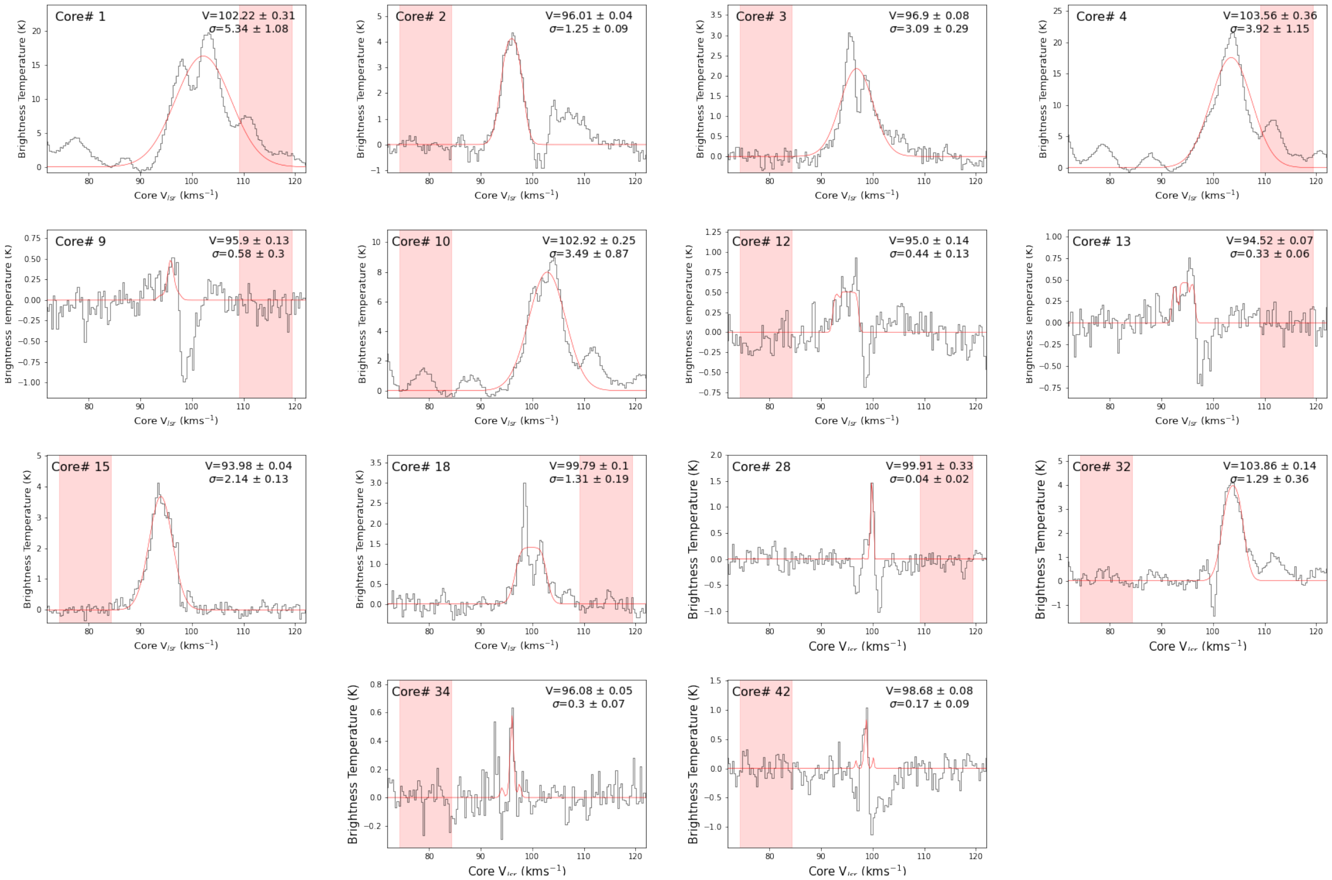

Fig. F.20. Complex-type core-averaged, background-subtracted DCN spectra extracted from the cores in the young protocluster W43-MM1. Readers can refer to Table F.11 for the line fit parameters for each core. labelfigf20

Table F.12. DCN fits towards the core population of the young protocluster W43-MM2.

n	Core Name	RA [ICRS]	DEC [ICRS]	F_A [″]	F_B [″]	PA [deg]	T [K]	$V_{\rm LSR}$ [km s^{-1}]	Linewidth [km s^{-1}]	Spectral Type
1	281.9033208-2.0150752	18:47:36.80	-02:00:54.27	0.76	0.7	147	100 ± 50	89.59 ± 0.08	–	complex
2	281.9001273-2.0224281	18:47:36.03	-02:01:20.74	0.78	0.48	84	19 ± 4	90.33 ± 0.07	1.25 ± 0.33	single
3	281.9004197-2.0210949	18:47:36.10	-02:01:15.94	0.9	0.7	80	18 ± 4	90.14 ± 0.06	2.21 ± 1.43	single
4	281.9006289-2.0132967	18:47:36.15	-02:00:47.87	0.59	0.52	64	18 ± 4	–	–	–
5	281.9011837-2.0141012	18:47:36.28	-02:00:50.76	0.67	0.54	175	19 ± 4	91.13 ± 0.03	2.11 ± 0.6	single
6	281.9031379-2.0149264	18:47:36.75	-02:00:53.74	0.79	0.73	56	35 ± 10	88.33 ± 0.03	–	complex
7	281.9029377-2.0132083	18:47:36.71	-02:00:47.55	0.72	0.55	118	100 ± 50	91.59 ± 0.02	1.84 ± 0.13	single
8	281.8962619-2.0191026	18:47:35.10	-02:01:8.770	0.64	0.55	128	18 ± 4	–	–	–
9	281.9034863-2.0173945	18:47:36.84	-02:01:2.620	0.74	0.54	132	20 ± 4	89.57 ± 0.03	1.47 ± 0.16	single
10	281.9135971-2.0078124	18:47:39.26	-02:00:28.12	0.79	0.74	148	23 ± 5	93.99 ± 0.09	–	complex
11	281.8987232-2.0090321	18:47:35.69	-02:00:32.52	0.62	0.49	148	21 ± 4	92.08 ± 0.02	1.42 ± 0.1	single
12	281.9027193-2.014794	18:47:36.65	-02:00:53.26	0.86	0.72	86	29 ± 6	91.32 ± 0.03	2.01 ± 0.58	single
13	281.9028491-2.0133518	18:47:36.68	-02:00:48.07	0.69	0.56	168	21 ± 4	91.49 ± 0.03	2.16 ± 0.41	single
14	281.9002537-2.0244012	18:47:36.06	-02:01:27.84	0.66	0.57	111	20 ± 4	–	–	–
15	281.9034339-2.0146926	18:47:36.82	-02:00:52.89	1.33	1.24	22	35 ± 10	88.08 ± 0.02	–	complex
16	281.9006053-2.0129566	18:47:36.15	-02:00:46.64	0.56	0.48	98	18 ± 4	–	–	–
17	281.9095872-2.011522	18:47:38.30	-02:00:41.48	0.57	0.48	104	18 ± 4	–	–	–
19	281.8998797-2.0139649	18:47:35.97	-02:00:50.27	1.46	1.2	1	18 ± 4	93.14 ± 0.07	1.34 ± 0.25	single
20	281.9031931-2.0153229	18:47:36.77	-02:00:55.16	0.72	0.69	110	35 ± 10	90.52 ± 0.05	–	complex
21	281.9005682-2.0247778	18:47:36.14	-02:01:29.20	0.62	0.62	48	20 ± 4	–	–	–
22	281.9034115-2.0140036	18:47:36.82	-02:00:50.41	0.6	0.54	154	24 ± 5	92.85 ± 0.03	0.8 ± 0.09	single
24	281.9031397-2.0154806	18:47:36.75	-02:00:55.73	0.71	0.61	107	30 ± 6	88.59 ± 0.02	1.29 ± 0.08	single
25	281.8945099-2.0177668	18:47:34.68	-02:01:3.960	0.73	0.57	108	19 ± 4	–	–	–
26	281.9038579-2.0152273	18:47:36.93	-02:00:54.82	0.94	0.74	83	27 ± 6	90.1 ± 0.02	–	complex
27	281.9003313-2.0203002	18:47:36.08	-02:01:13.08	0.51	0.47	74	18 ± 4	–	–	–
28	281.9031601-2.0129333	18:47:36.76	-02:00:46.56	0.77	0.65	80	21 ± 4	92.15 ± 0.03	1.0 ± 0.11	single
29	281.9000187-2.0137672	18:47:36.00	-02:00:49.56	0.78	0.62	80	18 ± 4	92.89 ± 0.1	1.12 ± 0.19	single
30	281.9001893-2.0207471	18:47:36.05	-02:01:14.69	0.78	0.68	136	18 ± 4	88.97 ± 0.1	1.17 ± 0.42	single
31	281.9020978-2.0195665	18:47:36.50	-02:01:10.44	1.53	0.97	82	18 ± 4	90.38 ± 0.07	0.86 ± 0.11	single
32	281.9001361-2.0137613	18:47:36.03	-02:00:49.54	0.77	0.54	97	18 ± 4	93.28 ± 0.04	2.05 ± 0.83	single
33	281.9028092-2.0166989	18:47:36.67	-02:01:0.120	0.69	0.52	92	21 ± 4	–	–	–
35	281.8969217-2.0171335	18:47:35.26	-02:01:1.680	0.58	0.5	140	18 ± 4	–	–	–
36	281.8949343-2.0222271	18:47:34.78	-02:01:20.02	1.03	0.75	78	19 ± 4	–	–	–
37	281.904921-2.0095957	18:47:37.18	-02:00:34.54	1.69	1.23	139	20 ± 4	–	–	–
38	281.9024073-2.0132046	18:47:36.58	-02:00:47.54	0.64	0.55	63	21 ± 4	–	–	–
39	281.9020797-2.0140221	18:47:36.50	-02:00:50.48	0.79	0.68	104	21 ± 4	90.3 ± 0.03	0.76 ± 0.13	single
40	281.8961141-2.0201944	18:47:35.07	-02:01:12.70	0.66	0.54	75	18 ± 4	–	–	–
44	281.9031339-2.0159252	18:47:36.75	-02:00:57.33	0.66	0.62	78	26 ± 5	88.68 ± 0.04	–	complex
46	281.911161-2.0123366	18:47:38.68	-02:00:44.41	0.8	0.43	132	18 ± 4	–	–	–
47	281.9015429-2.0234787	18:47:36.37	-02:01:24.52	1.52	1.07	110	20 ± 4	90.33 ± 0.05	0.61 ± 0.15	single

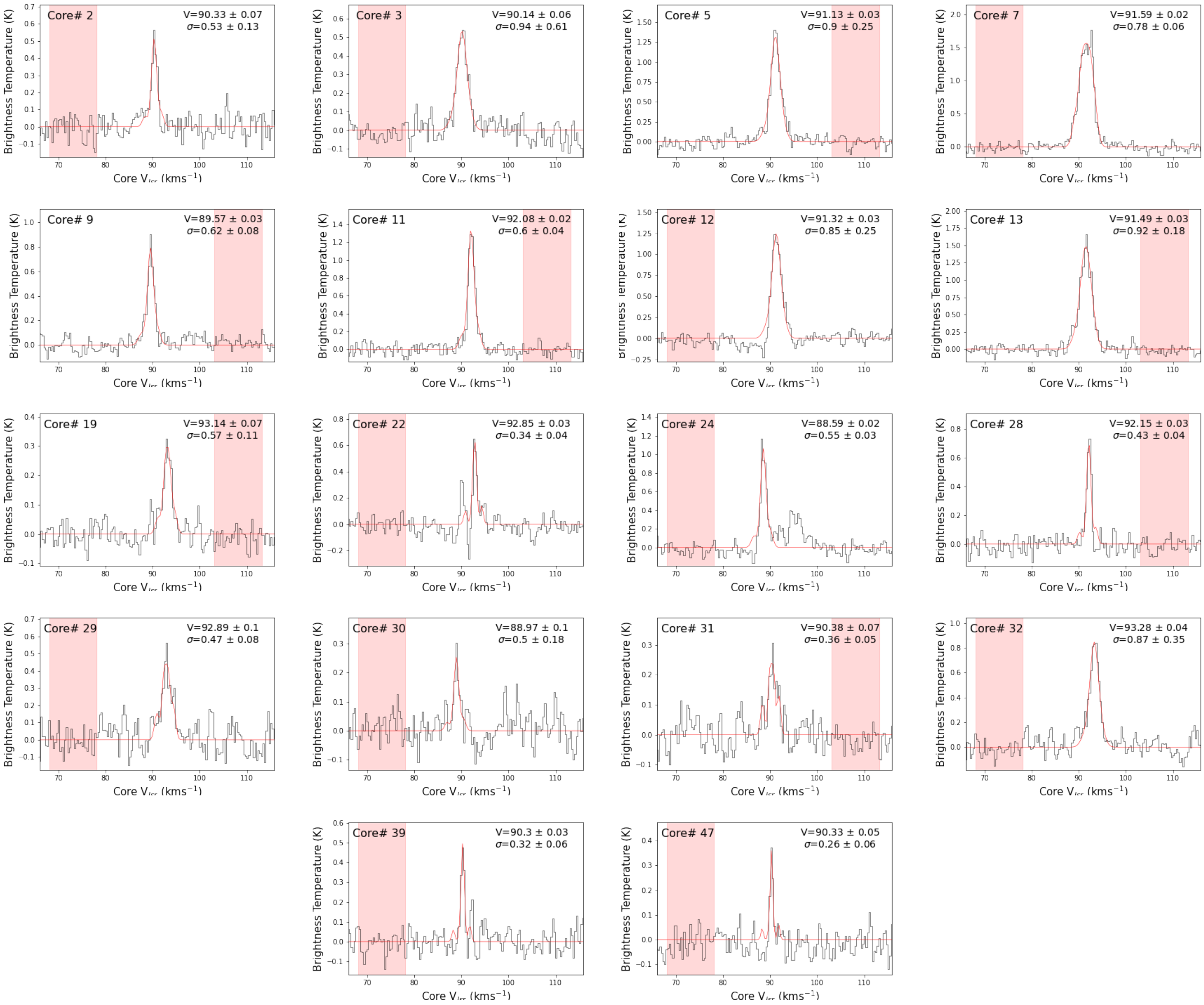

Fig. F.21. single-type core-averaged, background-subtracted DCN spectra extracted from the cores in the young protocluster W43-MM2. Readers can refer to Table F.12 for the line fit parameters for each core.

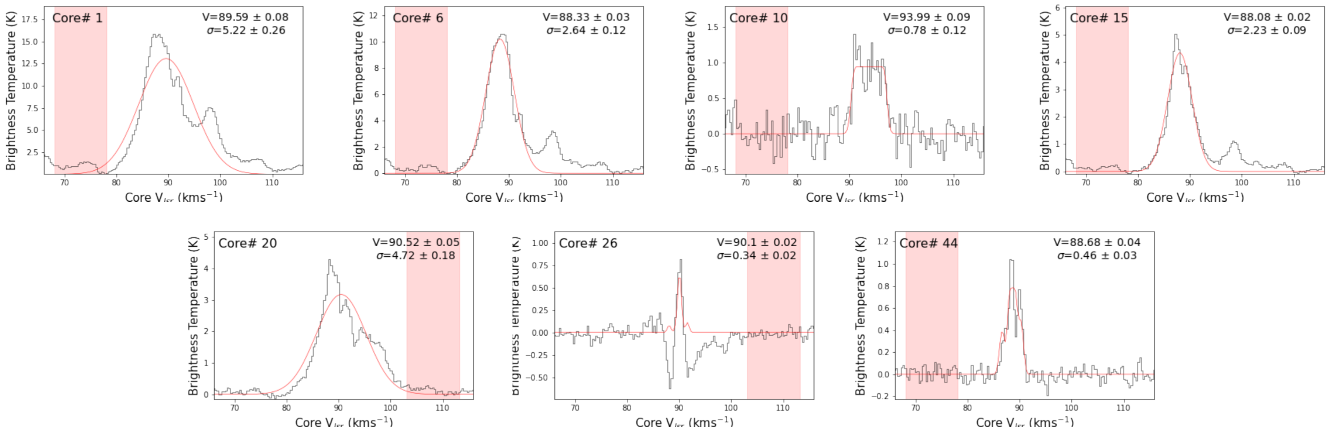

Fig. F.22. Complex-type core-averaged, background-subtracted DCN spectra extracted from the cores in the young protocluster W43-MM2. Readers can refer to Table F.12 for the line fit parameters for each core.

Table F.13. DCN fits towards the core population of the intermediate protocluster W43-MM3.

n	Core Name	RA [ICRS]	DEC [ICRS]	F_A [″]	F_B [″]	PA [deg]	T [K]	$V_{\rm LSR}$ [km s^{-1}]	Linewidth [km s^{-1}]	Spectral Type
1	281.9238036-2.0079434	18:47:41.71	-02:00:28.60	0.65	0.5	90	100 ± 50	92.46 ± 0.02	1.22 ± 0.09	single
2	281.9135958-2.0078027	18:47:39.26	-02:00:28.09	0.73	0.57	57	100 ± 50	93.38 ± 0.12	–	complex
3	281.9207197-2.0057611	18:47:40.97	-02:00:20.74	0.67	0.65	20	25 ± 5	–	–	–
4	281.9238914-2.0076105	18:47:41.73	-02:00:27.40	0.64	0.45	118	31 ± 6	95.3 ± 0.09	1.63 ± 0.73	single
5	281.9176265-2.0095864	18:47:40.23	-02:00:34.51	0.56	0.53	111	20 ± 4	–	–	–
6	281.9234345-2.007048	18:47:41.62	-02:00:25.37	0.64	0.61	44	32 ± 7	92.98 ± 0.07	1.11 ± 0.15	single
8	281.9145005-2.0091444	18:47:39.48	-02:00:32.92	0.55	0.47	82	22 ± 5	–	–	–
9	281.9232633-2.0078731	18:47:41.58	-02:00:28.34	0.55	0.46	88	29 ± 6	–	–	–
10	281.924284-2.008162	18:47:41.83	-02:00:29.38	0.82	0.62	98	29 ± 6	93.9 ± 0.05	–	complex
11	281.9273799-2.0015818	18:47:42.57	-02:00:5.690	1.1	0.94	52	22 ± 5	–	–	–
12	281.9249972-2.0078222	18:47:42.00	-02:00:28.16	0.63	0.51	81	28 ± 6	–	–	–
13	281.9134182-2.0075463	18:47:39.22	-02:00:27.17	1.09	0.93	158	26 ± 5	93.7 ± 0.11	–	complex
14	281.921711-2.00727	18:47:41.21	-02:00:26.17	0.73	0.64	82	25 ± 5	92.44 ± 0.03	0.96 ± 0.09	single
16	281.9244991-2.0077454	18:47:41.88	-02:00:27.88	0.81	0.76	110	30 ± 6	90.66 ± 0.01	1.4 ± 0.06	single
17	281.9293338-2.0006956	18:47:43.04	-02:00:2.500	1.05	0.66	92	20 ± 4	–	–	–
18	281.9209802-2.0087135	18:47:41.04	-02:00:31.37	0.81	0.69	89	23 ± 5	–	–	–
19	281.9215884-2.0111158	18:47:41.18	-02:00:40.02	1.15	1.12	64	21 ± 4	–	–	–
20	281.9191116-2.0101555	18:47:40.59	-02:00:36.56	1.19	1.04	140	21 ± 4	–	–	–
21	281.9199849-2.0102219	18:47:40.80	-02:00:36.80	0.77	0.72	99	21 ± 4	–	–	–
22	281.9189643-2.0061312	18:47:40.55	-02:00:22.07	1.05	0.73	176	22 ± 5	–	–	–
23	281.9268886-1.9949305	18:47:42.45	-01:59:41.75	0.59	0.5	114	21 ± 4	–	–	–
24	281.9139833-2.0079715	18:47:39.36	-02:00:28.70	1.1	0.75	140	25 ± 5	93.59 ± 0.14	–	complex
25	281.9207192-2.0087896	18:47:40.97	-02:00:31.64	0.76	0.64	59	22 ± 5	–	–	–
26	281.9174417-2.0007412	18:47:40.19	-02:00:2.670	0.64	0.4	14	21 ± 4	–	–	–
27	281.9317875-2.0140444	18:47:43.63	-02:00:50.56	1.0	0.79	119	18 ± 4	–	–	–
28	281.9138487-2.00915	18:47:39.32	-02:00:32.94	0.61	0.51	22	22 ± 5	–	–	–
29	281.9130975-2.0077682	18:47:39.14	-02:00:27.97	0.69	0.57	68	26 ± 5	–	–	–
31	281.9162905-2.0089111	18:47:39.91	-02:00:32.08	0.58	0.5	14	21 ± 4	94.97 ± 0.07	0.95 ± 0.15	single
32	281.9238534-2.0001514	18:47:41.72	-02:00:0.550	1.28	1.05	45	22 ± 4	–	–	–
34	281.9251055-2.0070496	18:47:42.03	-02:00:25.38	0.7	0.65	146	29 ± 6	91.92 ± 0.04	1.82 ± 0.45	single
36	281.9274195-1.9953527	18:47:42.58	-01:59:43.27	0.9	0.6	129	20 ± 4	–	–	–
37	281.9112287-2.0123947	18:47:38.69	-02:00:44.62	1.47	1.27	97	21 ± 4	–	–	–
38	281.9152398-2.0088625	18:47:39.66	-02:00:31.91	0.57	0.52	49	22 ± 4	–	–	–
39	281.9135666-2.0081333	18:47:39.26	-02:00:29.28	1.06	0.88	174	26 ± 5	92.88 ± 0.09	3.1 ± 1.13	single
40	281.9213102-2.0069861	18:47:41.11	-02:00:25.15	1.36	1.0	153	25 ± 5	91.73 ± 0.03	0.67 ± 0.13	single
42	281.9311334-2.005116	18:47:43.47	-02:00:18.42	1.17	0.88	119	21 ± 4	–	–	–

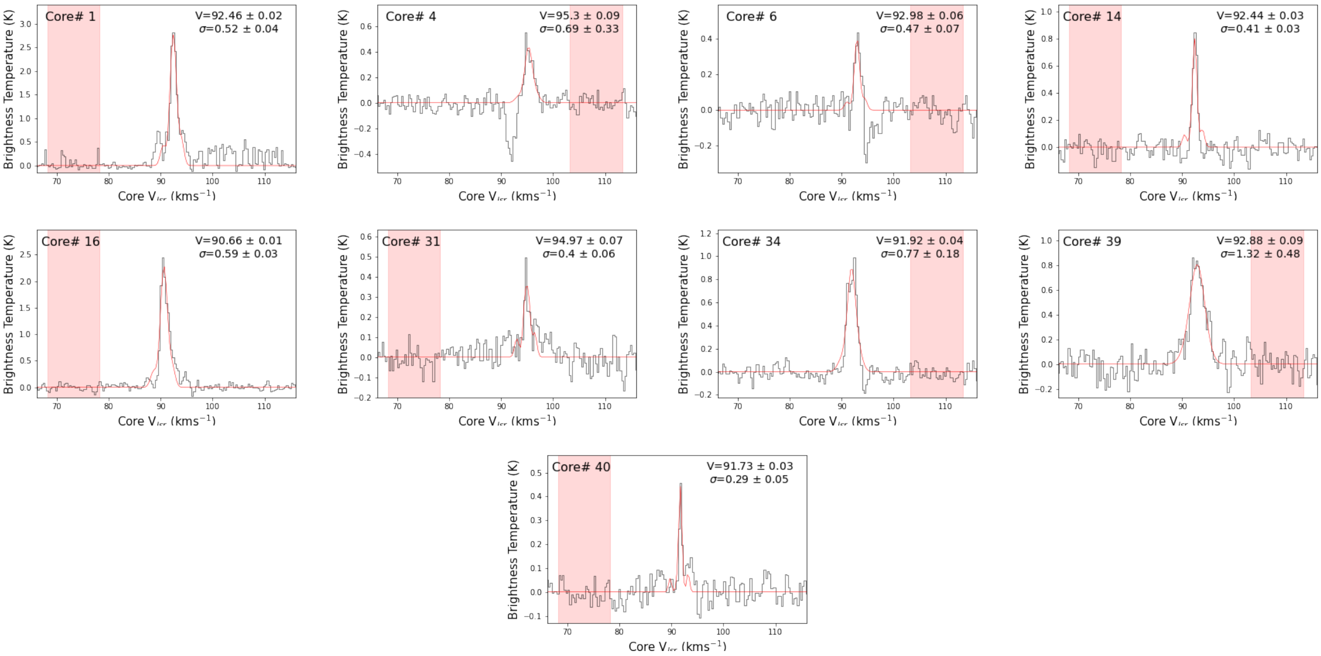

Fig. F.23. Single-type core-averaged, background-subtracted DCN spectra extracted from the cores in the intermediate protocluster W43-MM3. Readers can refer to Table F.13 for the line fit parameters for each core.

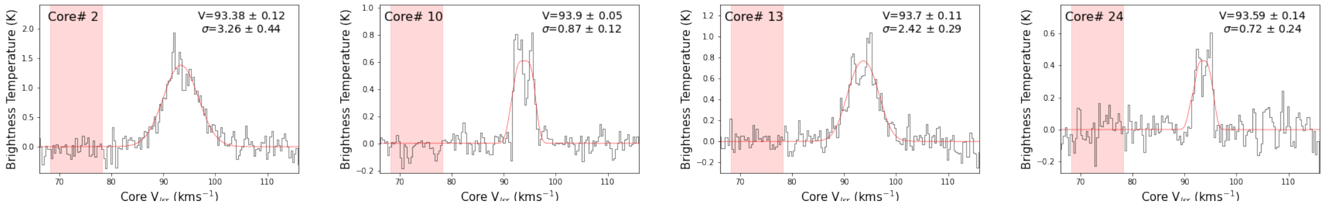

Fig. F.24. Complex-type core-averaged, background-subtracted DCN spectra extracted from the cores in the intermediate protocluster W43-MM3. Readers can refer to Table F.13 for the line fit parameters for each core.

Table F.14. DCN fits towards the core population of the intermediate protocluster W51-E.

n	Core Name	RA [ICRS]	DEC [ICRS]	F_A [″]	F_B [″]	PA [deg]	T [K]	$V_{\rm LSR}$ [km s^{-1}]	Linewidth [km s^{-1}]	Spectral Type
2	290.933185414.5095896	19:23:43.96	14:30:34.52	1.11	0.66	177	300 ± 100	63.97 ± 0.42	–	complex
4	290.932907614.5078281	19:23:43.90	14:30:28.18	0.85	0.73	6	100 ± 50	63.56 ± 0.74	–	complex
8	290.933036914.5101522	19:23:43.93	14:30:36.55	1.07	0.71	167	35 ± 10	52.79 ± 0.07	1.97 ± 0.62	single
11	290.922836614.5040393	19:23:41.48	14:30:14.54	0.79	0.68	20	25 ± 5	–	–	–
12	290.93328814.5091267	19:23:43.99	14:30:32.86	0.9	0.81	153	35 ± 10	–	–	–
13	290.932447914.5054808	19:23:43.79	14:30:19.73	0.77	0.68	27	31 ± 6	62.86 ± 0.23	–	complex
14	290.932607114.510126	19:23:43.83	14:30:36.45	0.65	0.61	174	35 ± 10	–	–	–
15	290.931505514.5099588	19:23:43.56	14:30:35.85	0.92	0.8	26	28 ± 6	–	–	–
16	290.932754414.5073581	19:23:43.86	14:30:26.49	0.91	0.48	21	35 ± 10	–	–	–
17	290.929976714.5141521	19:23:43.19	14:30:50.95	1.24	0.83	150	28 ± 6	60.95 ± 0.07	2.84 ± 1.53	single
18	290.926656814.502195	19:23:42.40	14:30:7.900	0.72	0.64	68	23 ± 5	–	–	–
19	290.932731514.5112086	19:23:43.86	14:30:40.35	0.6	0.51	11	27 ± 5	–	–	–
20	290.925572814.5112608	19:23:42.14	14:30:40.54	0.77	0.57	2	26 ± 5	–	–	–
21	290.927575714.5005965	19:23:42.62	14:30:2.150	0.64	0.57	142	23 ± 5	51.38 ± 0.05	0.7 ± 0.18	single
22	290.927781414.500986	19:23:42.67	14:30:3.550	0.8	0.69	174	24 ± 5	49.9 ± 0.11	1.49 ± 0.5	single
26	290.924399714.5149412	19:23:41.86	14:30:53.79	1.47	1.0	168	29 ± 6	60.07 ± 0.14	2.05 ± 1.02	single
28	290.931994614.5089561	19:23:43.68	14:30:32.24	0.63	0.54	65	30 ± 6	–	–	–
29	290.929639414.5149377	19:23:43.11	14:30:53.78	1.02	0.93	44	27 ± 5	61.58 ± 0.15	2.55 ± 3.69	single
30	290.926221314.5153389	19:23:42.29	14:30:55.22	0.65	0.57	70	27 ± 6	–	–	–
33	290.926670414.5017074	19:23:42.40	14:30:6.150	0.74	0.64	8	24 ± 5	–	–	–
34	290.932534914.5131101	19:23:43.81	14:30:47.20	1.08	0.94	134	25 ± 5	56.6 ± 0.07	1.12 ± 0.21	single
38	290.93495214.5078333	19:23:44.39	14:30:28.20	0.84	0.71	48	28 ± 6	–	–	–
39	290.93425614.5089017	19:23:44.22	14:30:32.05	1.02	0.89	78	28 ± 6	–	–	–

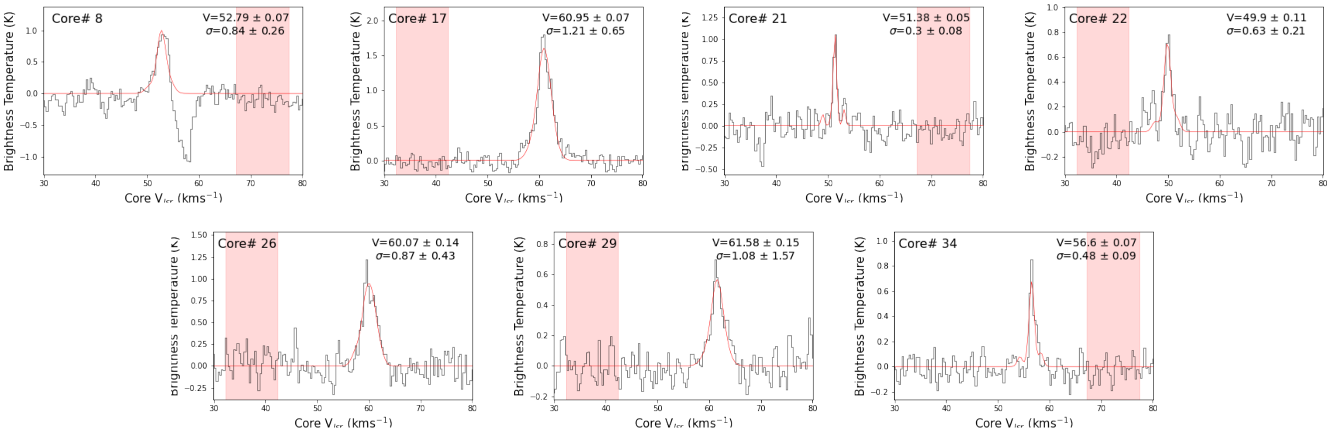

Fig. F.25. Single-type core-averaged, background-subtracted DCN spectra extracted from the cores in the intermediate protocluster W51-E. Readers can refer to Table F.14 for the line fit parameters for each core.

Table F.15. DCN fits towards the core population of the evolved protocluster W51-IRS2.

n	Core Name	RA [ICRS]	DEC [ICRS]	F_A [″]	F_B [″]	PA [deg]	T [K]	$V_{\rm LSR}$ [km s^{-1}]	Linewidth [km s^{-1}]	Spectral Type
1	290.916869914.5181896	19:23:40.05	14:31:5.480	0.72	0.66	89	300 ± 100	62.68 ± 0.19	–	complex
2	290.916470414.5181596	19:23:39.95	14:31:5.370	0.63	0.59	106	100 ± 50	60.72 ± 0.1	4.47 ± 0.95	single
4	290.910723514.5116053	19:23:38.57	14:30:41.78	0.74	0.61	150	100 ± 50	66.63 ± 0.39	–	complex
6	290.91664714.5182923	19:23:40.00	14:31:5.850	0.74	0.68	166	100 ± 50	63.28 ± 0.17	–	complex
7	290.915614814.5181323	19:23:39.75	14:31:5.280	0.67	0.58	69	100 ± 50	64.98 ± 0.11	–	complex
8	290.909155314.5185781	19:23:38.20	14:31:6.880	0.69	0.55	145	30 ± 6	61.05 ± 0.02	1.77 ± 0.12	single
9	290.910372314.5113251	19:23:38.49	14:30:40.77	0.71	0.66	84	31 ± 6	62.12 ± 0.02	1.12 ± 0.07	single
10	290.911183614.5126596	19:23:38.68	14:30:45.57	0.61	0.54	11	30 ± 6	62.31 ± 0.01	1.17 ± 0.06	single
11	290.918758714.5177443	19:23:40.50	14:31:3.880	0.82	0.67	139	37 ± 7	57.59 ± 0.02	1.59 ± 0.12	single
12	290.90857514.5182523	19:23:38.06	14:31:5.710	0.57	0.56	103	29 ± 6	59.32 ± 0.01	0.95 ± 0.04	single
13	290.905996614.5052314	19:23:37.44	14:30:18.83	0.71	0.59	11	28 ± 6	–	–	–
14	290.909192414.5092115	19:23:38.21	14:30:33.16	0.65	0.55	8	29 ± 6	62.37 ± 0.01	1.37 ± 0.04	single
15	290.910018914.510189	19:23:38.40	14:30:36.68	0.95	0.76	47	30 ± 6	63.35 ± 0.04	–	complex
16	290.908730214.5184137	19:23:38.10	14:31:6.290	0.6	0.54	109	30 ± 6	59.11 ± 0.02	0.9 ± 0.04	single
17	290.924596814.5197752	19:23:41.90	14:31:11.19	1.01	0.78	46	32 ± 7	61.37 ± 0.02	1.05 ± 0.08	single
19	290.924926214.5195877	19:23:41.98	14:31:10.52	0.56	0.49	150	33 ± 7	61.34 ± 0.03	0.75 ± 0.13	single
20	290.905668114.5182935	19:23:37.36	14:31:5.860	1.64	1.12	133	27 ± 6	60.33 ± 0.02	1.14 ± 0.09	single
22	290.925572314.5112676	19:23:42.14	14:30:40.56	0.62	0.48	7	35 ± 7	–	–	–
23	290.921855114.5211248	19:23:41.25	14:31:16.05	0.95	0.64	106	32 ± 6	63.42 ± 0.03	1.05 ± 0.1	single
24	290.911473814.5186878	19:23:38.75	14:31:7.280	0.92	0.64	38	32 ± 6	58.48 ± 0.02	1.64 ± 0.1	single
25	290.91465614.5176008	19:23:39.52	14:31:3.360	0.66	0.56	72	100 ± 50	64.65 ± 0.03	–	complex
26	290.920895914.5095599	19:23:41.02	14:30:34.42	0.63	0.56	63	31 ± 6	–	–	–
27	290.908368814.5198952	19:23:38.01	14:31:11.62	1.26	0.99	90	28 ± 6	59.96 ± 0.02	1.37 ± 0.1	single
28	290.905288814.5184717	19:23:37.27	14:31:6.500	0.94	0.82	146	27 ± 6	59.99 ± 0.09	1.14 ± 0.17	single
29	290.911773714.5112175	19:23:38.83	14:30:40.38	0.58	0.5	167	30 ± 6	65.3 ± 0.03	1.17 ± 0.12	single
31	290.912252514.5098749	19:23:38.94	14:30:35.55	0.56	0.5	174	28 ± 6	–	–	–
32	290.906946714.5064897	19:23:37.67	14:30:23.36	0.69	0.54	50	29 ± 6	63.76 ± 0.05	0.67 ± 0.16	single
33	290.923508714.5171682	19:23:41.64	14:31:1.810	0.86	0.68	170	33 ± 7	66.68 ± 0.04	1.61 ± 0.21	single
34	290.925906214.5150857	19:23:42.22	14:30:54.31	0.56	0.54	8	36 ± 7	61.08 ± 0.03	0.92 ± 0.08	single
35	290.912178514.5115741	19:23:38.92	14:30:41.67	0.59	0.51	25	29 ± 6	–	–	–
37	290.911971914.5159522	19:23:38.87	14:30:57.43	0.93	0.77	107	31 ± 6	64.96 ± 0.01	1.0 ± 0.05	single
38	290.926226214.515357	19:23:42.29	14:30:55.29	0.62	0.58	34	35 ± 7	60.66 ± 0.2	–	complex
40	290.920787414.5116943	19:23:40.99	14:30:42.10	0.66	0.62	126	31 ± 6	62.62 ± 0.03	1.04 ± 0.09	single
41	290.916181414.5181418	19:23:39.88	14:31:5.310	0.82	0.61	85	35 ± 10	61.21 ± 0.41	–	complex
42	290.918079114.5179626	19:23:40.34	14:31:4.670	0.78	0.67	104	38 ± 8	59.15 ± 0.1	1.16 ± 0.16	single
43	290.911424714.5132286	19:23:38.74	14:30:47.62	0.66	0.6	13	29 ± 6	–	–	–
44	290.923126314.5194174	19:23:41.55	14:31:9.900	0.56	0.54	148	32 ± 7	60.52 ± 0.04	0.96 ± 0.16	single
45	290.918415614.5179099	19:23:40.42	14:31:4.480	0.86	0.72	65	38 ± 8	–	–	–
46	290.907916614.5199136	19:23:37.90	14:31:11.69	1.58	1.27	117	28 ± 6	59.65 ± 0.02	1.23 ± 0.1	single
47	290.910052214.5196773	19:23:38.41	14:31:10.84	0.64	0.57	133	30 ± 6	–	–	–
48	290.913699614.517067	19:23:39.29	14:31:1.440	0.65	0.5	22	36 ± 7	64.77 ± 0.01	0.88 ± 0.05	single
49	290.911438314.5127072	19:23:38.75	14:30:45.75	0.84	0.76	102	30 ± 6	62.12 ± 0.01	1.22 ± 0.05	single
51	290.911693914.5107325	19:23:38.81	14:30:38.64	0.63	0.5	124	29 ± 6	64.92 ± 0.02	0.87 ± 0.06	single
52	290.9168114.514653	19:23:40.03	14:30:52.75	0.66	0.57	57	30 ± 6	62.72 ± 0.04	1.48 ± 0.18	single
53	290.919614614.5068189	19:23:40.71	14:30:24.55	0.55	0.5	156	31 ± 6	52.93 ± 0.07	0.62 ± 0.18	single
54	290.924726714.5084581	19:23:41.93	14:30:30.45	0.55	0.49	129	38 ± 8	–	–	–
55	290.906983914.5059755	19:23:37.68	14:30:21.51	0.62	0.57	143	29 ± 6	63.62 ± 0.06	1.06 ± 0.16	single
57	290.911114214.5111058	19:23:38.67	14:30:39.98	0.63	0.55	62	31 ± 6	–	–	–
59	290.908574314.5087426	19:23:38.06	14:30:31.47	0.65	0.63	158	29 ± 6	63.36 ± 0.02	0.88 ± 0.09	single
60	290.91181614.5117357	19:23:38.84	14:30:42.25	1.29	0.82	52	30 ± 6	65.49 ± 0.01	1.21 ± 0.04	single
61	290.911130914.519012	19:23:38.67	14:31:8.440	0.58	0.49	113	31 ± 6	–	–	–
62	290.905494814.5062954	19:23:37.32	14:30:22.66	0.62	0.51	116	27 ± 6	–	–	–
63	290.920546914.5187726	19:23:40.93	14:31:7.580	0.54	0.46	127	33 ± 7	–	–	–
64	290.905401114.5072415	19:23:37.30	14:30:26.07	0.55	0.51	1	27 ± 5	–	–	–
65	290.920362614.5140959	19:23:40.89	14:30:50.75	0.6	0.57	120	30 ± 6	–	–	–
66	290.927350314.5179344	19:23:42.56	14:31:4.560	0.86	0.69	161	31 ± 6	–	–	–
67	290.924275114.5152428	19:23:41.83	14:30:54.87	0.64	0.4	174	100 ± 50	–	–	–
68	290.914918514.5178211	19:23:39.58	14:31:4.160	0.81	0.69	47	38 ± 8	65.83 ± 0.03	–	complex
69	290.918235114.5176041	19:23:40.38	14:31:3.370	0.74	0.57	113	37 ± 8	61.65 ± 0.02	1.12 ± 0.07	single

Table F.15. continued DCN fits towards the core population of the evolved protocluster W51-IRS2.

n	Core Name	RA [ICRS]	DEC [ICRS]	F_A [$''$]	F_B [$''$]	PA [deg]	T [K]	$V_{\rm LSR}$ [km s^{-1}]	Linewidth [km s^{-1}]	Spectral Type
70	290.927487514.5198119	19:23:42.60	14:31:11.32	0.6	0.54	85	31 ± 6	–	–	–
71	290.907521914.5073516	19:23:37.81	14:30:26.47	0.59	0.57	115	28 ± 6	–	–	–
72	290.923421514.5187151	19:23:41.62	14:31:7.370	0.63	0.53	113	33 ± 7	61.58 ± 0.02	1.04 ± 0.09	single
73	290.917326114.5175912	19:23:40.16	14:31:3.330	0.63	0.47	172	37 ± 8	–	–	–
74	290.911425114.5094999	19:23:38.74	14:30:34.20	0.59	0.52	11	28 ± 6	–	–	–
75	290.917639714.5213077	19:23:40.23	14:31:16.71	0.91	0.75	173	35 ± 7	60.37 ± 0.02	1.3 ± 0.06	single
76	290.907401114.506935	19:23:37.78	14:30:24.97	0.77	0.51	37	28 ± 6	64.01 ± 0.07	1.18 ± 0.21	single
77	290.913007314.5183427	19:23:39.12	14:31:6.030	1.01	0.71	141	35 ± 7	57.54 ± 0.01	1.25 ± 0.03	single
78	290.903646914.5174172	19:23:36.88	14:31:2.700	0.63	0.5	129	27 ± 5	–	–	–
79	290.908463914.5047802	19:23:38.03	14:30:17.21	0.57	0.44	159	27 ± 6	–	–	–
80	290.906207614.50549	19:23:37.49	14:30:19.76	0.86	0.69	51	28 ± 6	64.99 ± 0.08	0.79 ± 0.24	single
81	290.908283514.5082754	19:23:37.99	14:30:29.79	1.38	0.85	54	28 ± 6	63.48 ± 0.02	1.1 ± 0.06	single
84	290.922458614.5209362	19:23:41.39	14:31:15.37	0.79	0.65	39	31 ± 6	61.03 ± 0.08	1.07 ± 0.25	single
85	290.909046214.5066179	19:23:38.17	14:30:23.82	0.77	0.57	29	27 ± 6	–	–	–
86	290.911497414.5173017	19:23:38.76	14:31:2.290	1.05	0.83	133	31 ± 6	62.72 ± 0.04	1.95 ± 0.32	single
87	290.907289414.510199	19:23:37.75	14:30:36.72	0.78	0.69	81	27 ± 5	–	–	–
88	290.904790314.5182133	19:23:37.15	14:31:5.570	0.7	0.64	3	27 ± 6	60.19 ± 0.05	1.41 ± 0.22	single
89	290.920063614.5132211	19:23:40.82	14:30:47.60	0.77	0.65	154	30 ± 6	61.49 ± 0.02	1.03 ± 0.07	single
90	290.926329814.515708	19:23:42.32	14:30:56.55	0.76	0.65	9	35 ± 7	61.34 ± 0.05	1.05 ± 0.22	single
91	290.912545314.5149959	19:23:39.01	14:30:53.99	0.69	0.59	174	30 ± 6	62.23 ± 0.01	0.7 ± 0.02	single
92	290.922819714.5254406	19:23:41.48	14:31:31.59	0.78	0.53	27	28 ± 6	–	–	–
94	290.917227714.5173194	19:23:40.13	14:31:2.350	0.57	0.5	14	37 ± 7	–	–	–
95	290.906717114.506982	19:23:37.61	14:30:25.14	0.7	0.54	171	28 ± 6	–	–	–
97	290.924309514.5175529	19:23:41.83	14:31:3.190	0.8	0.6	166	34 ± 7	62.15 ± 0.05	0.87 ± 0.17	single
99	290.920432814.5135282	19:23:40.90	14:30:48.70	0.66	0.63	65	31 ± 6	61.25 ± 0.08	1.13 ± 0.34	single
100	290.909435414.5096602	19:23:38.26	14:30:34.78	0.64	0.59	53	29 ± 6	62.85 ± 0.02	1.19 ± 0.06	single
101	290.913856914.5173454	19:23:39.33	14:31:2.440	0.66	0.65	103	37 ± 7	64.52 ± 0.01	0.91 ± 0.03	single
102	290.915392114.5217669	19:23:39.69	14:31:18.36	0.72	0.58	86	35 ± 7	61.13 ± 0.02	0.75 ± 0.07	single
104	290.909308914.5201626	19:23:38.23	14:31:12.59	0.86	0.67	4	29 ± 6	60.02 ± 0.02	1.32 ± 0.06	single
105	290.92551914.5190497	19:23:42.12	14:31:8.580	1.35	1.13	53	32 ± 7	–	–	–
106	290.925325214.5152483	19:23:42.08	14:30:54.89	0.92	0.74	69	36 ± 7	62.16 ± 0.04	0.96 ± 0.14	single
107	290.907227114.5059095	19:23:37.73	14:30:21.27	0.74	0.63	16	29 ± 6	66.19 ± 0.1	–	complex
109	290.910963614.5156795	19:23:38.63	14:30:56.45	0.98	0.68	125	30 ± 6	–	–	–
111	290.908421814.5174026	19:23:38.02	14:31:2.650	1.53	1.17	29	28 ± 6	60.33 ± 0.07	0.8 ± 0.17	single
114	290.909888814.5104222	19:23:38.37	14:30:37.52	0.76	0.68	32	30 ± 6	63.23 ± 0.06	–	complex
117	290.911454714.5109119	19:23:38.75	14:30:39.28	0.75	0.56	139	30 ± 6	64.98 ± 0.04	0.93 ± 0.16	single
119	290.909482214.5078441	19:23:38.28	14:30:28.24	1.03	0.72	37	28 ± 6	65.4 ± 0.06	1.49 ± 0.26	single
122	290.914317414.517634	19:23:39.44	14:31:3.480	1.04	0.79	121	38 ± 8	61.13 ± 0.08	–	complex

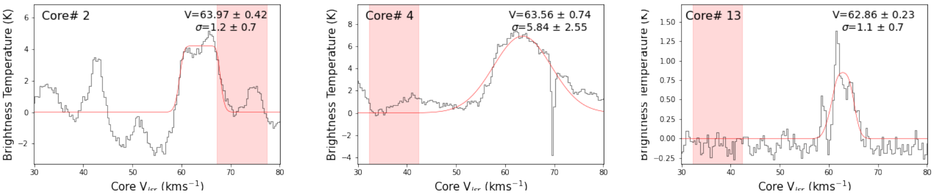

Fig. F.26. Complex-type core-averaged, background-subtracted DCN spectra extracted from the cores in the intermediate protocluster W51-E. Readers can refer to Table F.14 for the line fit parameters for each core.

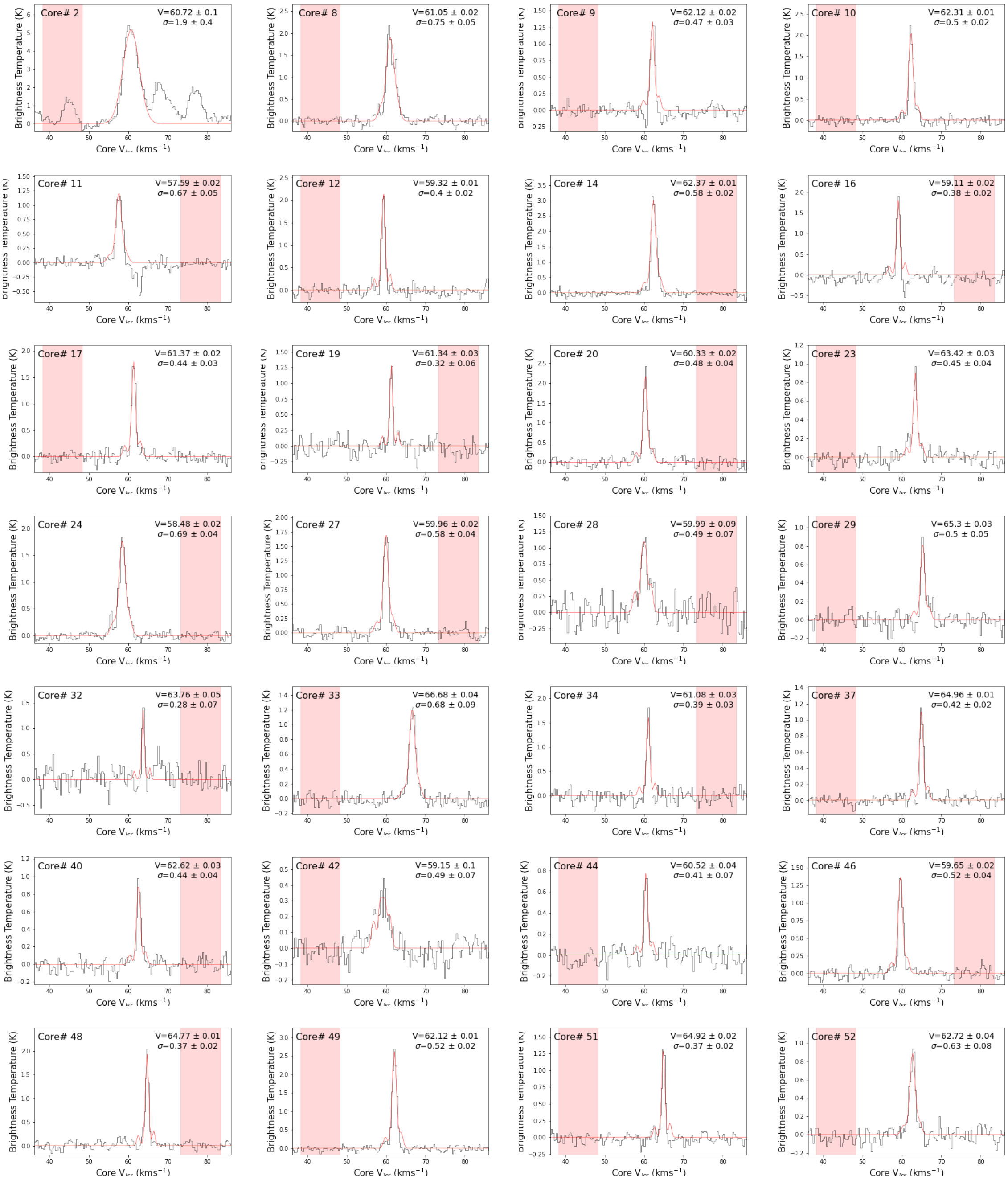

Fig. F.27. Single-type core-averaged, background-subtracted DCN spectra extracted from the cores in the evolved protocluster W51-IRS2. Readers can refer to Table F.15 for the line fit parameters for each core.

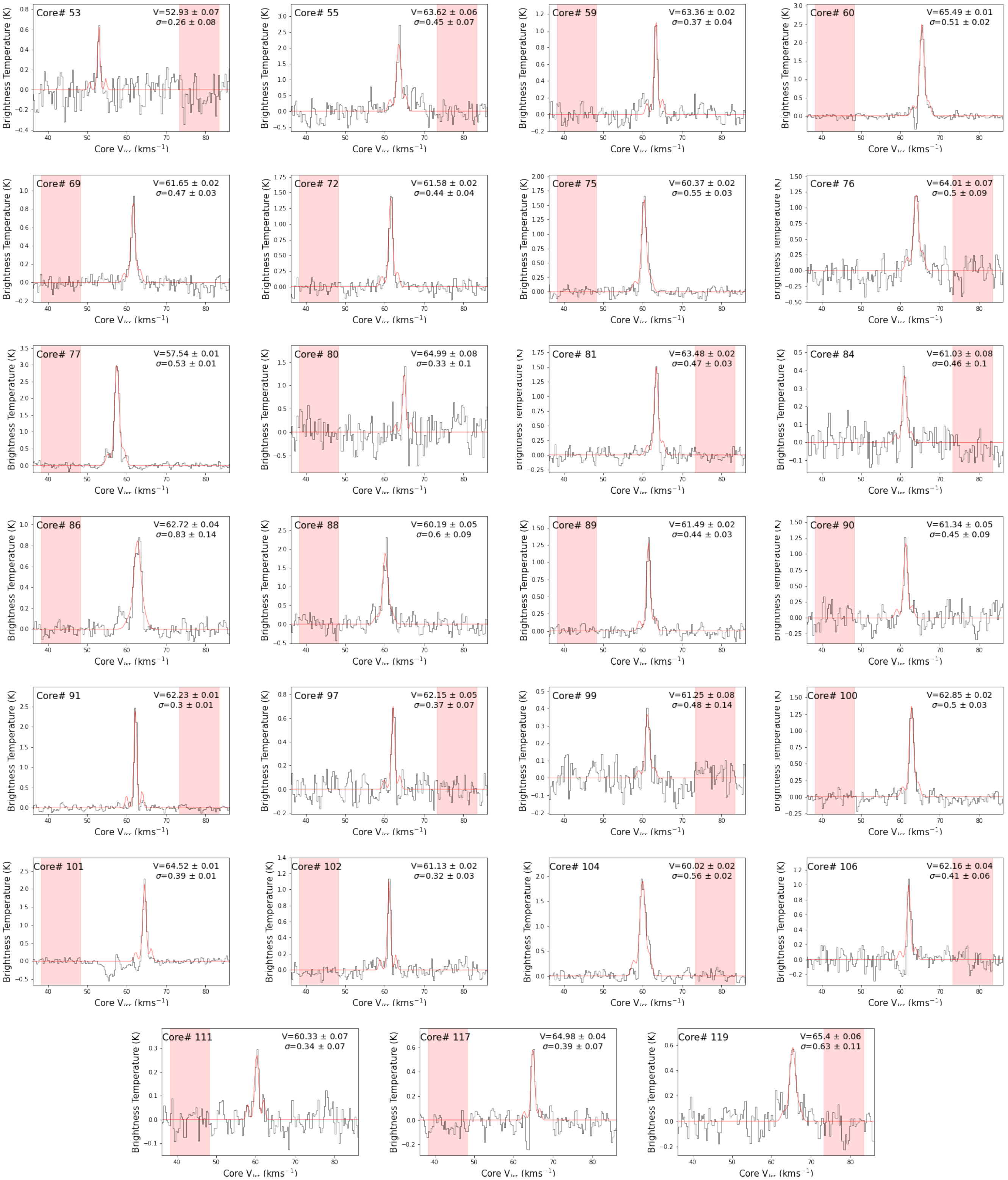

Fig. F.27. continued: Single-type core-averaged, background-subtracted DCN spectra extracted from the cores in the evolved protocluster W51-IRS2. Readers can refer to Table F.15 for the line fit parameters for each core.

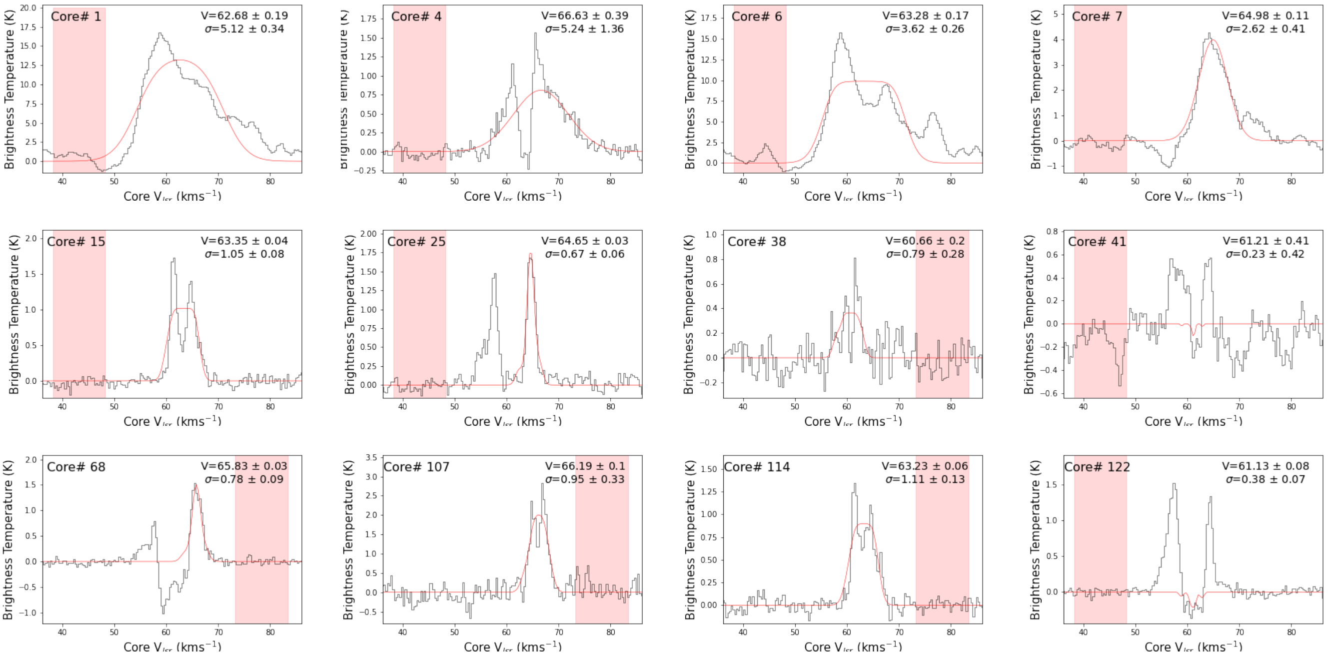

Fig. F.28. Complex-type core-averaged, background-subtracted DCN spectra extracted from the cores in the evolved protocluster W51-IRS2. Readers can refer to Table F.15 for the line fit parameters for each core.

Appendix G: DCN core kinematics

We present the core $V_{\rm LSR}$ and linewidth of the cores with DCN (3-2) detections for the remaining 13 protoclusters. G338.93 and G333.60 are presented in the main body of the text.

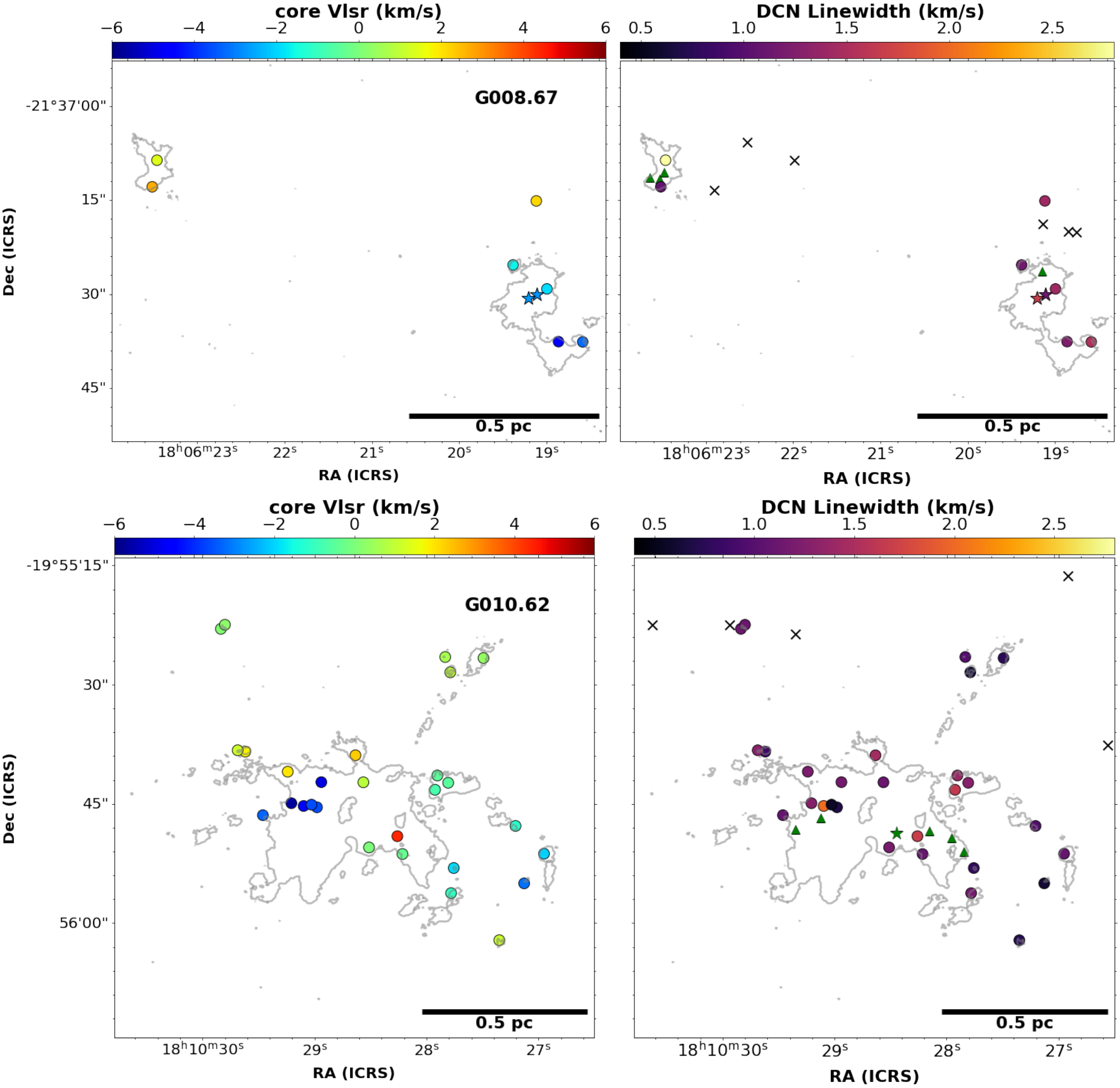

Fig. G.1. Core $V_{\rm LSR}$ (left) and DCN (3-2) linewidths (right) estimated from the DCN (3-2) fits to the continuum cores towards the intermediate, and evolved protocluster G008.67 (top) and G010.62 (bottom), respectively. The circles and stars represent the detected cores with mass estimates below and above 8 $M_\odot$, respectively, with the colour scale displaying the fitted parameters from the DCN (3-2) fits (left: core $V_{\rm LSR}$, right: linewidth). The core $V_{\rm LSR}$ is the centroid velocity of the DCN (3-2) fit minus the cloud $V_{\rm LSR}$ (taken as 37 km s^{-1}, and -2 km s^{-1} for G008.67, and G010.62, respectively). The grey contours are the 4 σ level of the DCN (3-2) moment 0 map. In the right panels, the positions of cores without a DCN (3-2) detection are marked with a black cross and black star for cores with a mass estimate below and above 8 $M_\odot$, respectively, and green triangles and stars represent cores with a complex-type DCN (3-2) spectra, with a mass estimate below and above 8 $M_\odot$, respectively.

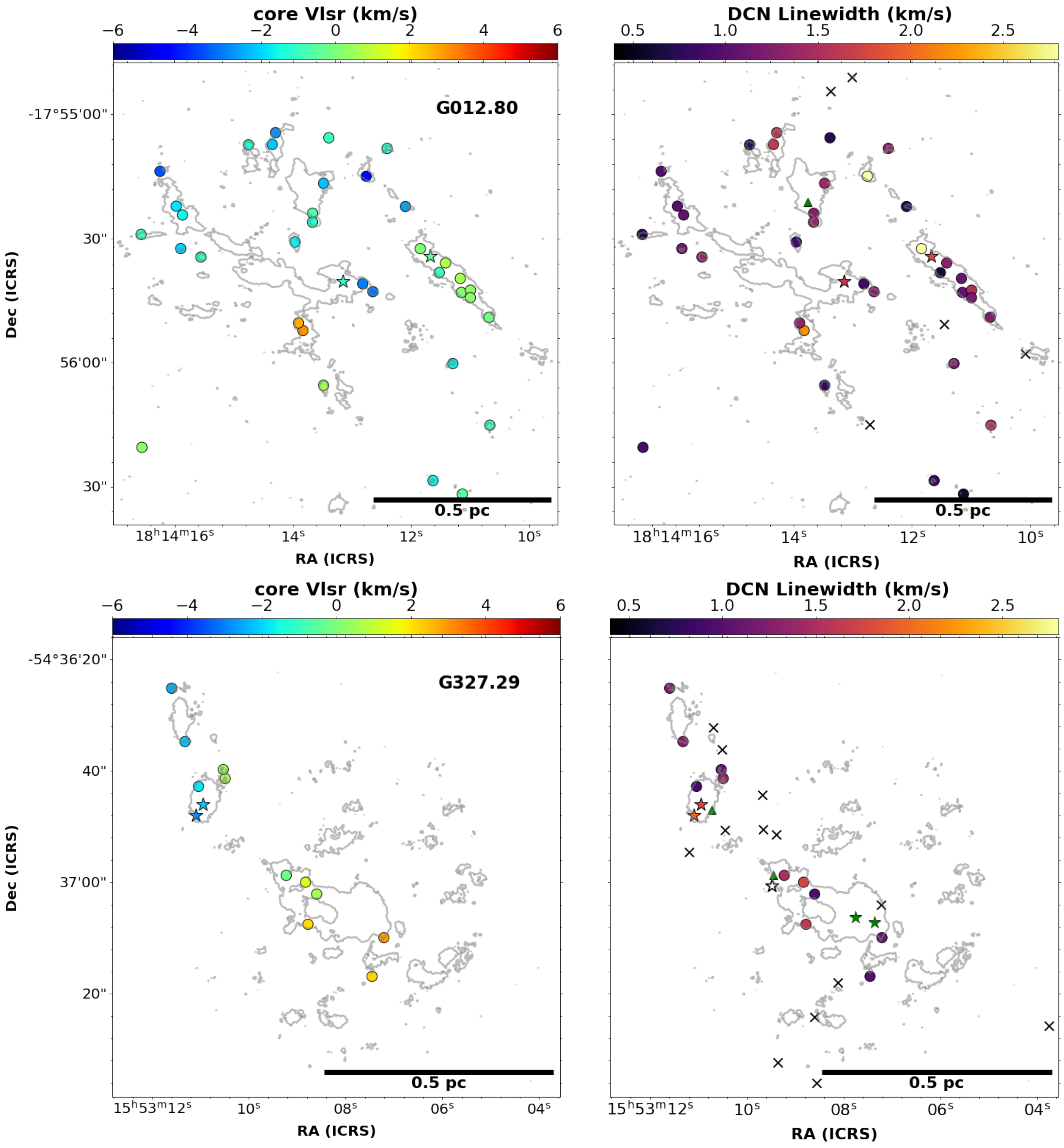

Fig. G.1. continued: Core $V_{\rm LSR}$ (left) and DCN (3-2) linewidths (right) estimated from the DCN (3-2) fits to the continuum cores towards the evolved and young protocluster G012.80 (top) and G327.29 (bottom), respectively. The core $V_{\rm LSR}$ is the centroid velocity of the DCN (3-2) fit minus the cloud $V_{\rm LSR}$ (taken as 37 km s^{-1} and -45 km s^{-1} for G012.80 and G327.29, respectively).

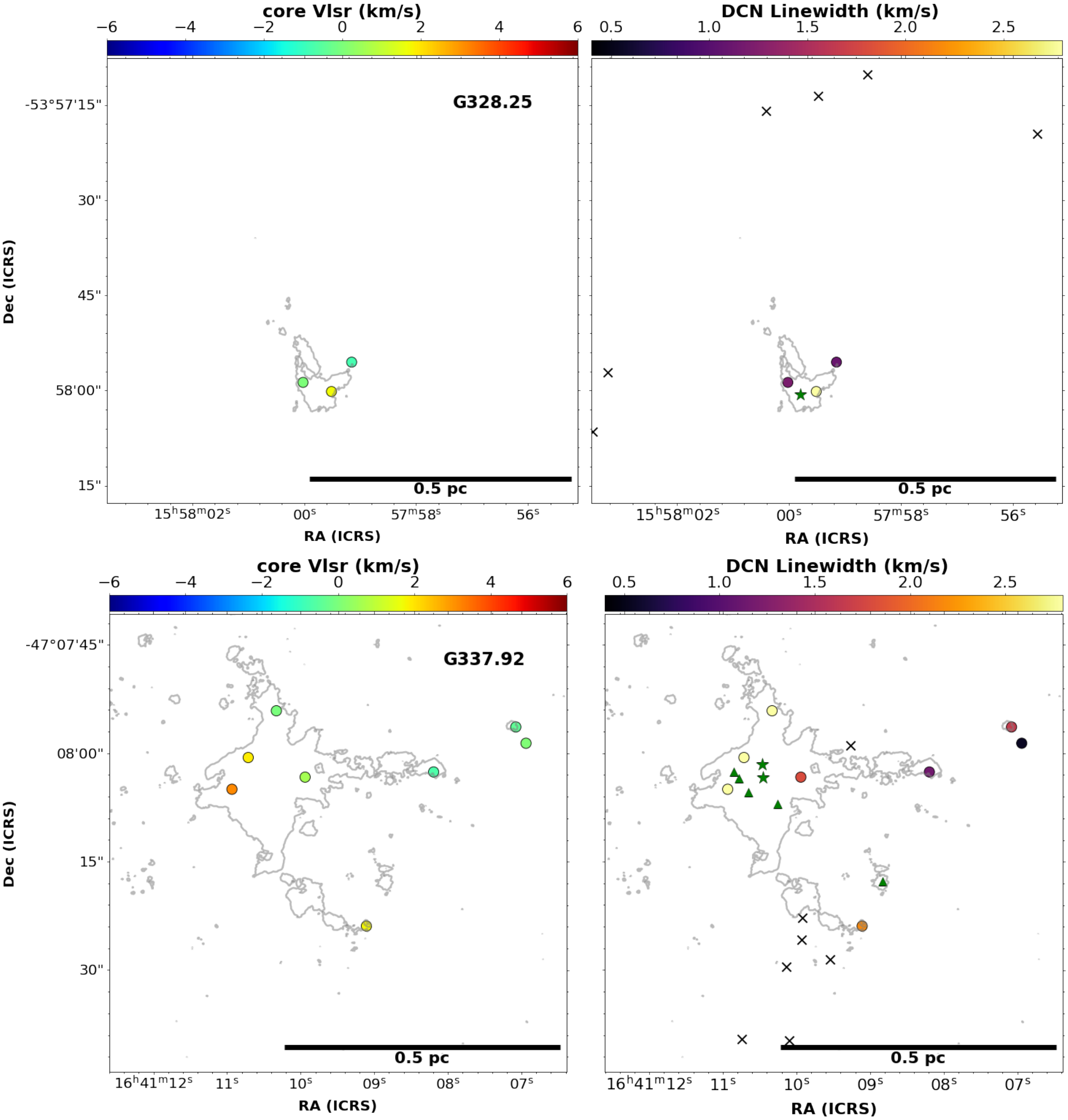

Fig. G.1. continued: Core V_{LSR} (left) and DCN (3-2) linewidths (right) estimated from the DCN (3-2) fits to the continuum cores towards the young protoclusters G328.25 (top) and G337.92 (bottom), respectively. The core V_{LSR} is the centroid velocity of the DCN (3-2) fit minus the cloud V_{LSR} (taken as -43 km s^{-1} and -40 km s^{-1} for G328.25 and G337.92, respectively).

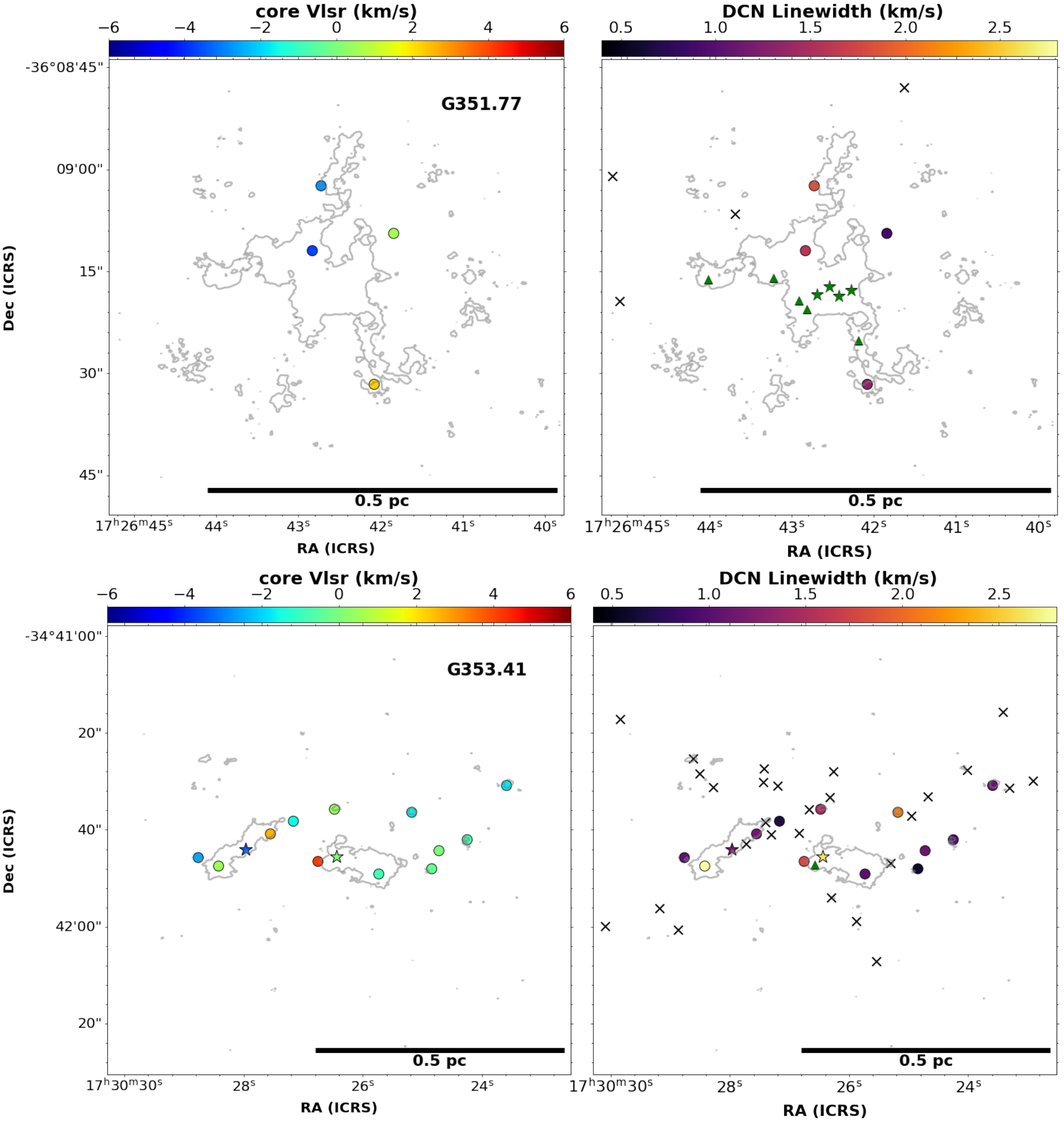

Fig. G.1. Core $V_{\rm LSR}$ (left) and DCN (3-2) linewidths (right) estimated from the DCN (3-2) fits to the continuum cores towards the intermediate protoclusters G351.77 (top) and G353.41 (bottom), respectively. The core $V_{\rm LSR}$ is the centroid velocity of the DCN (3-2) fit minus the cloud $V_{\rm LSR}$ (taken as -3 km s^{-1}, and -17 km s^{-1} for G351.77 and G353.41, respectively).

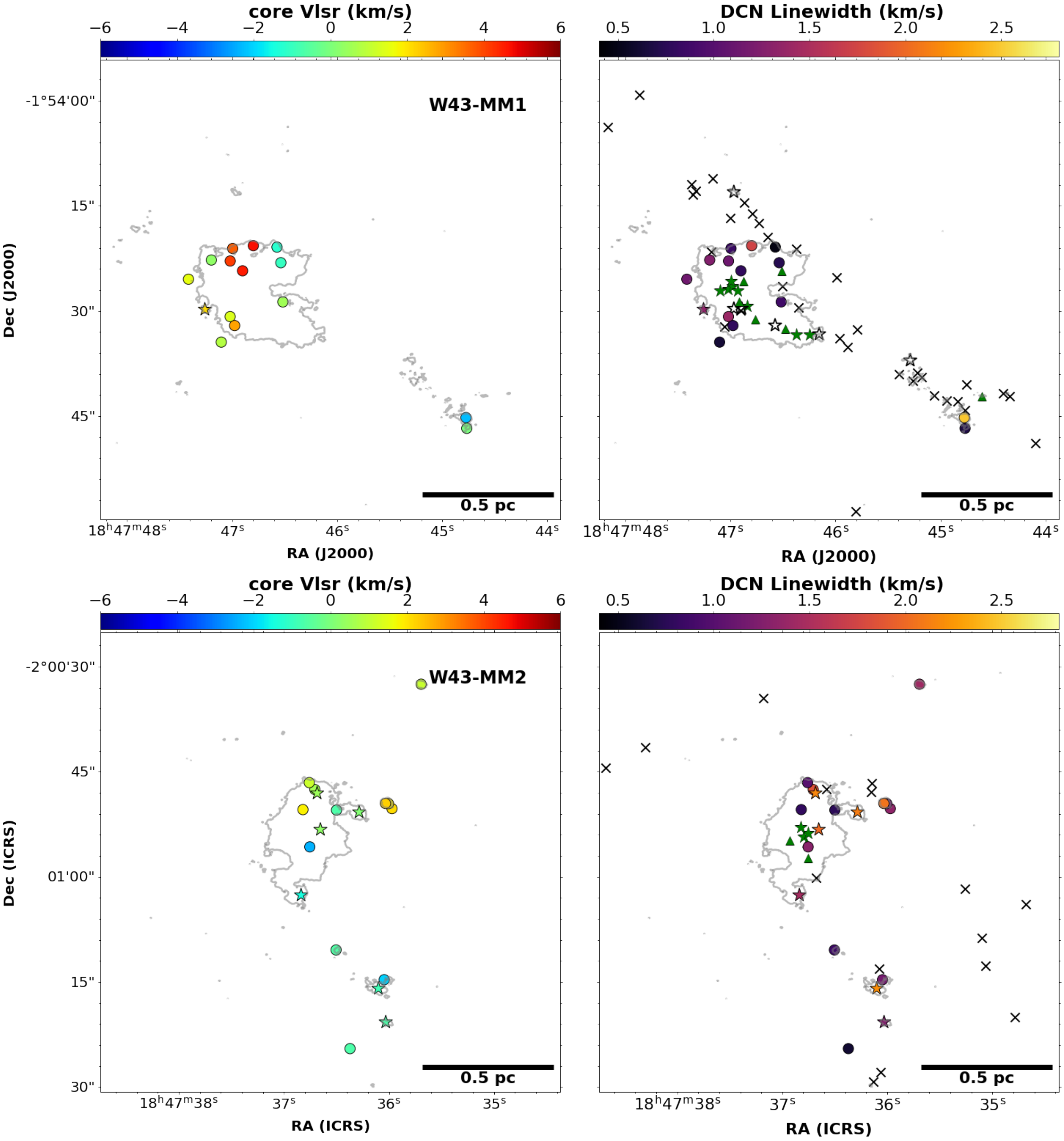

Fig. G.1. continued: Core $V_{\rm LSR}$ (left) and DCN (3-2) linewidths (right) estimated from the DCN (3-2) fits to the continuum cores towards the young protoclusters W43-MM1 (top) and W43-MM2 (bottom), respectively. The core $V_{\rm LSR}$ is the centroid velocity of the DCN (3-2) fit minus the cloud $V_{\rm LSR}$ (taken as 97 km s^{-1}, and 91 km s^{-1} for W43-MM1, and W43-MM2, respectively).

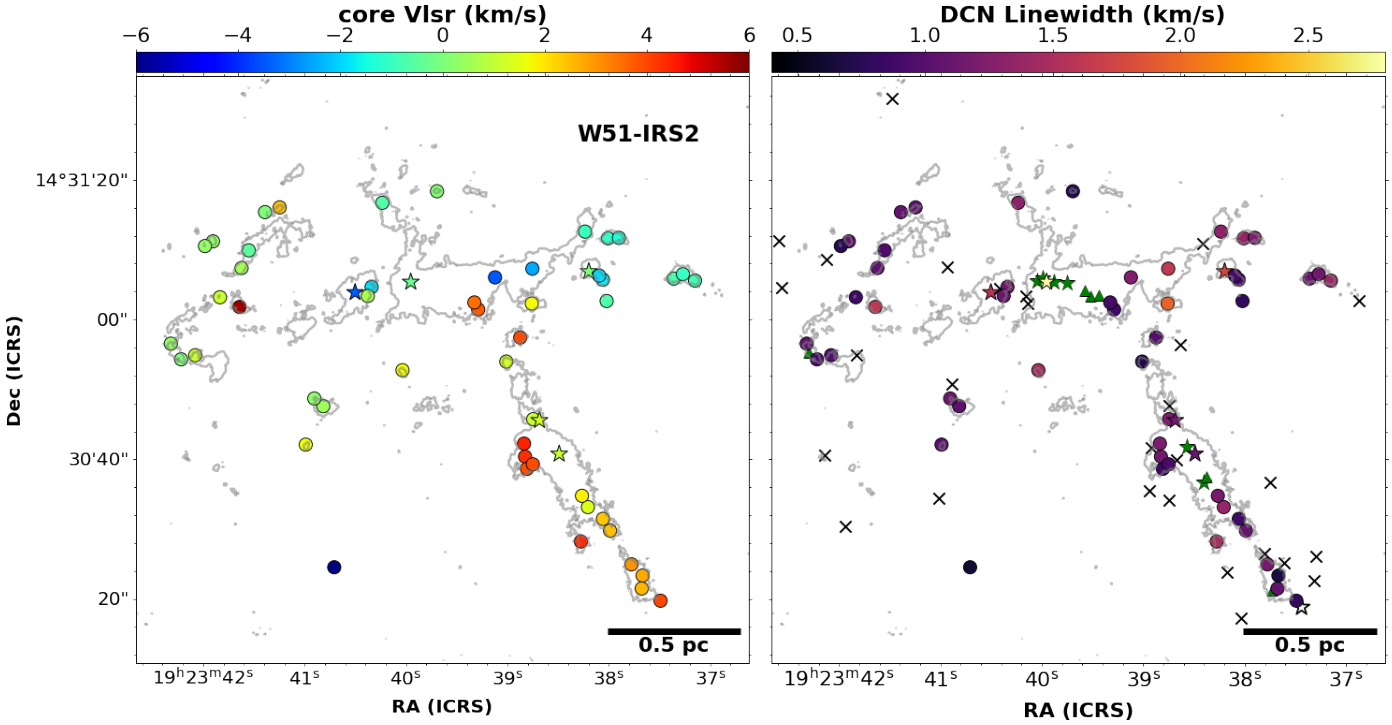

Fig. G.1. continued: Core $V_{\rm LSR}$ (left) and DCN (3-2) linewidths (right) estimated from the DCN (3-2) fits to the continuum cores towards the evolved protocluster W51-IRS2. The core $V_{\rm LSR}$ is the centroid velocity of the DCN (3-2) fit minus the cloud $V_{\rm LSR}$ (taken as 61 km s^{-1} for W51-IRS2).

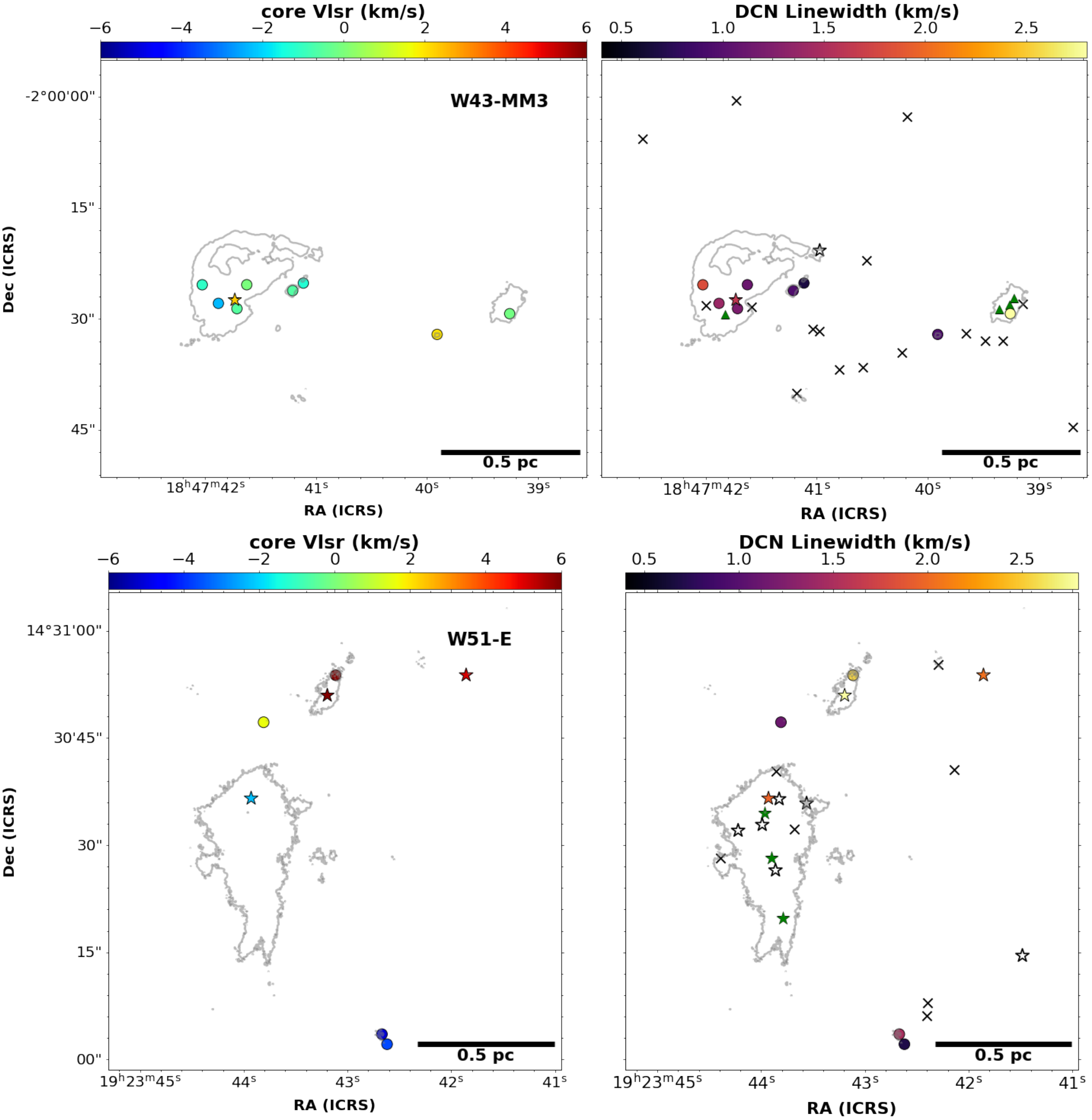

Fig. G.1. continued: Core V_{LSR} (left) and DCN (3-2) linewidths (right) estimated from the DCN (3-2) fits to the continuum cores towards the intermediate protoclusters W43-MM3 (top) and W51-E (bottom), respectively. The core V_{LSR} is the centroid velocity of the DCN (3-2) fit minus the cloud V_{LSR} (taken as 93 km s^{-1}, and 55 km s^{-1} for W43-MM3, and W51-E, respectively).